MOMENTUM TRANSPORT IN ROTATING SHEAR TURBULENCE

Dissertation

zur Erlangung des
Doktorgrades der Naturwissenschaften
(Dr. rer. nat.)

dem Fachbereich Physik
der Philipps-Universität Marburg
vorgelegt von

Hannes Jörn Brauckmann

aus Herdecke

Marburg/Lahn, 2016

Vom Fachbereich Physik der Philipps-Universität Marburg
als Dissertation angenommen am: 10.06.2016

Erstgutachter: Prof. Dr. Bruno Eckhardt, Philipps-Universität Marburg
Zweitgutachter: Prof. Dr. Jörg Schumacher, Technische Universität Ilmenau
Tag der mündlichen Prüfung: 14.06.2016
Hochschulkennziffer 1180

ABSTRACT

In turbulent shear flows, the interaction of vortices with a solid surface determines the drag exerted by the fluid. In many practical examples, wall curvature or additional body forces influence the flow and consequently change the drag. Therefore, understanding the connection between the turbulent motion and the drag force (or torque) represents an important task for fluid dynamics research. We study this connection in Taylor–Couette flow (TCF), the motion of a fluid between two independently rotating concentric cylinders, which serves as a fundamental model system to analyse the effects of wall curvature and system rotation on the turbulence and angular momentum transport resulting in the torque. Differential rotation, mean rotation and curvature of the cylinders can be varied independently by means of the shear Reynolds number Re_S, rotation number R_Ω and radius ratio η. Because of its large parameter space, TCF shows a variety of turbulent phenomena that we study in direct numerical simulations using a spectral method. Furthermore, we introduce physical models to explain the observed turbulent behaviour.

The simulations are performed in small domains, which can accommodate a single Taylor vortex pair. Periodic boundary conditions are used in the azimuthal and axial direction. We demonstrate that the small domain correctly reproduces the mean torque and velocity profile of longer or higher domains containing more vortex pairs of the same size, and only slightly influences the velocity fluctuations. Furthermore, we discuss three criteria to select an adequate spatial resolution for our simulations that results in converged torque values and velocity profiles.

For a sufficiently strong counter-rotation of the outer cylinder, the outer flow region shows turbulent bursts, i.e. it intermittently oscillates between turbulent and relatively quiescent phases. For the shear Reynolds number $Re_S = 2 \times 10^4$, we study this phenomenon in simulations of TCF for various radius ratios and determine the critical mean rotation for the onset of the bursting. We propose a theoretical model for this critical value, which is based on stability properties of the turbulent flow and also rationalises the coincidence with the torque maximum observed for $\eta \leq 0.8$. Our model suggests and the simulations show that the rotation dependence of the torque is linked to variations in the mean Taylor vortex flow, which is first enhanced for slight counter-rotation and then weakened as the bursting sets in for stronger counter-rotation. While for $\eta \lesssim 0.8$, the model conforms with the numerical results and with experiments at higher Reynolds numbers, it needs to be replaced in the limit $\eta \to 1$ where the stability properties of TCF change.

To explore this limit of vanishing curvature, we study the transition from TCF to rotating plane Couette flow (RPCF) in the limit of infinite radii.

Already for radius ratios $\eta \geq 0.9$, we find that the simulation results for TCF and RPCF collapse as a function of R_Ω, indicating a turbulent behaviour common to both systems. We observe this agreement in the torque, momentum transport by the mean flow, mean profiles and turbulent fluctuations. Moreover, for $R_\Omega > 0$, the velocity profiles of both systems are found to conform with inviscid neutral stability in the central region. Intermittent bursts, which have been observed in the outer region and have been linked to the formation of a torque maximum for counter-rotation, are shown to disappear as $\eta \to 1$. The corresponding torque maximum disappears as well. Instead, two new maxima of different origin appear for $\eta \geq 0.9$ and RPCF, a broad and a narrow one, in contrast to the results for smaller η. The broad maximum at $R_\Omega = 0.2$ is connected with a strong vortical flow and can be reproduced by streamwise-invariant simulations. The narrow maximum at $R_\Omega = 0.02$ only emerges with increasing Re_S and is accompanied by an efficient and correlated momentum transport by the mean flow.

To identify the physical mechanisms behind the two torque maxima of low-curvature TCF, we present a marginal stability model for the flow. The model assumes almost constant angular momentum in the central region and marginally stable boundary layers according to the stability condition of TCF. The model prediction reproduces the broad torque maximum, but not the narrow maximum. Furthermore, the model suggests that the narrow torque maximum results from a transition to turbulent boundary layers for small rotation numbers. An improved model implementing the boundary-layer transition reproduces the emergence of the narrow maximum. In addition, near-wall fluctuations and the torque scaling exponent in the simulations confirm the transition to turbulent boundary layers for small rotation numbers. We additionally determine the critical rotation number for this transition for the other radius ratios considered here. This reveals that the boundary-layer transition in TCF depends on the mean system rotation, differs between inner and outer cylinder and varies with the radius ratio. Finally, we discuss that our improved marginal stability model predicts the disappearance of the broad torque maximum for $Re_S \gtrsim 7 \times 10^4$ and a boundary in parameter space for the transition to turbulent boundary layers.

ZUSAMMENFASSUNG

In turbulenten Scherströmungen verursacht die Wechselwirkung von Wirbeln mit einer festen Oberfläche den Strömungswiderstand. Bei vielen Praxisbeispielen beeinflussen Wandkrümmung oder zusätzliche Volumenkräfte die Strömung und verändern somit den Widerstand. Daher besteht eine wichtige Aufgabe der Strömungsforschung darin, den Zusammenhang zwischen turbulenter Bewegung und Widerstandskraft (oder Drehmoment) zu verstehen. Wir studieren diesen Zusammenhang am Beispiel der Taylor-Couette-Strömung (TCF), der Flüssigkeitsbewegung zwischen zwei unabhängig rotierenden konzentrischen Zylindern. Sie dient als fundamentales Modellsystem, um den Einfluss von Wandkrümmung und Rotation auf die Turbulenz und den Drehimpulstransport zu untersuchen, welcher das Drehmoment verursacht. Die differentielle Rotation, mittlere Rotation und Krümmung der Zylinder können unabhängig voneinander mithilfe der Scher-Reynoldszahl Re_S, der Rotationszahl R_Ω und des Radienverhältnisses η variiert werden. Wegen der großen Zahl möglicher Parameterkombinationen zeigt die TCF eine Vielfalt von turbulenten Phänomenen, welche wir in direkten numerischen Simulationen mit einem spektralen Verfahren studieren. Zudem präsentieren wir physikalische Modelle, welche das beobachtete turbulente Verhalten erklären.

Es wurden kleine Strömungsgebiete simuliert, welche für ein einzelnes Taylor-Wirbel-Paar Platz bieten. Hierbei wurden periodische Randbedingungen in azimutaler und axialer Richtung verwendet. Wir zeigen, dass das kleine Simulationsgebiet das mittlere Drehmoment und Geschwindigkeitsprofil von Gebieten mit doppelter Länge oder dreifacher Höhe richtig wiedergibt und dass es nur geringfügig die Geschwindigkeitsfluktuationen beeinflusst. Des Weiteren diskutieren wir drei Kriterien für die Auswahl einer räumlichen Auflösung in unseren Simulationen, mit welcher konvergierte Drehmomente und Geschwindigkeitsprofile erreicht werden.

Bei ausreichend starker Gegenrotation des Außenzylinders entwickelt der äußere Strömungsbereich turbulente Bursts, d.h. er oszilliert stoßweise zwischen turbulenten und relativ ruhigen Phasen. Wir untersuchen dieses Phänomen in TCF-Simulationen für verschiedene Radienverhältnisse bei der Scher-Reynoldszahl $Re_S = 2 \times 10^4$ und bestimmen die kritische mittlere Rotation für das Einsetzen der Bursts. Wir schlagen ein theoretisches Modell für diesen kritischen Wert vor, welches auf Stabilitätseigenschaften der turbulenten Strömung beruht und auch die für $\eta \leq 0.8$ beobachtete Koinzidenz mit dem Drehmoment-Maximum erklärt. Unser Modell legt nahe und die Simulationen zeigen, dass die Rotationsabhängigkeit des Drehmoments mit der Variation der Taylor-Wirbel zusammenhängt, welche zunächst bei leichter Gegenrotation verstärkt und dann abgeschwächt werden, wenn die Bursts bei starker Gegenrotation erscheinen. Für $\eta \lesssim 0.8$ stimmt das Modell mit den Simulationsergebnissen und mit Experimenten

überein. Im Limes $\eta \to 1$ muss jedoch ein Alternativmodell gefunden werden, da sich hier die TCF-Stabilitätseigenschaften verändern.

Um diesen Grenzfall verschwindender Krümmung zu untersuchen, studieren wir den Übergang von der TCF zur rotierenden ebenen Couette-Strömung (RPCF) im Limes unendlich großer Zylinderradien. Bereits für Radienverhältnisse $\eta \geq 0.9$ fallen die Simulationsergebnisse von TCF und RPCF als Funktion von R_Ω zusammen, was auf ein gemeinsames turbulentes Verhalten der beiden Systeme hindeutet. Wir stellen diese Übereinstimmung bei dem Drehmoment, dem Impulstransport durch die mittlere Strömung, den mittleren Profilen und den turbulenten Fluktuationen fest. Für $R_\Omega > 0$ erfüllen die Geschwindigkeitsprofile beider Systeme im mittleren Bereich zudem die reibungsfreie neutrale Stabilität. Es wird gezeigt, dass die turbulenten Bursts, welche im äußeren Strömungsbereich beobachtet wurden und mit der Entstehung eines Drehmoment-Maximums bei Gegenrotation in Verbindung gebracht wurden, für $\eta \to 1$ verschwinden. Das zugehörige Drehmoment-Maximum verschwindet ebenfalls. Für $\eta \geq 0.9$ und RPCF erscheinen stattdessen zwei neue Maxima, ein breites und ein schmales, im Unterschied zu den Ergebnissen für kleinere η-Werte. Das breite Maximum bei $R_\Omega = 0.2$ ist verbunden mit einer starken Wirbelströmung und erscheint auch in Simulationen, welche in Stromrichtung invariant sind. Das schmale Maximum bei $R_\Omega = 0.02$ hingegen bildet sich erst mit steigender Scher-Reynoldszahl heraus und ist begleitet von einem effizienten und korrelierten Impulstransport durch die mittlere Strömung.

Um die physikalischen Mechanismen zu identifizieren, welche für die beiden Drehmoment-Maxima in TCF mit geringer Krümmung verantwortlich sind, präsentieren wir ein auf marginaler Stabilität basierendes Modell für die Strömung. Das Modell besteht aus den Annahmen, dass der Drehimpuls im mittleren Bereich nahezu konstant ist und dass die Grenzschichten marginal stabil gemäß der TCF-Stabilitätsbedingung sind. Es zeigt sich, dass die Modellvorhersage das breite Drehmoment-Maximum reproduziert, jedoch nicht das schmale Maximum. Zudem legt die Modellvorhersage nahe, dass das schmale Drehmoment-Maximum aus einem Übergang zu turbulenten Grenzschichten für kleine Rotationszahlen resultiert. Ein verbessertes Modell, welches den Grenzschichtübergang berücksichtigt, reproduziert das Erscheinen des schmalen Maximums. Zusätzlich bestätigen die wandnahen Fluktuationen und der Drehmoment-Skalierungsexponent in den Simulationen, dass die Grenzschichten für kleine Rotationszahlen turbulent werden. Wir bestimmen die kritische Rotationszahl für diesen Übergang auch für die anderen hier untersuchten Radienverhältnisse. Dies zeigt, dass der Grenzschichtübergang in TCF von der mittleren Systemrotation abhängt, sich zwischen dem Innen- und Außenzylinder unterscheidet und mit dem Radienverhältnis variiert. Schließlich diskutieren wir, dass unser verbessertes Modell das Verschwinden des breiten Drehmoment-Maximums für $Re_S \gtrsim 7 \times 10^4$ prognostiziert und dass es eine Grenze im Parameterraum für den Übergang zu turbulenten Grenzschichten vorhersagt.

CONTENTS

LIST OF FIGURES

LIST OF TABLES

ACRONYMS

BL	boundary layer
DNS	direct numerical simulation
PDF	probability distribution function
RMS	root-mean-square
RPCF	rotating plane Couette flow
TC	Taylor–Couette
TCF	Taylor–Couette flow

1 INTRODUCTION

1.1 MOTIVATION

Turbulence, the chaotic swirling motion of a fluid, is ubiquitous in everyday life and occurs in flows through pipes or around objects (such as aeroplanes, cars, soccer balls) or in weather phenomena. Turbulent motions often result from high shear rates, i.e. high velocity differences between neighbouring fluid layers, which cause instabilities and swirls so that the flow becomes unsteady. In addition to such shear instabilities, body forces acting on the fluid can also drive vortical motions. As a typical example, we here study rotating flows where centrifugal and Coriolis forces arise.

In the presence of a solid wall, the fluid adheres to its surface and thus adopts the velocity of the wall. As a consequence, a fluid layer with a high velocity gradient develops above the wall, commonly called boundary layer (BL). Important global properties of flows around objects, such as the drag force, are determined by the local interaction between fluid and surface within the BL. Furthermore, the drag is related to the wall-normal momentum transport caused by vortical flow structures. Therefore, it is of great interest to understand the turbulent behaviour and momentum transport in near-wall regions. Furthermore, another aim of this thesis is to analyse the influence of rotation and wall curvature on the turbulence and BL flow.

However, typical flows around objects entail several challenges, such as complicated geometries and the implementation of well-defined boundary conditions upstream and downstream, which make their study difficult. Even in the simplified case of the flow over a flat plate, the BL thickness grows downstream, and thus the flow is inhomogeneous in this direction. To avoid these difficulties, we study the turbulent behaviour, momentum transport and BL dynamics in Taylor–Couette flow, a canonic hydrodynamic system where the effects of shear, rotation and curvature can be analysed. As explained below, this system has the advantage of being closed and homogeneous in the downstream direction.

1.2 TAYLOR–COUETTE FLOW

Taylor–Couette flow (TCF), the motion of a viscous fluid between two independently rotating concentric cylinders, serves as a fundamental model system to study wall-bounded shear flows and to analyse the influence of rotation on turbulence. As illustrated in Figure 1.1, the fluid is kept in motion by rotating the inner and outer cylinder with the constant angular velocities ω_i and ω_o, respectively, which are the two main control paramet-

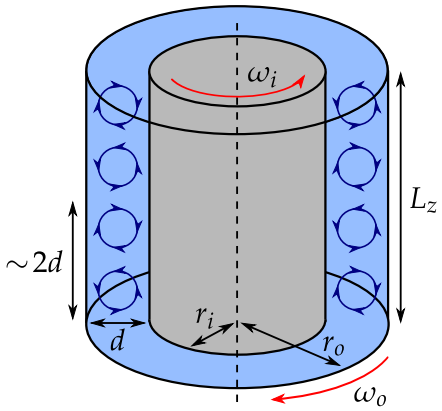

FIGURE 1.1: Sketch of the Taylor–Couette (TC) system. The flow is driven by rotating the cylinders at constant angular velocities ω_i and ω_o. The sketch also shows counter-rotating Taylor vortices that typically form in the unstable regime.

ers of the system. However, to describe the two key physical processes, it is advantageous to characterise the cylinder motion by two other parameters: The differential rotation of the cylinders results in a shear gradient driving the flow, and the average of the inner and outer cylinder rotation (denoted the mean system rotation) determines the magnitude of rotational influences on the flow. Thus, a Taylor–Couette (TC) system allows to study the effects of shear and rotation on the turbulence, since both can be adjusted individually. As a third effect, the fluid motion is influenced by the cylinder curvature that is determined by the radii r_i and r_o of the inner and outer cylinder. The corresponding geometrical parameter characterising the curvature is the radius ratio $\eta = r_i/r_o$. The influence of the curvature becomes important when the cylinder radii are comparable in size to the gap width $d = r_o - r_i$, i.e. for radius ratios η considerably below 1. Conversely, when η approaches 1, the cylinder radii become large compared to the gap width, and the geometric curvature decreases.

first experiments

In contrast to other shear flows, such as flows between plane walls or over a flat plate, TCF is periodic in the downstream direction, which avoids problems in implementing inflow and outflow conditions. With additional end plates at the top and bottom, one can build a closed hydrodynamic experiment that is relatively easy to operate and control. According to Donnelly (1991), the laminar flow between two concentric cylinders was first proposed as an experiment to quantify the viscosity of fluids by measuring the torque acting on the cylinders. Measurements in such rotating cylinder viscosimeters were first reported independently by Mallock (1888, 1896) and Couette (1890). However, they already found that the laminar flow becomes unstable at large cylinder speeds. The instability mechanism was later theoretically explained and experimentally confirmed by Taylor (1923). He found that the laminar flow becomes unstable to the formation of streamwise-invariant counter-rotating vortices, commonly called *Taylor vortices*. They introduce a natural length scale in the axial direction since one vortex pair has approximately a height of $2d$, as depicted in Figure 1.1.

routes to turbulence

After this first success, TCF has become a paradigmatic system for fluid dynamics research since many phenomena studied in this system also occur in various other flows. In particular, depending on the system rotation, TCF shows two different scenarios for the transition to turbulence. When the inner cylinder rotates only, Fenstermacher, Swinney & Gollub (1979) found that the flow undergoes only three bifurcations that introduce new modulations, before it becomes chaotic and therefore turbulent. This transition scenario was proposed by Ruelle & Takens (1971) and also occurs in Rayleigh–Bénard convection, a fluid layer heated from below (Swinney & Gollub, 1978; Eckmann, 1981). On the other hand, for counter-rotating cylinders, TCF shows a subcritical transition scenario. The turbulence suddenly occurs in form of spots and spirals that grow with increasing cylinder speeds until the entire flow is turbulent (Coles, 1965; Van Atta, 1966; Goharzadeh & Mutabazi, 2001; Prigent *et al.*, 2002, 2003; Meseguer *et al.*, 2009b). Such an intermittency, i.e. coexistence of laminar and turbulent regions, is also characteristic of the transition in plane Couette flow between moving walls (Daviaud, Hegseth & Bergé, 1992; Tillmark & Alfredsson, 1992; Bottin *et al.*, 1998; Duguet, Schlatter & Henningson, 2010) and pressure-driven channel flow (Tuckerman *et al.*, 2014). Furthermore, the turbulent patches in TCF were found to be transient, meaning that they eventually decay back to the laminar state (Borrero-Echeverry, Schatz & Tagg, 2010; Shi, Avila & Hof, 2013), similar to the transient turbulent puffs in pipe flow (Hof *et al.*, 2006). While intermittent and transient turbulence also occur in other shear flows, the TC system facilitates their experimental investigation since it is a closed system with periodic downstream direction, which enables long observation times (Avila & Hof, 2013). Furthermore, the possibility to rotate both cylinders independently enables a multitude of distinct flow states that were studied in detail (Coles, 1965; Andereck, Liu & Swinney, 1986), see also the reviews by Koschmieder (1993) and Fardin, Perge & Taberlet (2014).

turbulent regime

At high cylinder speeds, these patterns partially disappear and the bulk flow becomes turbulent. Then, instead of the distinct states, the average properties of the turbulence are relevant for flow investigations. In his pioneering work, Wendt (1933) characterised turbulent TCF by mean profiles of the azimuthal velocity and by the torque exerted on the cylinders. The former demonstrate the turbulent mixing; the latter measures the radial transport of angular momentum by the fluid motion. In the following years, many studies focussed on the bifurcations between flow states at relatively low cylinder speeds (Coles, 1965; Andereck, Liu & Swinney, 1986), and the highly turbulent regime received more attention only many years later (Lathrop, Fineberg & Swinney, 1992a,b; Lewis & Swinney, 1999; Burin, Schartman & Ji, 2010; Ravelet, Delfos & Westerweel, 2010; Paoletti & Lathrop, 2011; van Gils *et al.*, 2011; van Hout & Katz, 2011; Brauckmann & Eckhardt, 2013a; Merbold, Brauckmann & Egbers, 2013; Ostilla-Mónico *et al.*, 2014c). In this thesis, numerical simulations as well as theoretical arguments are used to study the turbulent regime of TCF in a wide para-

meter range. Such simulations provide access to the three-dimensional shape and the dynamics of turbulent flow structures, which are more difficult to obtain with experimental techniques (Tokgoz *et al.*, 2012). Based on the simulation results, the TC turbulence is studied by analysing the momentum transport and further flow characteristics that will be introduced in Section 1.3 and Section 1.4, respectively.

1.2.1 *Choice of parameters*

Traditionally, the geometry of the TC system is characterised by two dimensionless parameter, the radius ratio η and aspect ratio Γ,

$$\eta = r_i/r_o, \qquad \Gamma = L_z/d, \tag{1.1}$$

with the cylinder height L_z and gap width $d = r_o - r_i$, cf. Figure 1.1. In experiments the cylinders are confined by end plates, whereas our simulations use periodic boundary conditions in the axial direction, and hence L_z corresponds to the largest axial wavelength. The traditional dimensionless parameters describing the cylinder motion are the Reynolds numbers

traditional parameters

$$Re_i = \frac{r_i \omega_i d}{\nu}, \qquad Re_o = \frac{r_o \omega_o d}{\nu}, \tag{1.2}$$

that measure the velocities of inner and outer cylinder in viscous units, cf. Andereck, Liu & Swinney (1986). Furthermore, the ratio of angular velocities $\mu = \omega_o/\omega_i$ (also denoted *rotation ratio*) is commonly used to characterise the rotation state of the outer cylinder relative to the inner one (Taylor, 1923). However, these parameters do not describe the key dynamical processes of shear and system rotation independently, and they are not suited to study the limit $\eta \to 1$, as will be discussed in Section 4.1.1.

Instead, we therefore use parameters that describe the dynamics since they arise from the equations of motion (Dubrulle *et al.*, 2005). In this context, formulating the equations in a reference frame rotating with a typical angular velocity Ω_{rf} around the cylinder axis is the key to find a reasonable parameter for the system rotation. In this thesis, we study the motion of an incompressible fluid that is characterised by the constant mass density ρ_f and kinematic viscosity ν, as well as the velocity and pressure fields $\boldsymbol{u}(\boldsymbol{x}, t)$ and $p(\boldsymbol{x}, t)$ in the rotating frame. The equations of motion are given by the Navier–Stokes and continuity equations (Landau & Lifshitz, 1987)

equations of motion

$$\partial_t \boldsymbol{u} + (\boldsymbol{u} \cdot \boldsymbol{\nabla})\boldsymbol{u} = -\boldsymbol{\nabla} p - R_\Omega \, \boldsymbol{e}_z \times \boldsymbol{u} + \frac{1}{Re_S} \Delta \boldsymbol{u}, \qquad \boldsymbol{\nabla} \cdot \boldsymbol{u} = 0, \tag{1.3}$$

here formulated in the rotating reference frame by applying the transformation described in Section 2.1. Furthermore, (1.3) has already been rendered dimensionless using the velocity difference between the cylinders U_0 and the gap width d as characteristic scales for all velocities and lengths. Consequently, all times and pressures are measured in units

of d/U_0 and $\rho_f U_0^2$, respectively. In this form, the equations of motion (1.3) have only two dimensionless dynamical parameters,

$$Re_S = \frac{U_0\, d}{\nu}, \qquad R_\Omega = \frac{2\Omega_{\mathrm{rf}}\, d}{U_0}, \tag{1.4}$$

dynamical parameters

the shear Reynolds number Re_S measuring the shear gradient between the cylinders and the rotation number R_Ω that estimates the ratio between system rotation and shear. While the combination of scales in (1.4) clearly follows from the equations of motion, the choice of the velocity scale U_0 and of the reference frame rotation Ω_{rf} is ambiguous. For example, the parameters used by Nagata (1986) correspond to $U_0^N = (r_i + r_o)(\omega_i - \omega_o)/2$ and $\Omega_{\mathrm{rf}}^N = (\omega_i + \omega_o)/2$, whereas Ostilla *et al.* (2013) used other scales $U_0^O = r_i(\omega_i - \omega_o)$ and $\Omega_{\mathrm{rf}}^O = \omega_o$. (Without loss of generality, we here assume that $\omega_i > \omega_o$.) However, we follow the analysis by Dubrulle *et al.* (2005) and choose Ω_{rf} such that, in the rotating reference frame, the cylinders are exactly counter-rotating with equal but opposite velocities. In the rotating frame, the velocity difference between the cylinders then serves as the velocity scale U_0. As will be shown in Section 4.1, these choices for Ω_{rf} and U_0 result in the parameters

$$Re_S = \frac{2}{1+\eta}(Re_i - \eta Re_o), \qquad R_\Omega = (1-\eta)\frac{Re_i + Re_o}{Re_i - \eta Re_o}, \tag{1.5}$$

introduced by Dubrulle *et al.* (2005) and used here. In addition, they specified the geometric mean radius $\widetilde{r} = \sqrt{r_i r_o}/d$ as a second length scale and define the curvature number $R_C = 1/\widetilde{r} = (1-\eta)/\sqrt{\eta}$ to characterise the curvature of the TC system. Altogether, R_C, Re_S and R_Ω are the three main parameters (Dubrulle *et al.*, 2005). However, we will still identify the different TC geometries by the more commonly used radius ratio η (instead of R_C). Furthermore, one exception to this parameter choice occurs in Chapter 3 and Section 4.2, where the effects of counter-rotation can be more adequately characterised by the rotation ratio μ (instead of R_Ω).

The quality of these parameters can be assessed by testing how consistently they describe the TCF results. Coles (1967) already noted that '*the effect of geometry can be suppressed by a proper choice of variables.*' Our results will show that the parameters Re_S and R_Ω fulfil this requirement in a wide range.

1.2.2 *Relation to rotating plane Couette flow*

cylinder curvature

The influence of the curvature of the cylinder walls can be captured by the radius ratio $\eta = r_i/r_o$ or the curvature number R_C. If the radius ratio falls considerably below 1 (i.e. $R_C > 0$), the influence of curvature on the fluid motion becomes important, see for example $\eta = 0.71$ in Figure 1.2(a). Conversely, the system curvature becomes small when η approaches 1 while keeping the gap width d constant (as illustrated in Figure 1.2(a)), since the cylinder radii diverge in this limit as indicated by $R_C \to 0$. Then,

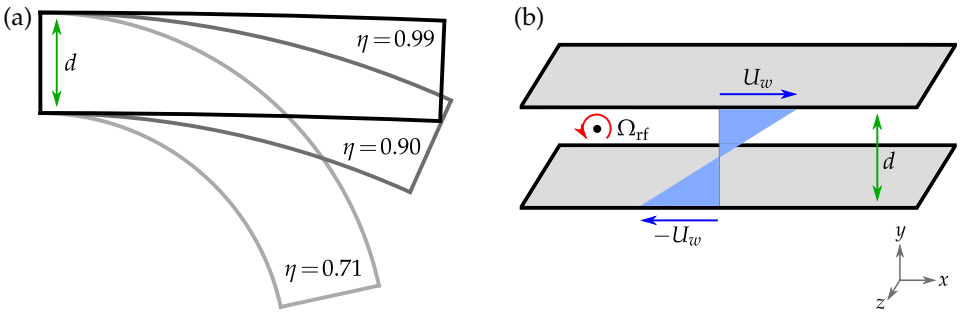

FIGURE 1.2: The cylinder curvature in TCF disappears for $\eta \to 1$, and the system approximates rotating plane Couette flow (RPCF). (a) Shown is a domain of length $L_\varphi = 4d$ for three typical values of the radius ratio η investigated here (representation adopted from Faisst & Eckhardt (2000)). (b) Sketch of plane Couette flow with wall velocity U_w rotating with the angular velocity Ω_{rf} around the spanwise axis.

the TC system approximates plane Couette flow subject to spanwise system rotation, cf. Figure 1.2(b), commonly called rotating plane Couette flow (RPCF). This RPCF-limit of TCF is relevant for rotating astrophysical and geophysical flows, as the radii in these systems are often much larger than the flow structures so that the curvature becomes small (Hersant, Dubrulle & Huré, 2005; Dubrulle *et al.*, 2005; Rincon, Ogilvie & Cossu, 2007).

RPCF-limit of TCF

In the context of the transition to turbulence, the RPCF-limit of the TC system has already been studied in an approximation where certain curvature terms in the equations of motion have been neglected (Nagata, 1986, 1990; Demay, Iooss & Laure, 1992). Nagata found that wavy vortices, which develop as an instability of streamwise-invariant Taylor vortices, can be continued to non-rotating plane Couette flow where they form finite-amplitude solutions. Such wavy roll cells were also observed experimentally in RPCF at low shear rates (Hiwatashi *et al.*, 2007). Moreover, by considering the full equations of motion, Faisst & Eckhardt (2000) were able to continuously study the transition from TC to plane Couette flow and found that, already for radius ratios η below 1, some characteristics of plane Couette flow can be observed. Furthermore, Dubrulle *et al.* (2005) noted that the linear stability criterion for the laminar state in RPCF (Lezius & Johnston, 1976) is approximated by the stability boundary of TCF (Esser & Grossmann, 1996) when the radius ratio η tends to 1. Beyond the first bifurcation towards turbulence, further transitions create a rich set of flow states also in RPCF (Tsukahara, Tillmark & Alfredsson, 2010; Daly *et al.*, 2014), reminiscent of the states described by Andereck, Liu & Swinney (1986) in TCF.

In an extension of these bifurcation studies at low Reynolds numbers that revealed several similarities between the two systems, in Chapter 4 we will investigate the continuous transition of TCF to RPCF in the turbulent regime. For this purpose, we performed numerical simulations of TCF for seven values of η ranging between 0.5 and 0.99. For each radius ratio, three turbulent shear rates and various mean rotation states were realised.

Thus, we can study the influence of system rotation in the limit of vanishing curvature. These TC simulations were complemented by analogous simulations of RPCF to compare directly to the curvature-free limit.

1.3 ANGULAR MOMENTUM TRANSPORT AND TORQUE

momentum transport

As fluid parcels move in the flow, they carry momentum to another place. In addition, the friction between neighbouring fluid layers results in a diffusion (i.e. molecular transport) of momentum. We study this momentum transport which is governed by the Navier–Stokes equations (1.3) describing the local momentum balance. For TCF, we introduce cylindrical coordinates (r, φ, z) with velocities $\boldsymbol{u} = (u_r, u_\varphi, u_z)$ to account for the annular geometry.

While the equations of motion (1.3) describe the conservation of linear momentum (Landau & Lifshitz, 1987), in cylindrical coordinates, an analogous continuity equation for the specific angular momentum $\mathcal{L} = ru_\varphi$ can be obtained from the φ-component of (1.3) multiplied by the radius r. Averaging the equation over a concentric cylindrical surface (using the area average $\langle\cdots\rangle_A = \langle\cdots\rangle_{\varphi z}$) results in the continuity equation for $\mathcal{L}$

angular momentum transport

$$\partial_t \langle \mathcal{L} \rangle_A + r^{-1} \partial_r (r J^{\mathcal{L}}) = 0 \tag{1.6}$$

with the angular-momentum flux

$$J^{\mathcal{L}} = \langle u_r \mathcal{L} \rangle_A - Re_S^{-1} r^2 \partial_r \langle \omega \rangle_A, \tag{1.7}$$

that measures the radial transport of angular momentum, see also Marcus (1984a). Here, $\langle u_r \mathcal{L} \rangle_A$ denotes the convective transport due to radial flows, and the radial gradient of the angular velocity $\omega = u_\varphi / r$ gives rise to a diffusive transport mediated by viscosity. Since we only study statistically stationary cases, we additionally average (1.6) in time giving radial profiles $\langle\cdots\rangle(r) = \langle\cdots\rangle_{\varphi z t}$. Hence, the time dependence drops out, i.e. $\partial_t \langle \mathcal{L} \rangle = 0$, and (1.6) reveals that the transverse current

$$J^\omega = r \left\langle J^{\mathcal{L}} \right\rangle_t = r^3 \left(\langle u_r \omega \rangle - Re_S^{-1} \, \partial_r \langle \omega \rangle \right) \tag{1.8}$$

is a constant, i.e. independent of the radius for all $r \in [r_i, r_o]$ and averaged over φ, z and t (Eckhardt, Grossmann & Lohse, 2007b). The radial flux $J^{\mathcal{L}}$ results in a loss of angular momentum at the inner cylinder that is compensated by a torque T exerted on the cylinder to keep it at a constant speed (Marcus, 1984a). This balance gives a relation between the dimensionless torque

dimensionless torque

$$G = \frac{T}{2\pi L_z \rho_f \nu^2 d} = Re_S^2 \, r J^{\mathcal{L}} = Re_S^2 \, J^\omega \tag{1.9}$$

and the transverse current J^ω, where L_z is the cylinder height (Eckhardt, Grossmann & Lohse, 2007b). For the laminar flow, the first term in (1.8)

vanishes, and only the radial derivative of the laminar angular velocity profile $\omega_{\mathrm{lam}}(r)$ contributes to the current. In the inertial reference frame, it is given by the circular Couette flow

$$\hat{\omega}_{\mathrm{lam}}(r) = \frac{1}{2}\left(R_\Omega - 1 + \frac{\tilde{r}^2}{r^2}\right), \tag{1.10}$$

and in the rotating reference frame by $\omega_{\mathrm{lam}}(r) = (\tilde{r}^2/r^2 - 1)/2$, with r ranging between r_i/d and r_o/d. We use the corresponding laminar torque value $G_{\mathrm{lam}} = \eta(1-\eta)^{-2}Re_S$ as the unit to measure all torques and introduce the Nusselt number

Nusselt number

$$Nu_\omega = G/G_{\mathrm{lam}} = J^\omega/J^\omega_{\mathrm{lam}}, \tag{1.11}$$

in analogy to the Nusselt number measuring the heat flux in thermal convection (Dubrulle & Hersant, 2002; Eckhardt, Grossmann & Lohse, 2007a).

In addition to the flux of angular momentum, the turbulence also generates a flux of energy. By exerting a torque on the cylinders, energy is injected into the flow, which is eventually dissipated by viscous friction. In the statistically stationary state and averaged over long times, the energy input must equal the volume energy dissipation rate $\widetilde{\varepsilon}$. This balance is expressed by the relation

energy balance

$$\widetilde{\varepsilon} = Nu_\omega/Re_S \qquad \text{with} \qquad \widetilde{\varepsilon} = \frac{1}{2Re_S}\left\langle \left(\partial_i u_j + \partial_j u_i\right)^2 \right\rangle_{V,t} \tag{1.12}$$

between dissipation rate and Nusselt number, which can be derived directly from the Navier–Stokes equations (1.3), see Eckhardt, Grossmann & Lohse (2007b). Note that for consistency the dissipation rate is here measured in advective units U_0^3/d instead of the frequently used viscous units ν^3/d^4. In the latter units, the dissipation rate reads $\varepsilon_\nu = Re_S^3\,\widetilde{\varepsilon}$.

The angular-momentum flux $J^{\mathcal{L}}$ and Nusselt number Nu_ω are the key physical quantities for our study of angular momentum transport and torque in TCF. Furthermore, the balance (1.12) allows to apply theoretical estimates for the energy dissipation to the torque. Analogous relations between a transverse flux, a Nusselt number and the energy dissipation also exist for the heat transport in thermal convection and the momentum transport in pipe flow (Eckhardt, Grossmann & Lohse, 2007a) as well as in plane Couette flow (Salewski & Eckhardt, 2015). In the study of these flows, one of the key challenges is to understand and predict the variation of the Nusselt number with external parameters.

torque scaling estimates

Over the years, various theoretical approaches have been proposed to predict the torque at given cylinder speeds. Using Kolmogorov-type arguments and dimensional analysis, Lathrop, Fineberg & Swinney (1992a) estimated the global energy dissipation rate in physical units as $\varepsilon = U_0^3/d$, where U_0 and d are the external velocity and length scales. Since it corresponds to $\widetilde{\varepsilon} = 1$ in (1.12), this estimate predicts the torque scaling $G \sim Re_S^\alpha$ with $\alpha = 2$. More rigorous estimates, which are derived from the Navier–Stokes equations, provide only an upper bound on the momentum transport (Busse, 1970) or on the energy dissipation (Doering & Constantin,

1992, 1994). Both bounds also predict the torque scaling exponent $\alpha = 2$. However, even further improved upper bounds overestimate the experimental torques by one order of magnitude (Nicodemus, Grossmann & Holthaus, 1997b,a). Another theoretical approach uses the marginal stability assumption that the turbulence realises a velocity profile which just does not provoke further flow instabilities. For large Reynolds numbers and stationary outer cylinder, the marginal stability theory results in the torque scaling $G \sim Re_i^{5/3}$ (King *et al.*, 1984; Marcus, 1984b; Barcilon & Brindley, 1984).

no pure power-law torque scaling

In contrast to these theoretical predictions, torque measurements revealed that the scaling exponent α varies with the Reynolds numbers. First, Wendt (1933) found two regimes with torque scaling exponents $\alpha = 1.5$ for $4 \times 10^2 < Re_i < 10^4$ and $\alpha = 1.7$ for $Re_i > 10^4$. Later, detailed torque measurements revealed that the exponent is not constant over any Reynolds-number range. Instead, the locally calculated $\alpha(Re_i)$ increases monotonically with Re_i from $\alpha = 1.23$ to 1.87 in the range $8 \times 10^2 < Re_i < 1.2 \times 10^6$ (Lathrop, Fineberg & Swinney, 1992a,b; Lewis & Swinney, 1999). Furthermore, these authors showed that the torque variation expressed by the friction factor $c_f = G/Re_i^2$ is in agreement with a Prandtl–von Kármán skin friction law and qualitatively conforms with the friction-factor variation of turbulent flows in a pipe and over a flat plate. In addition, the friction factor of channel flow also follows a skin friction law (Schultz & Flack, 2013), suggesting that this is a general behaviour for highly turbulent shear flows. In TCF, the experimental torque variation is also in line with theories that decompose the energy dissipation and angular-momentum flux into a BL and bulk contribution with different scalings (Eckhardt, Grossmann & Lohse, 2000, 2007b), or that introduce logarithmic corrections to the upper-bound scaling $G \sim Re_i^2$ (Dubrulle & Hersant, 2002). The latter two theories also include a dependence of the torque on the radius ratio η.

rotation dependence of torque

Remarkably, all aforementioned theoretical predictions only concern the torque scaling with Re_S or with Re_i for a stationary outer cylinder. However, already torque measurements by Wendt (1933) showed that the system rotation also influences the angular momentum transport. Dubrulle *et al.* (2005) found that the torque variation can be represented by a scaling with Re_S multiplied by a function that depends on the system rotation and shows a maximum. Furthermore, recent TC experiments with $\eta \approx 0.7$ revealed that the torque as a function of system rotation is maximised for counter-rotating cylinders (Paoletti & Lathrop, 2011; van Gils *et al.*, 2011), as also confirmed in numerical simulations (Brauckmann & Eckhardt, 2013a; Ostilla *et al.*, 2013). However, this torque variation with R_Ω has received much less attention than the scaling with Re_S. Therefore, we here study the rotation dependence of the torque in numerical simulations and introduce theoretical models to explain the variation with R_Ω, as well as its dependence on the radius ratio η.

1.4 CHARACTERISTICS OF TURBULENT SHEAR FLOWS

velocity profiles

The previous section introduced the torque G and flux $J^{\mathcal{L}}$ to characterise the angular momentum transport in TCF. Another characteristic of turbulent flows is given by the mean distribution of the streamwise velocity, which in case of TCF is the component u_φ averaged over concentric cylinders and over time, resulting in the radial profile $\langle u_\varphi \rangle(r)$. While the laminar profile shows a uniform decline from the faster inner cylinder to the outer cylinder, the turbulent profile is flattened in the middle region causing high velocity gradients in thin layers close to the walls, see e.g. Wendt (1933). The latter regions of high shear are the boundary layers (BLs) that dominate the interaction between flow and solid wall. The profile flattening results from the turbulent mixing of momentum. However, even in the highly turbulent regime, the profiles often show a residual gradient in the middle, as for instance found in plane Couette flow (Avsarkisov *et al.*, 2014). Since the profile gradients in the central region characterise the strength of turbulent mixing, they will be studied here as well.

profile models

Many theoretical studies predict the functional shape of velocity profiles using simplified model equations. As a historically important example, the Prandtl–Blasius theory predicts the profile shape of a laminar BL (Prandtl, 1905; Blasius, 1908). However, in wall-bounded shear flows the profile consists of a bulk (i.e. central) region surrounded by two BLs. To model the entire profile, marginal stability arguments have been employed in Rayleigh–Bénard convection (Malkus, 1954; Howard, 1966), channel flow (Malkus, 1956) and in TCF with stationary outer cylinder (King *et al.*, 1984; Marcus, 1984b; Barcilon & Brindley, 1984). These theories assume that the turbulence realises a mean profile that is neutrally stable to vortical perturbations. In order to study the effect of system rotation in TCF, we here generalise and extend previous marginal stability models to the case of independently rotating cylinders. On the other hand, at sufficiently large shear rates, BLs become unstable to the formation of vortices and transition to turbulence (Schlichting & Gersten, 2006). Then, the BL is interspersed with vortices of various sizes that increase the momentum transport and mixing in vicinity of the wall. In this case, the theory by von Kármán predicts that a logarithmic profile region develops in the BL (Pope, 2000). Indeed, experiments and simulations show that logarithmic BLs are a general feature of highly turbulent wall-bounded flows since they occur in TCF (Smith & Townsend, 1982; Huisman *et al.*, 2013; Grossmann, Lohse & Sun, 2014), plane Couette flow (Avsarkisov *et al.*, 2014), channel flow (Schultz & Flack, 2013) and pipe flow (Hultmark *et al.*, 2012).

turbulent intermittency

Averaged quantities, such as torque and mean profiles, only describe the flow well when the turbulence is space-filling and fluctuates around a single state. However, this is not always the case as the flow can be composed of laminar and turbulent regions at the onset of turbulence (Coles, 1965; Van Atta, 1966). Furthermore, Brethouwer, Duguet & Schlatter (2012) showed that such turbulent–laminar patterns persist up to large Reynolds

numbers of several 10^4, when a shear flow is stabilised by a damping body force. In TCF, the outer region can be stabilised by rotating the cylinders in opposite directions (Chandrasekhar, 1961). For this case, we study a different kind of intermittency in form of a radial inhomogeneity in the turbulence that was previously described by Coughlin & Marcus (1996) at lower Reynolds numbers. While the region near the inner cylinder is permanently turbulent, the outer region experiences bursts in the strength of turbulence over time (Brauckmann & Eckhardt, 2013b). In TC experiments, the presence of intermittent bursts has been confirmed up to Reynolds numbers of 10^6 (van Gils *et al.*, 2012). Such a subdivision of the turbulence with bursts on one side is not limited to TCF, but also occurs in rotating channel flow where an unstable and a stabilised side exist as well (Brethouwer *et al.*, 2014).

large-scale structures

Even if the turbulence is space-filling and persistent in time, it is not necessarily homogeneous but often shows large flow structures that underlie the small-scale fluctuations. For a wide range of rotation numbers in TCF, the Taylor vortices originating from the first instability persist up to the highly turbulent regime and thus structure the flow. Furthermore, many studies revealed that turbulent Taylor vortices also influence the angular momentum transport (Lathrop, Fineberg & Swinney, 1992a; Lewis & Swinney, 1999; Brauckmann & Eckhardt, 2013a; Martínez-Arias *et al.*, 2014), even at Reynolds numbers as high as $Re_S \sim 10^6$ (Huisman *et al.*, 2014). Such large-scale structures are also typical for other shear flows in the highly turbulent regime. Large vortices have been detected in the core region of plane Couette flow (Kitoh & Umeki, 2008; Avsarkisov *et al.*, 2014) as well as in pressure-driven channel and pipe flows (Monty *et al.*, 2007; Boersma, 2015). The momentum transport by the large-scale vortices results in long streaks of low or high streamwise velocity, which have been observed in BL flows as well (Smits, McKeon & Marusic, 2011).

Since they shape the turbulence, it is of interest how such large-scale vortices influence the angular momentum transport, and whether variations of the torque with the system rotation can be ascribed to changes in the strength of vortices. In the Delft TC experiment, the increase of torques with R_Ω was linked to a strengthening of the large-scale structures (Ravelet, Delfos & Westerweel, 2010; Tokgöz, 2014). In Brauckmann & Eckhardt (2013b), we introduced a method to quantify the torque contribution of the averaged Taylor vortices. Here, it will be used to study the connection between large-scale structures and the torque variation in a wide parameter range.

drag-reduction studies

We will see that large-scale structures, as well as small-scale vortices in the BL, influence the torque that measures the drag on both cylinder surfaces. Therefore, understanding the connection between flow structures and the torque is also relevant for industrial applications, where the reduction of drag is often of interest, for example to decrease fuel consumption of aeroplanes, boats and cars. Drag reduction can be achieved by modifying the turbulent flow structures or by manipulating the interaction of

the flow with the wall. Again, because of its closed and simple geometry, TCF has proven as a useful model system to study drag-reduction mechanisms. In TC experiments, drag reduction was achieved by adding polymer fibres (Tong *et al.*, 1990) or air bubbles to the water (van den Berg *et al.*, 2005, 2007; van Gils *et al.*, 2013) or by structuring the cylinder surface with riblets (Greidanus *et al.*, 2015).

1.5 OUTLINE OF THE THESIS

studied phenomena

Together with further studies summarised by Grossmann, Lohse & Sun (2016), this thesis contributes to the recent progress in the understanding of turbulent TCF in a wide parameter range. The numerical simulations presented here enable the investigation of a variety of turbulent phenomena in TCF that are also typical for other shear flows. These include intermittent bursts in conjunction with a radial inhomogeneity in the turbulence, influence of system rotation on the turbulence and angular momentum transport, curvature effects on the flow and the transition to a plane geometry for $\eta \to 1$, formation of large-scale structures in the turbulence and quantification of their contribution to the angular momentum transport, residual profile gradients in the middle that characterise the turbulent mixing, marginal stability behaviour of velocity profiles and the transition to turbulent BLs, influence of system rotation and cylinder curvature on the BLs, interaction of large-scale vortices with the BLs.

thesis outline

The outline of this thesis is as follows. Chapter 2 describes the numerical scheme used for the simulations of turbulent TCF, as well as the extensive validation of the simulation approach. The simulation convergence with spatial resolution is analysed based on computed torques, the energy balance and velocity profiles. To produce resolution-independent results, simulations have to fulfil three convergence requirements given in Chapter 2. Furthermore, effects of the domain size on computed torques and velocity profiles are discussed. As a final consistency check, the computed torques are compared to results from other studies. The chapter also provides an overview of the region in parameter space investigated in this thesis and of the used domain sizes and spatial resolutions.

In Chapter 3, the phenomenon of turbulent bursts and the formation of torque maxima as a function of the rotation are studied for $\eta = 0.5$, 0.71, 0.8 and 0.9, thus focusing on wide-gap TC systems. The critical rotation ratio for the onset of the bursting and the location of the torque maximum are determined for each radius ratio. In order to explain the bursting onset and its variation with radius ratio, Chapter 3 introduces a theoretical model that is based on stability properties of the turbulent flow and on the strength of large-scale vortices. Finally, the model prediction is compared to the simulation results. This chapter also discusses torque data by Wendt (1933) that are re-analysed in Appendix A.

Chapter 4 is devoted to the limit of vanishing curvature ($\eta \to 1$) and the transition from TCF to RPCF in the turbulent regime. First, it describes

the unified framework for a consistent study of the momentum transport in TCF and RPCF. It is analysed how curvature effects in TCF disappear for $\eta \to 1$, and how the turbulent behaviour approaches that of RPCF. The latter analysis includes the rotation dependence of the total momentum transport, large-scale vortices contributing to the momentum transport, angular momentum profiles and turbulent fluctuations. The turbulent mixing in TCF and RPCF is characterised by the profile gradients in the middle region.

The behaviour of low-curvature TCF is further analysed in Chapter 5. To explain the rotation dependence of torques and the shape of angular momentum profiles, a marginal stability model for TCF with independently rotating cylinders is introduced. The modelling approach is validated by comparing model predictions to numerical results. Discrepancies between model and simulation point to a change in the BL dynamics, which is further analysed in the simulations.

Finally, Chapter 6 provides an overview of the main results and conclusions of this study. Moreover, an outlook on questions for further research is given.

2 SIMULATION METHOD

This chapter describes the numerical method for the simulation of turbulent TCF and validates the simulation approach used for the investigations in the following chapters. We employ a spectral scheme that approximates a solution to the Navier–Stokes equations by expanding the velocity in basis functions, as described in Section 2.1. With increasing number of basis functions, the simulations converge, as demonstrated in Section 2.2. We assess the convergence based on computed torques and velocity profiles since these quantities will be of interest in the following investigations. Moreover, the influence of the domain size on computed torques and velocity profiles is discussed in Section 2.3. We provide an overview of the parameter space explored by the simulations and of their resolution characteristics in Section 2.4 and Section 2.5, respectively. As a final test, the computed torques are compared to various experimental torque measurements in Section 2.6.

2.1 NUMERICAL SCHEME

For our study of turbulent TCF, we perform direct numerical simulations (DNS) meaning that an approximate solution to the incompressible Navier–Stokes equations is computed. For the simulations, we use a Fortran code developed by Marc Avila and described in detail in Avila (2008) and Meseguer *et al.* (2007), which is furthermore similar to the spectral scheme used for pipe flow (Meseguer & Trefethen, 2003; Meseguer & Mellibovsky, 2007). Therefore, we here only summarise some key features of the numerical scheme.

To incorporate the cylindrical symmetry, the problem is formulated in cylindrical coordinates (r, φ, z) denoting the wall-normal, streamwise and spanwise directions, respectively. The flow in the annular domain is described by the velocity field $\boldsymbol{u} = (u_r, u_\varphi, u_z)$ and the pressure p, which have to satisfy the Navier–Stokes and continuity equations (1.3) with no-slip boundary conditions at the cylinder walls. Periodic boundary conditions are used in the axial direction. Similar to previous numerical studies of TCF (Moser, Moin & Leonard, 1983; Marcus, 1984a; Jones, 1985), the spectral scheme expands the velocity field with Fourier modes in the continuous directions and with Chebyshev polynomials in the radial direction. More precisely, the deviation $\boldsymbol{v} = \boldsymbol{u} - \boldsymbol{u}_b$ from the laminar base flow $\boldsymbol{u}_b$ is expanded in a vector field basis $\boldsymbol{\Phi}_{lnm}$,

$$\boldsymbol{v}(r, \varphi, z, t) = \sum_{l=-M_z}^{M_z} \sum_{n=-M_\varphi}^{M_\varphi} \sum_{m=0}^{M_r} a_{lnm}(t)\, \boldsymbol{\Phi}_{lnm}(r, \varphi, z), \qquad (2.1)$$

spectral expansion

with time-dependent complex coefficients a_{lnm} and the basis functions

basis functions

$$\boldsymbol{\Phi}_{lnm}(r,\varphi,z) = e^{i(lk_0 z + n n_{\mathrm{sym}}\varphi)}\, \boldsymbol{v}_{lnm}(r). \tag{2.2}$$

They fulfil the incompressibility condition $\boldsymbol{\nabla}\cdot\boldsymbol{\Phi}_{lnm} = 0$ and, at the cylinder walls, the boundary condition $\boldsymbol{v}_{lnm}(r_i) = \boldsymbol{v}_{lnm}(r_o) = \boldsymbol{0}$. For the three spatial directions, M_r, M_φ and M_z denote the highest order of modes used in the truncated series (2.1). The smallest axial wave number k_0 defines the axial domain height $L_z = 2\pi/k_0$, and the azimuthal periodicity $n_{\mathrm{sym}} \geq 1$ enables a reduction of the azimuthal length $L_\varphi = 2\pi r_a/n_{\mathrm{sym}}$ to minimise the computational effort. For instance, with a value of $n_{\mathrm{sym}} = 3$ only one third of the full cylinder circumference is simulated. This cylinder wedge periodically repeats three times. The basis vectors $\boldsymbol{v}_{lnm}(r)$ representing the radial variations are constructed from *Heinrichs basis* functions $h_m(x) = (1-x^2)T_m(x)$ and $g_m(x) = (1-x^2)^2 T_m(x)$ (Heinrichs, 1989). Compared to a pure *Chebyshev basis* $T_m(x)$, they reduce the condition number of the differentiation matrices and thereby improve the numerical stability, see also Boyd (2000, §7.7)

projection and integration in time

The spectral scheme is obtained by inserting the expansion (2.1) into the Navier–Stokes equations and projecting them with divergence-free test vector fields $\boldsymbol{\Psi}_{lnm}$, see Avila (2008) for details. Thereby, the pressure term vanishes, and a system of ordinary differential equations for the coefficients $a_{lnm}(t)$ is obtained. The equations are coupled by the non-linear term resulting from $(\boldsymbol{u}\cdot\boldsymbol{\nabla})\boldsymbol{u}$. After adding a small perturbation to the laminar base flow, the system of equations is integrated in time using a semi-implicit scheme, which stabilises the time stepping at low costs (Boyd, 2000, §12.5). The linear advection and Laplace terms are treated implicitly using fourth-order *backward differences* and the non-linear term is computed explicitly employing a modified fourth-order *Adams–Bashforth method*, resulting in a scheme denoted as $\mathrm{AB_4BD_4}$ (Cox & Matthews, 2002). For pipe flow, Meseguer & Mellibovsky (2007) showed that the accuracy of this time-stepping scheme is mainly limited by the spatial resolution and not by the temporal one: With decreasing time step, the error converges to the level prescribed by the spatial resolution. Since their spectral method for pipe flow is similar to the one for TCF, we expect such a convergence behaviour also here.

The numerical code is extensively tested, as it was successfully used in several studies of TCF. These include spiral flow (Meseguer *et al.*, 2009a) as well as spiral turbulence for counter-rotating cylinders (Meseguer *et al.*, 2009b) and variants of TCF with axial through-flow (Avila, Meseguer & Marques, 2006), harmonic axial motion of the inner cylinder (Avila *et al.*, 2007) and harmonic oscillation of the inner cylinder rotation speed (Avila *et al.*, 2008). It was also used for the simulations of turbulent TCF in Brauckmann & Eckhardt (2013a).

Our investigations in Chapter 4 and Chapter 5 include simulations with strongly co-rotating cylinders so that high rotation numbers R_Ω can be reached for large cylinder radii. In these cases, the fluid rotates fast,

and flow structures are quickly advected in the azimuthal direction. Consequently, the advection speed is not determined by the velocity difference between the cylinders but by their individual velocities, which in our investigations are up to 47 times larger. Such high velocities render the numerical integrator unstable and would require a smaller time step in the inertial reference frame, in which the numerical scheme was originally formulated. To overcome these restrictions, in the strongly co-rotating cases, we perform the simulations in the reference frame rotating with the angular velocity $\boldsymbol{\Omega}_{\mathrm{rf}} = \Omega_{\mathrm{rf}} \boldsymbol{e}_z$. The transformation from the velocity $\hat{\boldsymbol{u}}$ and pressure $\hat{p}$ in the inertial reference frame to $\boldsymbol{u}$ and p in the rotating frame is given by

change to rotating reference frame

$$\begin{aligned} \boldsymbol{u}(r,\varphi,z,t) &= \hat{\boldsymbol{u}}(r,\varphi+\widetilde{\Omega}_{\mathrm{rf}}t,z,t) - r\widetilde{\Omega}_{\mathrm{rf}}\boldsymbol{e}_\varphi, \\ p(r,\varphi,z,t) &= \hat{p}(r,\varphi+\widetilde{\Omega}_{\mathrm{rf}}t,z,t) - \frac{r^2\widetilde{\Omega}_{\mathrm{rf}}^2}{2}, \end{aligned} \tag{2.3}$$

with the non-dimensionalised angular velocity $\widetilde{\Omega}_{\mathrm{rf}} = \Omega_{\mathrm{rf}}\, d/U_0$. The additional pressure term is chosen such that its radial gradient $\partial_r p$ cancels the centrifugal acceleration $r\widetilde{\Omega}_{\mathrm{rf}}^2$. By inserting the expressions (2.3) for the pressure $\hat{p}$ and the velocity components $\hat{u}_i$, as well as their time derivatives $\partial_t \hat{u}_i = \partial_t u_i - \widetilde{\Omega}_{\mathrm{rf}}\partial_\varphi u_i$, into the Navier–Stokes equations in the inertial frame of reference (Landau & Lifshitz, 1987), one obtains

$$\partial_t \boldsymbol{u} + (\boldsymbol{u}\cdot\boldsymbol{\nabla})\boldsymbol{u} = -\boldsymbol{\nabla} p + \frac{1}{Re_S}\Delta\boldsymbol{u} - 2\widetilde{\Omega}_{\mathrm{rf}}\boldsymbol{e}_z \times \boldsymbol{u}, \tag{2.4}$$

the Navier–Stokes equations in the rotating reference frame. In addition to the formulation in the inertial frame, it includes the Coriolis acceleration $-R_\Omega \boldsymbol{e}_z \times \boldsymbol{u}$ with $R_\Omega = 2\widetilde{\Omega}_{\mathrm{rf}}$. Thus, the change to the rotating frame is achieved by implementing the transformation (2.3) as well as the Coriolis acceleration in the Fortran code. As the Coriolis term is linear in $\boldsymbol{u}$, it is treated implicitly by the integration scheme.

2.2 CONVERGENCE TESTS

In the following, we analyse how one typical turbulent simulation converges with increasing spatial resolution. Since we are not able to repeat every simulation with various spectral resolutions to test for convergence, other criteria computable from one single simulation are needed to estimate the quality of convergence. The following three criteria will be utilised.

radial independence of Nusselt number

The first criterion is based on the radial independence of the angular momentum current J^ω, equation (1.8), which implies that the torques at the inner and outer cylinder coincide. However, numerical approximation errors can lead to deviations from this J^ω balance. Therefore, for a converged computation, both torque values have to agree within their fluctuations, see also Marcus (1984a) and Dong (2007). The radial independence of J^ω also implies that the ratio $Nu_\omega = J^\omega / J^\omega_{\mathrm{lam}}$ should be constant over r. Therefore, we also test for radial variations of $Nu_\omega(r)$ over the complete

cylinder gap, which was suggested as a criterion by Ostilla *et al.* (2013) and is more strict than checking the torque relation at r_i and r_o alone.

Second, to assess the convergence of the spatial resolution, we calculate the amplitude of the highest mode in each direction, $\widetilde{a}_r$, $\widetilde{a}_\varphi$ and $\widetilde{a}_z$, defined as the maximum norm of the spectral coefficients a_{lnm} for $m = M_r$, $n = \pm M_\varphi$ and $l = \pm M_z$, respectively,

amplitude of last coefficient

$$\widetilde{a}_r = \max_{l,n} |a_{lnM_r}| / a_{\max}\,, \qquad \widetilde{a}_\varphi = \max_{l,m} \left\{ |a_{lM_\varphi m}|,\ |a_{l-M_\varphi m}| \right\} / a_{\max}\,, \qquad \widetilde{a}_z = \max_{n,m} \{ |a_{M_z nm}|,\ |a_{-M_z nm}| \} / a_{\max}\,. \tag{2.5}$$

In addition, these amplitudes are measured in relation to the globally strongest mode $a_{\max} = \max_{l,n,m} |a_{lnm}|$. Since Fourier and Chebyshev series of smooth functions often converge exponentially, the amplitude of the last coefficient serves as an estimate for the truncation error of the spectral expansion in the corresponding direction, see Boyd (2000, §2.12). Consequently, for an adequately resolved simulation, the relative amplitudes $\widetilde{a}_r$, $\widetilde{a}_\varphi$ and $\widetilde{a}_z$ should be sufficiently small and of similar magnitude.

As a third criterion, we measure the deviation from the energy balance (1.12) which states that, on average, the energy input must equal the volume energy dissipation rate $\widetilde{\varepsilon}$. While $\widetilde{\varepsilon} = Nu_\omega / Re_S$ is an exact relation derived from the Navier–Stokes equations, under-resolved simulations do not satisfy this relation because of approximation errors. Therefore, the relative deviation from the energy balance,

deviation from energy balance

$$\Delta\varepsilon = \frac{Nu_\omega / Re_S - \widetilde{\varepsilon}}{\widetilde{\varepsilon}} \qquad \text{with} \qquad \widetilde{\varepsilon} = \frac{1}{2Re_S} \left\langle \left(\partial_i u_j + \partial_j u_i \right)^2 \right\rangle_{V,t}, \tag{2.6}$$

has to be small for a converged simulation. This criterion was previously used by Marcus (1984a) to test the numerical accuracy, and an analogous criterion for the thermal dissipation rate in Rayleigh–Bénard convection was discussed by Stevens, Verzicco & Lohse (2010).

test case

For illustration, we analyse these criteria for one representative simulation with $\eta = 5/7$, $Re_S = 9452.1605$ and stationary outer cylinder. This shear Reynolds number ($\sim 10^4$) is typical for the remaining simulations, which are performed in the range $5 \times 10^3 \leq Re_S \leq 2 \times 10^4$. Furthermore, only rotating the inner cylinder corresponds to the classical mode of operation of TC experiments, where a radius ratio near $\eta = 5/7 \approx 0.7$ was used frequently. The simulation domain has a height of $L_z = 2\pi/3 \approx 2$, which is sufficiently tall to host one pair of counter-rotating Taylor vortices. By imposing the azimuthal periodicity $n_{\text{sym}} = 6$, the downstream length of the domain is reduced to $L_\varphi = \pi$, which has previously been identified to be sufficient for an accurate torque computation (Brauckmann, 2011). In addition to the sensitivity of the torque, we here also analyse whether velocity profiles are influenced by the restricted domain size. For this test case, we perform simulations at six different spectral resolutions, and two additional simulations in domains that are twice as long or three times higher than the original domain, with results listed in Table 2.1.

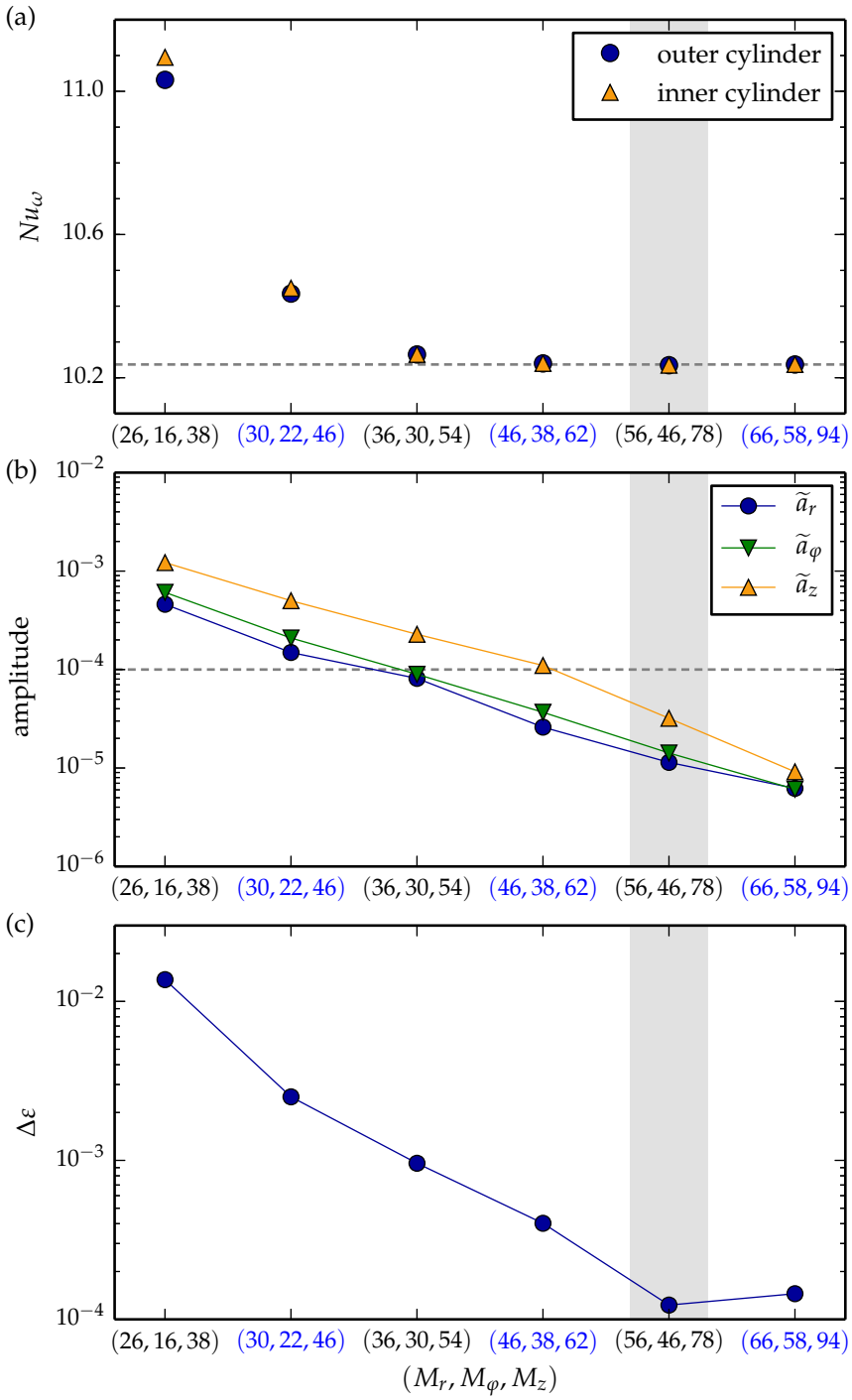

FIGURE 2.1: Convergence with increasing spectral resolution (M_r, M_φ, M_z), analysed for a simulation with $\eta = 5/7$, $Re_S = 9452.1605$, $L_z = 2\pi/3$, $n_{\text{sym}} = 6$ and a stationary outer cylinder. Convergence is assessed by (a) the torque computed at both cylinders, (b) the amplitude of the highest modes and (c) the deviation from the energy balance. The dashed line in (a) marks the result $Nu_\omega = 10.237$ at the highest resolution. Uncertainties in Nu_ω due to temporal fluctuations are much smaller than the symbol size. For the amplitudes, we identified a convergence threshold of 10^{-4} indicated by the dashed line in (b). For subsequent simulations at $Re_S = 10^4$, we use approximately the resolution highlighted by the grey area. Profiles of simulations labelled in blue are compared in Figures 2.2, 2.3 and 2.4.

$L_r \times L_\varphi \times L_z$	$M_r \times M_\varphi \times M_z$	$10^4\,(\widetilde{a}_r,\, \widetilde{a}_\varphi,\, \widetilde{a}_z)$	$100\Delta\varepsilon$	Nu_ω
$1 \times \pi \times 2\pi/3$	$26 \times 16 \times 38$	4.60, 6.08, 12.2	1.37	11.095
$1 \times \pi \times 2\pi/3$	$30 \times 22 \times 46$	1.49, 2.09, 5.00	0.25	10.450
$1 \times \pi \times 2\pi/3$	$36 \times 30 \times 54$	0.81, 0.90, 2.28	0.10	10.265
$1 \times \pi \times 2\pi/3$	$46 \times 38 \times 62$	0.26, 0.37, 1.10	0.04	10.240
$1 \times \pi \times 2\pi/3$	$56 \times 46 \times 78$	0.11, 0.14, 0.32	0.01	10.235
$1 \times \pi \times 2\pi/3$	$66 \times 58 \times 94$	0.06, 0.06, 0.09	0.01	10.237
$1 \times 2\pi \times 2\pi/3$	$56 \times 94 \times 78$	0.10, 0.11, 0.35	0.01	10.232
$1 \times \pi \times 2\pi$	$56 \times 46 \times 238$	0.08, 0.10, 0.17	0.01	10.271

TABLE 2.1: Simulations used to test the effect of spatial resolution and domain size for $\eta = 5/7$, $Re_S = 9452.1605$ and a stationary outer cylinder. L_r, L_φ and L_z denote the radial, azimuthal and axial domain length, and M_r, M_φ, M_z give the highest order of spectral modes in the corresponding direction. The azimuthal length is $L_\varphi = 2\pi r_a / n_{\mathrm{sym}}$ with the mean radius $r_a = (r_i + r_o)/2$ and the imposed azimuthal periodicity $n_{\mathrm{sym}} = 6$ for $L_\varphi = \pi$. The relative amplitudes of the highest spectral modes $\widetilde{a}_r$, $\widetilde{a}_\varphi$ and $\widetilde{a}_z$ estimate the truncation error of the expansion in each direction. The last two columns show the relative deviation from the energy balance $\Delta\varepsilon$ and the Nusselt number Nu_ω computed at the inner cylinder.

convergence analysis

Figure 2.1 shows the convergence of the simulations with increasing spectral resolution (M_r, M_φ, M_z) in terms of the three criteria defined above. In (a), the torque (given as $Nu_\omega = G/G_{\mathrm{lam}}$) decreases with increasing number of modes and converges to a resolution-independent value only for (M_r, M_φ, M_z) above $(36, 30, 54)$. At the lowest resolution, the torque values computed at the inner and outer cylinder clearly differ from each other. They start to agree within their statistical uncertainties of 0.07% at the resolution $(36, 30, 54)$ where Nu_ω becomes resolution-independent. Consequently, the agreement of inner and outer torques constitutes one requirement for a converged torque computation. For the three highest resolutions, the Nusselt numbers of different simulations are equal to within 0.05% and approach $Nu_\omega = 10.24$. Furthermore, the amplitudes of the highest spectral modes decrease with increasing resolution, see sub-figure (b). For the resolution $(36, 30, 54)$ where the torque converges, the relative amplitudes reach a level of $\sim 10^{-4}$ and drop below it for even higher resolutions. This suggests that at least four orders of magnitude should be represented by the spectral expansion in each direction for a converged computation. In sub-figure (c), the deviation from the energy balance is 0.1% at the threshold for torque convergence $(36, 30, 54)$, and it decreases further with increasing resolution.* Note that the final level of $\Delta\varepsilon \sim 0.01\%$ is already below the statistical uncertainty of 0.07%,

* Checking the implementation of the calculation of $\widetilde{\varepsilon}$ again, it was noticed that the deviation $\Delta\varepsilon$ is more than a factor of 10 smaller than reported in Brauckmann & Eckhardt (2013a). The value quoted here is the corrected one.

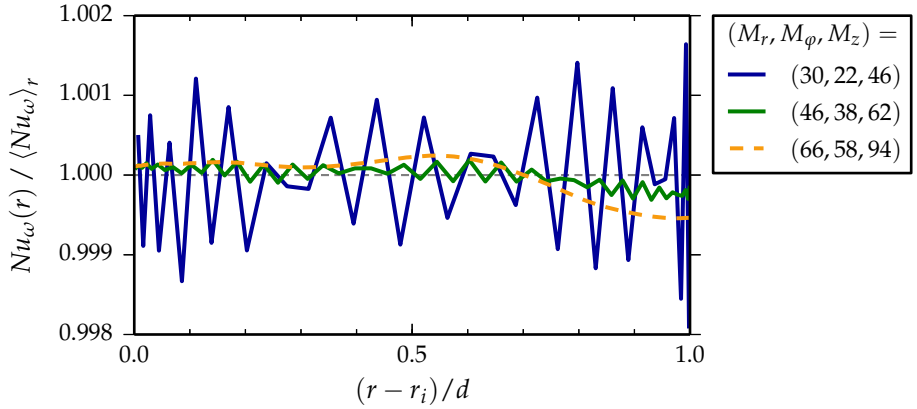

FIGURE 2.2: Radial variation of the Nusselt number for three spectral resolutions (M_r, M_φ, M_z). The profiles $Nu_\omega(r)$ are normalised by the mean value $\langle Nu_\omega \rangle_r$. As a reference, the dotted line marks the theoretically expected value 1. For simulation parameters see Figure 2.1.

and even smaller values are therefore difficult to achieve. The convergence characteristics discussed here seem to be more general, since we observed a similar behaviour at $Re_S \approx 5 \times 10^3$ for a stationary outer cylinder (Brauckmann & Eckhardt, 2013a) and for exact counter-rotation (Brauckmann, 2011).

convergence requirements

Overall, we summarise the following convergence requirements: Agreement of the torque values at the inner and outer cylinder within the statistical uncertainty, decay of the relative amplitudes of the highest modes $\widetilde{a}_r$, $\widetilde{a}_\varphi$ and $\widetilde{a}_z$ to $\sim 10^{-4}$ and a deviation $\Delta\varepsilon$ from the energy balance of at most 0.1%. All subsequent simulations conform with these three convergence criteria. For instance, all simulations at $Re_S = 10^4$ (close to the $Re_S = 9452.1605$ analysed here) use a spatial resolution corresponding to $(M_r, M_\varphi, M_z) = (50, 46, 78)$, which is marked by the grey area in Figure 2.1 and clearly lies inside the region of convergence.

test for radially constant Nu_ω

In the following, we test whether a simulation that meets these three convergence requirements also results in a constant Nusselt number profile $Nu_\omega(r) = J^\omega(r)/J^\omega_{\text{lam}}$ over the full cylinder gap. So far, we only verified that the torque values at both cylinders coincide for a converged simulation. However, the requirement that the profile $Nu_\omega(r)$ should be constant for all radii $r \in [r_i, r_o]$ is more strict. To test this property, Figure 2.2 shows profiles of the Nusselt number for a non-converged $(M_r, M_\varphi, M_z) = (30, 22, 46)$, a just converged $(46, 38, 62)$ and a highly resolved $(66, 58, 94)$ simulation (labelled in blue in Figure 2.1). The non-converged simulation results in peak-to-peak Nu_ω-variations of 0.35%. For the two higher resolved simulations, the variations drop below 0.1% and hence approximately reach the accuracy level $\Delta\varepsilon$ achieved in the energy balance. Moreover, the radial fluctuations of Nu_ω are of similar amplitude over the entire cylinder gap. In the highly resolved simulation, the radial Nu_ω-variations are smaller than the statistical uncertainty due to temporal fluctuations. Thus, even smaller variations are difficult to achieve because

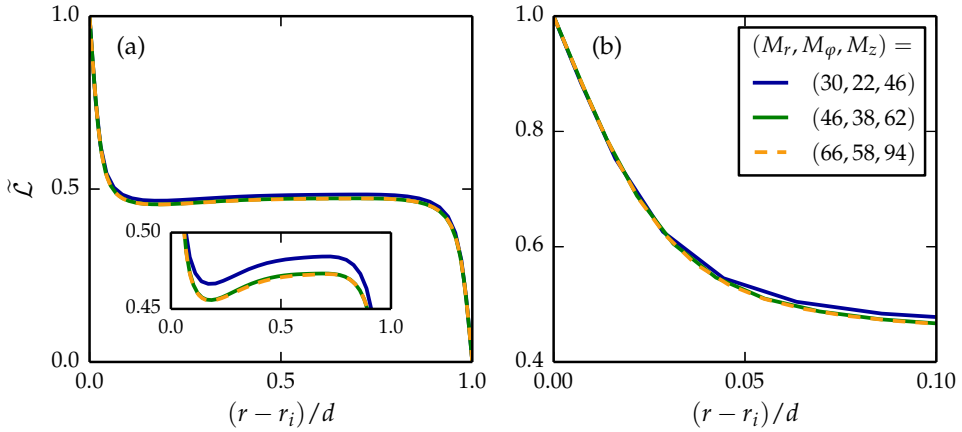

FIGURE 2.3: Convergence of angular momentum profiles with increasing spectral resolution. The specific angular momentum profile $\langle \hat{\mathcal{L}} \rangle = r\langle \hat{u}_\varphi \rangle$ in the inertial frame is rescaled as $\widetilde{\mathcal{L}} = (\langle \hat{\mathcal{L}} \rangle - \mathcal{L}_o)/(\mathcal{L}_i - \mathcal{L}_o)$, where $\mathcal{L}_i$ and $\mathcal{L}_o$ denote the corresponding values at the inner and outer cylinder. Magnifications of the inner BL and central region of the profile in (a) are shown in (b) and in the inset of (a), respectively, and demonstrate the good agreement between the two higher resolved profiles. For simulation parameters see Figure 2.1.

of the limitation of computing time. In conclusion, the deviation from the radial independence of Nu_ω certainly lies below 0.1% for the two converged cases shown here.

velocity profile convergence

We furthermore test whether the observed convergence of global quantities, such as mean torques and energy dissipation, also implies that the velocity profiles are converged. For this purpose, we compare profiles of mean and fluctuating velocities from the non-converged, just converged and highly resolved simulations at the resolutions labelled in blue in Figure 2.1. As the mean profile, Figure 2.3 shows the angular momentum profile $\langle \hat{\mathcal{L}} \rangle = r\langle \hat{u}_\varphi \rangle$ in the inertial reference frame, where it becomes almost flat in the middle. The profiles of the two converged simulations collapse, whereas the low-resolved profile clearly deviates from the other two. The deviation becomes most noticeable in the central region detailed in the inset of (a), where the low resolution results in a larger angular momentum level. Since we will later discuss that the slightly positive profile slope in the centre observed here is a general feature, it is important to note that the profile slope does not change with the spectral resolution. The high quality of agreement between the two higher resolved profiles can be estimated from the magnifications of the central region and inner BL in (a) and (b), respectively. Even in the BL, where a high spatial resolution is needed to represent strong local gradients emerging from small flow structures, no difference between the two higher resolved profiles is discernible. This demonstrates the advantage of using Chebyshev polynomials in the radial direction, since they easily resolve thin BLs close to the walls (Orszag & Israeli, 1974) due to a clustering of grid points in this region (Boyd, 2000, §2.16).

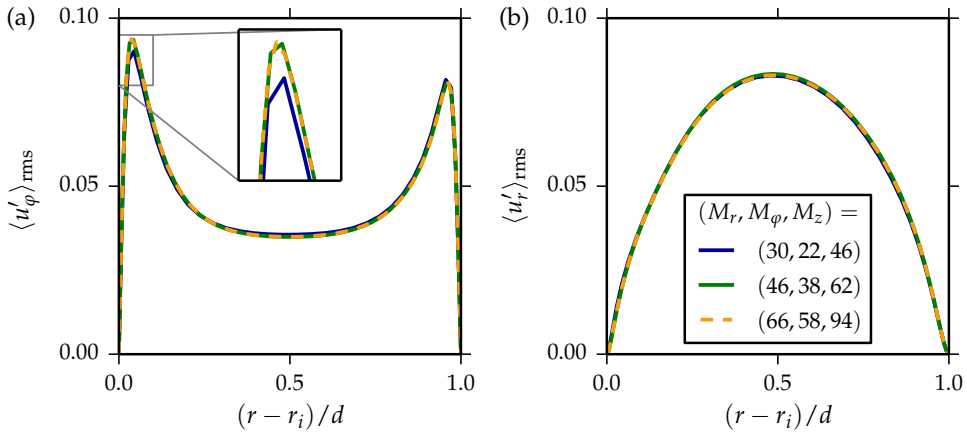

FIGURE 2.4: Convergence of root-mean-square (RMS) profiles of (a) the azimuthal and (b) the radial velocity, which are based on the fluctuations $u'_i = u_i - \langle u_i \rangle$ around the mean profile $\langle u_i \rangle$. Only the lowest resolved profile slightly deviates as is noticeable in (a). For simulation parameters see Figure 2.1.

To further test the simulation convergence, we compare local velocity fluctuations at different resolutions. For this purpose, Figure 2.4 shows root-mean-square (RMS) profiles of velocity fluctuations $u'_i = u_i - \langle u_i \rangle$ around the mean profile $\langle u_i \rangle$ for the azimuthal and radial component. Only the lowest resolution $(30, 22, 46)$ results in slightly deviating RMS profiles, whereas the profiles for the two higher resolutions agree well. The small deviation is more noticeable for the azimuthal velocity fluctuations in (a), especially at the left peak detailed in the inset. This observation suggests that a proper resolution is more critical for the inner BL than for the outer one, consistent with the fact that the viscous length scale at the inner cylinder is a factor η smaller than the outer viscous length scale, see e.g. Huisman *et al.* (2013).

In summary, we identified three convergence requirements and demonstrated for one representative test case that, when a simulation meets these requirements, the mean torque as well as mean and RMS velocity profiles become resolution-independent. For the test case, we furthermore found that the converged simulations fulfil the radial independence of $Nu_\omega(r)$ to within 0.1%. All subsequent simulations satisfy the three convergence criteria and are therefore expected to result in converged torque values and velocity profiles.

2.3 DOMAIN SIZE EFFECTS

In addition to the spatial resolution, the torque computation may also depend on the size of the simulation domain, and we expect it to become size-independent for large domains. This expectation is based on the idea that the turbulent statistics result from flow structures, which only form if they can fit into the domain. In case of a sufficiently large domain, a further increase in size would enable repetitions of the same flow structures,

which do not alter the turbulent statistics for the following reason: In an ergodic system, averaging over many realisations in space is expected to give the same result as averaging only one flow-structure realisation over long times. In contrast, if some essential flow structures can not be represented in a too small domain, some relevant contributions to the turbulent statistics are lost.

effect of Taylor vortices

This idea is clarified by the example of Taylor vortices that typically dominate TCF in the linearly unstable regime and still exist at high shear rates. These flow structures consist of two counter-rotating vortices that wind around the inner cylinder and have a diameter of approximately one gap width (Taylor, 1923; Koschmieder, 1993). However, depending on the experimental start-up procedure, Taylor vortices of various axial heights can be obtained for the same cylinder rotation speeds (Coles, 1965). For axisymmetric Taylor vortex flow, the computations by Riecke & Paap (1986) showed that the torque depends on the vortex height. Our simulations with stationary outer cylinder in Brauckmann & Eckhardt (2013a) revealed that the torque as a function of vortex size exhibits a maximum at the axial vortex wavelength $\lambda_z = 1.93$. More importantly, this study showed that, when simulating two or three vortex pairs in a domain of double or triple height, the torque remains the same as the vortex size is unchanged. This confirms the aforementioned ergodic behaviour and demonstrates that simulating only a single Taylor vortex pair suffices for an accurate torque computation. However, changing the axial height of Taylor vortices can affect the turbulent statistics as also noted by Ostilla-Mónico, Verzicco & Lohse (2015). In the following investigations, we simulate domains with a height of $L_z = 2$. When Taylor vortices are present in the flow, such domains contain a single vortex pair. Thereby, we fix the wavelength of the Taylor vortex pair to $\lambda_z = 2$, which is close to the maximum at $\lambda_z = 1.93$. It is important to note that in TC experiments a cylinder height of $L_z \sim 10$ also restricts the wavelength of Taylor vortices to discrete possible values. Such discrete vortex states can lead to non-unique results even at Reynolds numbers $Re_S \sim 10^6$ (Huisman *et al.*, 2014).

azimuthal domain length

Similarly, the azimuthal domain length may affect the representable flow structures and, thereby, the turbulent statistics. Naturally, the azimuthal length at the mean radius r_a is $L_\varphi = 2\pi r_a$, but in simulations it can be reduced to $L_\varphi = 2\pi r_a / n_{\mathrm{sym}}$ by imposing a higher rotational symmetry $n_{\mathrm{sym}} > 1$. This represents a restriction on the largest azimuthal wavelength that can be represented. For $\eta = 0.71$, $Re_i = 8000$ and stationary outer cylinder, we found that the rotational symmetry can be increased to $n_{\mathrm{sym}} = 9$ while still maintaining an accurate result for the torque (Brauckmann, 2011). This periodicity corresponds to an azimuthal length of $L_\varphi \approx 2.1$, which is still longer than the correlation length of velocity fluctuations in the DNS. Similarly for $\eta = 0.909$ and $Re_i = 10^5$, Ostilla-Mónico, Verzicco & Lohse (2015) found that their smallest simulation domain with $L_\varphi \approx 3.3$ already results in accurate torques and mean azimuthal velocity profiles.

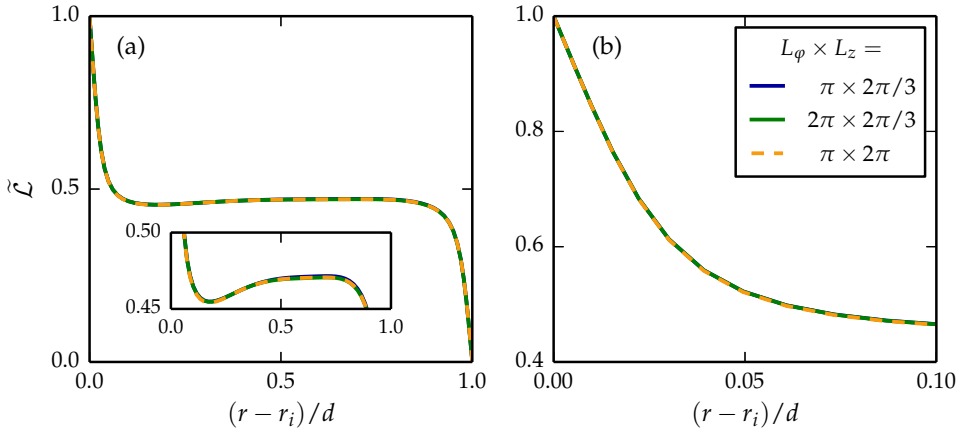

FIGURE 2.5: Profiles of the rescaled angular momentum $\widetilde{\mathcal{L}}$ for three different domain sizes and the remaining parameters as in Figure 2.1. For the two larger domains, the spectral resolution of the smallest domain $(56, 46, 78)$ is increased with L_φ and L_z, respectively, cf. Table 2.1. Magnifications of the inner BL and central region of the profile in (a) are shown in (b) and in the inset of (a), respectively.

Extending our previous analysis at lower Re_S, we here also test the effect of the domain size on mean and RMS profiles for $Re_S \approx 10^4$. To this end, we compare the original converged simulation to results obtained in domains that are two times longer ($L_\varphi = 2\pi$) or three times higher ($L_z = 2\pi$) with correspondingly adjusted spatial resolution, see bottom rows of Table 2.1. The domain with $L_z = 2\pi$ contains three Taylor vortex pairs so that their axial wavelength remains unchanged compared to simulations of one pair with the height $L_z = 2\pi/3$. Similar to previous observations, the relative deviation between the torques from the three domains is less than 0.4%, which is of the same order of magnitude as the statistical uncertainty. Moreover, the mean angular momentum profiles from the three domains collapse, as shown in Figure 2.5. Even in the magnifications of the central region and of the inner BL, the profiles do not differ, as their maximal pointwise deviation is 0.4% and may also be affected by statistical uncertainties. However, the RMS velocity profiles in Figure 2.6 show small deviations of maximally 1.7%. The two larger domains especially result in slightly increased radial velocity fluctuations in (b), while on average the deviations seem to be smaller for the azimuthal component in (a).

In conclusion, a domain of length $L_\varphi \approx 3$, which contains only a single vortex pair, is sufficiently large to generate accurate results for the torque and mean velocity profile. Moreover, simulating longer domains or more vortex pairs of the same size only slightly changes the velocity fluctuations and does not alter the mean values. On the other hand, in domains containing only one vortex pair, Ostilla-Mónico, Verzicco & Lohse (2015) found that the fluctuations depend on the domain height. However, they noted that this effect is caused by the changing axial wavelength of the Taylor vortices and not by the change in height itself.

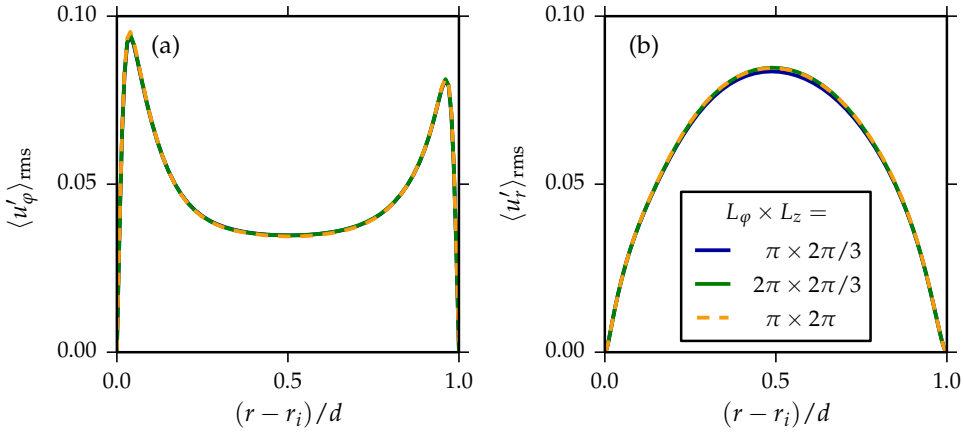

FIGURE 2.6: RMS profiles of (a) the azimuthal and (b) the radial velocity fluctuations for three different domain sizes and the remaining parameters as in Figure 2.1. The spectral resolution is adapted to the domain size, cf. Table 2.1. In the larger domains, the radial velocity fluctuations are slightly enhanced in the central region.

2.4 INVESTIGATED PARAMETER RANGE†

We here summarise the points (R_C, Re_S, R_Ω) in parameter space explored by simulations for our investigations in the following chapters. All three parameters are varied to analyse their influence on the turbulence. Studies for different η (or curvature numbers $R_C = (1-\eta)/\sqrt{\eta}$) analyse the effect of system curvature and give information on when the properties of RPCF emerge from TCF. Studies of different Re_S and R_Ω give information on the impact of shear and rotation on the turbulence. The range of parameters explored is indicated in Figure 2.7. They were selected as follows.

selected parameter values

For each curvature number R_C the evolution of the rotation dependence is analysed with increasing shear. To this end, we realise various mean rotation states for three shear Reynolds numbers $Re_S = 5 \times 10^3$, 1×10^4 and 2×10^4. Since we adopt some of the results for $\eta = 0.71$ from our previous study (Brauckmann & Eckhardt, 2013a), the simulated values of $Re_S = 3899$, 8772, 19737 deviate slightly from the target values, as indicated in Figure 2.7(a). In the following, we will skip over these small differences in Re_S, as they are not significant within statistical fluctuations. Our highest value of Re_S lies in the range where the transition to the fully turbulent state was observed in experiments for $\eta \sim 0.7$ and stationary outer cylinder (Lathrop, Fineberg & Swinney, 1992a; Lewis & Swinney, 1999). We performed simulations for the range of rotation numbers R_Ω where the occurrence of a torque maximum was observed for medium radius ratios η (Dubrulle *et al.*, 2005; Paoletti & Lathrop, 2011; van Gils *et al.*, 2011; Paoletti *et al.*, 2012; Brauckmann & Eckhardt, 2013a; Merbold, Brauckmann & Egbers, 2013; Ostilla *et al.*, 2013); this allowed us to extend these studies

† The text of this and the next section follows closely the representation in H. J. Brauckmann, M. Salewski & B. Eckhardt (2016). Momentum transport in Taylor–Couette flow with vanishing curvature. *J. Fluid Mech.* 790: 419–452.

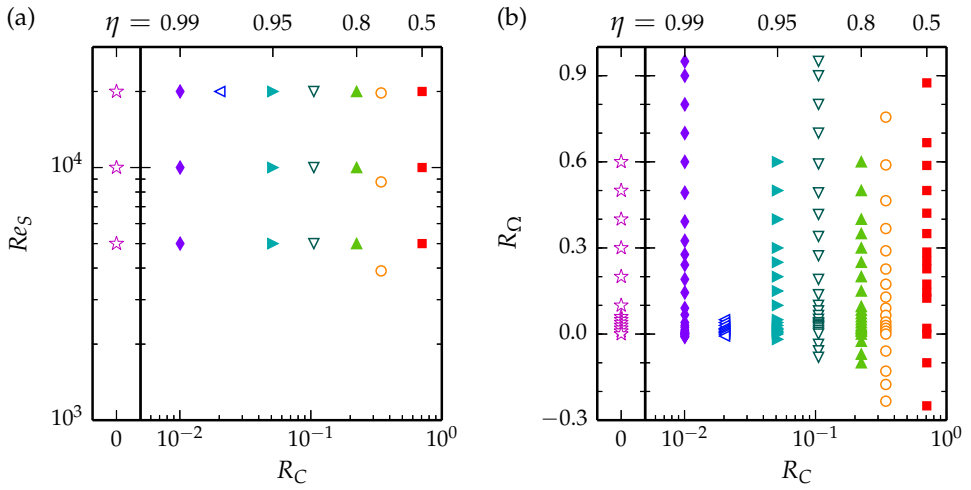

FIGURE 2.7: Parameter space (R_C, Re_S, R_Ω) explored by DNS of TCF and RPCF to study the limit of vanishing curvature, i.e. $R_C \to 0$ equivalent to $\eta \to 1$. The curvature numbers $R_C = (1-\eta)/\sqrt{\eta}$ correspond to the radius ratios $\eta = 0.99$, 0.98, 0.95, 0.9, 0.8, 0.71 and 0.5, and the extra columns for $R_C = 0$ summarise RPCF simulations by Matthew Salewski. (a) For the shear Reynolds numbers Re_S and curvature numbers R_C indicated here, several simulations with $R_\Omega \in (-0.3, 0.95)$ were performed. (b) The range of rotation numbers R_Ω explored is shown here for $Re_S = 2 \times 10^4$ and different curvature numbers R_C. Symbols and colours for R_C (and η) as used in Chapter 4.

to η close to one. Moreover, rotation numbers that correspond to strong counter-rotation $\mu < 0$ were selected in order to study the turbulent intermittency in the outer region (Coughlin & Marcus, 1996; van Gils *et al.*, 2012; Brauckmann & Eckhardt, 2013b). Thus, the simulated rotation numbers lie mainly in the range $-0.1 \leq R_\Omega \leq 0.6$ as shown in Figure 2.7(b), except for $R_C = 0.02$ ($\eta = 0.98$) where we focus on a narrow range in R_Ω for a study of the turbulent intermittency for counter-rotation. The case of no system rotation, i.e. $R_\Omega = 0$, corresponds to counter-rotating cylinders with $\omega_o = -\eta\omega_i$. For the highest shear Reynolds number $Re_S = 2 \times 10^4$, the evolution of the rotation dependence is studied for seven curvature numbers $R_C > 0$ (TCF) and for $R_C = 0$ (RPCF), as listed in Table 2.2. All RPCF results were provided by Matthew Salewski.

2.5 SIMULATED DOMAINS AND SPATIAL RESOLUTION

selected domain size

In our simulations of TCF and RPCF, we introduce a spanwise (axial) periodicity of length $L_z = 2$ which is large enough to accommodate one pair of counter-rotating Taylor vortices. As we will see in Section 3.4 and Section 4.4, turbulent Taylor vortices are the typical flow structures at and around the torque maximum, and they are suppressed for strongly co- or counter-rotating cylinders (Brauckmann & Eckhardt, 2013b; Huisman *et al.*, 2014; Ostilla-Mónico *et al.*, 2014c). In RPCF, and as will be shown in large radius ratio TCF (Chapter 4), there can exist two peaks in the mo-

η	R_C	n_{sym}	$L_r \times L_\varphi \times L_z$	$M_r \times M_\varphi \times M_z$
0.50	0.707	3	$1 \times \pi \times 2$	$70 \times 62 \times 190$
0.71	0.344	6	$1 \times 3.09 \times 2$	$70 \times 78 \times 110$
0.80	0.224	7	$1 \times 4.04 \times 2$	$70 \times 94 \times 94$
0.90	0.105	15	$1 \times 3.98 \times 2$	$70 \times 94 \times 94$
0.95	0.051	30	$1 \times 4.08 \times 2$	$70 \times 94 \times 94$
0.98	0.020	78	$1 \times 3.99 \times 2$	$70 \times 94 \times 94$
0.99	0.010	99	$1 \times 6.31 \times 2$	$70 \times 158 \times 94$
1	0	–	$1 \times 2\pi \times 2$	$76 \times 159 \times 95$

TABLE 2.2: Domain size and spatial resolution at the highest $Re_S = 2 \times 10^4$ for the different radius ratios η and corresponding curvature numbers R_C. The azimuthal periodicity n_{sym} was introduced for the TC simulations to reduce the natural azimuthal length to $L_\varphi = 2\pi r_a / n_{\text{sym}}$ with the mean radius $r_a = (r_i + r_o)/2$, while the wall-normal (radial) and spanwise (axial) lengths were kept at $L_r = 1$ and $L_z = 2$. M_r, M_φ and M_z give the highest order of spectral modes in the corresponding direction. For RPCF in the bottom line, the coordinates r and φ correspond to y and x. For resulting truncation error and grid spacing see Table 2.3.

mentum transport, both of which show turbulent Taylor vortices (Salewski & Eckhardt, 2015). In the cases studied here, the flows near the maxima typically consist of a single vortex pair. Corresponding flow visualisations are shown in Brauckmann & Eckhardt (2013a) for TCF and in Salewski & Eckhardt (2015) for RPCF with $L_z = \pi$. In addition, a streamwise periodicity of length $L_x = 2\pi$ was assumed in the RPCF simulations, while TCF is naturally periodic in this direction. However, we only simulated a domain of reduced azimuthal length L_φ that repeats n_{sym} times to fill the entire cylinder circumference. For $\eta = 0.5$ and $\eta = 0.71$ we tested that the reduced azimuthal length does not bias the computed torques for a stationary outer cylinder. The length L_φ was further increased for larger radius ratios, see Table 2.2. As shown in Section 2.3 and Ostilla-Mónico, Verzicco & Lohse (2015), the effects of these geometrical constraints of the domain are small for single point quantities, like the torque and profiles studied here.

RPCF code

The RPCF simulations were performed with the *Channelflow* code (Gibson, Halcrow & Cvitanović, 2008; Gibson, 2012). As the TC code described in Section 2.1, it employs a pseudospectral scheme which was modified to include the Coriolis force, $-R_\Omega \boldsymbol{e}_z \times \boldsymbol{u}$, caused by the spanwise rotation. Both numerical codes use an expansion of the velocity field in Fourier modes in the two periodic directions and in Chebyshev polynomials in the wall-normal direction, and employ a semi-implicit scheme for the time stepping. For simplicity, in the RPCF simulations, we also denote the highest order of modes in the wall-normal, streamwise and spanwise dir-

η	$10^4\,(\widetilde{a}_r,\ \widetilde{a}_\varphi,\ \widetilde{a}_z)$	$\Delta r^+,\ \Delta x^+,\ \Delta z^+$	$Re_{\tau,i}$	$Re_{\tau,o}$
0.50	0.74, 0.33, 0.23	0.34, 8.8, 2.8	403	201
0.71	0.54, 0.18, 0.90	0.28, 7.2, 4.0	338	240
0.80	0.33, 0.20, 1.14	0.26, 7.9, 4.4	318	255
0.90	0.37, 0.23, 0.52	0.25, 7.9, 4.2	301	271
0.95	0.35, 0.22, 0.44	0.25, 8.2, 4.1	297	282
0.98	0.20, 0.14, 0.36	0.24, 8.0, 4.1	294	288
0.99	0.30, 0.13, 0.33	0.24, 7.6, 4.0	291	288
1	0.42, 0.42, 0.38	0.25, 7.7, 4.1	291	291

TABLE 2.3: Truncation error and grid spacing at the highest $Re_S = 2 \times 10^4$ for the different radius ratios η. The amplitudes of the highest spectral modes $\widetilde{a}_r$, $\widetilde{a}_\varphi$ and $\widetilde{a}_z$ estimate the truncation error of the expansion in the corresponding direction. Δr^+, Δx^+ and Δz^+ denote the grid spacing in inner wall units $\delta_{\nu,i}$ at the inner cylinder with $\Delta x^+ = r_i^+ \Delta\varphi$. The friction Reynolds numbers $Re_{\tau,i}$ and $Re_{\tau,o}$ at the inner and outer wall differ by a factor η. For the RPCF results in the bottom line, the coordinates r and φ correspond to y and x. We listed the maximal amplitudes, grid spacing values and friction Reynolds numbers over all R_Ω values considered here. For corresponding domain size and spatial resolution see Table 2.2.

ections by M_r, M_φ and M_z, respectively, since the RPCF coordinates x and y correspond to φ and r.

resolution characteristics

The truncation error of the expansions can be assessed by the amplitudes of the highest modes $\widetilde{a}_r$, $\widetilde{a}_\varphi$ and $\widetilde{a}_z$ which are normalised by the globally strongest mode. Our resolution tests in Section 2.2 revealed that these amplitudes have to drop to $\sim 10^{-4}$ for the shear Reynolds numbers $Re_S \sim 10^4$ considered here in order to reach converged torque values and velocity profiles. All present simulations fulfil this criterion. It turned out that the resolution in the axial direction could be reduced for larger η while maintaining $\widetilde{a}_z \lesssim 10^{-4}$, see Table 2.3. This seems plausible since the angular velocity gradients near the inner cylinder are steeper for small η (Eckhardt, Grossmann & Lohse, 2007b) and thus require a higher resolution. Consequently, the viscous length scale at the inner cylinder $\delta_{\nu,i} = \nu/u_{\tau,i} = \sqrt{\eta/(Re_S\, Nu_\omega)}$ increases with η so that the axial grid spacing in units of $\delta_{\nu,i}$ remains at $\Delta z^+ \approx 4$ for the maximal Nu_ω value at $Re_S = 2 \times 10^4$. Nevertheless, we did not reduce the resolution in the radial direction for large η, and hence the wall-normal grid spacing at the inner cylinder (Δr^+) decreases. Because of the non-uniform distribution of Chebyshev grid points, the wall-normal grid spacing at the centre increases by a factor of 49 compared to the grid spacing at the inner cylinder (cf. Table 2.3). The maximal streamwise grid spacing remains at $\Delta x^+ \approx 8$. Overall, our spacings $(\Delta r^+, \Delta x^+, \Delta z^+)$ at the inner cylinder are comparable to the ones used in other DNS of turbulent TCF (Bilson & Bremhorst, 2007; Pirrò & Quadrio, 2008). We furthermore note that the grid spacing measured in outer wall units $\delta_{\nu,o} = \delta_{\nu,i}/\eta$ is η-times smaller. Moreover,

our simulations satisfy the two additional convergence criteria described in Section 2.2: Agreement of the torques computed at the inner and outer cylinder within the statistical uncertainty and agreement of the energy dissipation estimated from the torque and from the volume-averaged energy dissipation rate to within 0.1%.

friction Reynolds numbers

Similar to the difference between inner and outer wall units, the friction Reynolds numbers at the inner wall $Re_{\tau,i} = u_{\tau,i}d/(2\nu) = \sqrt{\eta^{-1}Re_S\,Nu_\omega}/2$ and at the outer wall $Re_{\tau,o} = \eta Re_{\tau,i}$ differ, see Table 2.3. The simulations for $\eta = 0.5$ maximally reach $Re_{\tau,i} = 403$ and $Re_{\tau,o} = 201$, while in our RPCF simulations the maximal friction Reynolds number is $Re_\tau = 291$ at both walls.

2.6 COMPARISON TO OTHER STUDIES‡

So far, we identified three convergence criteria for a simulation to become resolution-independent and the minimal domain size required to receive accurate results for the torque and mean profiles. As a consistency check, we now test how simulations that meet these requirements compare to other torque studies. The comparison is based on torques for radius ratios $\eta = 0.5$ and $\eta = 0.71$ and analyses their variation with the shear (Re_S) and with the rotation ratio μ.

torques versus shear

First, we compare our computed torques for $\eta = 0.71$ and the outer cylinder at rest (Brauckmann & Eckhardt, 2013a) to experimental torque studies with $\eta \approx 0.7$ (Wendt, 1933; Lewis & Swinney, 1999; Racina & Kind, 2006) and to numerical simulations by Ostilla *et al.* (2013). Figure 2.8(a) shows the torque Nu_ω in dependence on the shear Reynolds number Re_S. All data collapse when plotted on logarithmic scales. In order to better resolve deviations between the torque studies, we show in Figure 2.8(b) the relative difference of Nu_ω to the fit proposed by Lewis & Swinney (1999) in their equation (3). For $Re_S > 3 \times 10^3$ most experimental and numerical torques agree to within 5% with the fit and the agreement is even better for the measurement by Lewis & Swinney (1999) who controlled their apparatus to always contain eight Taylor vortices. In contrast, the torques by Wendt (1933) and Racina & Kind (2006) may additionally be subject to variations due to a switching between different Taylor vortex states. Moreover, Lewis & Swinney (1999) only measured the torque acting on the central part of the inner cylinder to reduce effects from the end caps, whereas Wendt (1933) and Racina & Kind (2006) measured over the full cylinder height. End-wall effects in the latter studies are thus likely to contribute to the larger variations in Figure 2.8(b). Since the numerical scheme used

‡ The results of this section have been published in
H. J. Brauckmann & B. Eckhardt (2013a). Direct numerical simulations of local and global torque in Taylor–Couette flow up to $Re = 30\,000$. *J. Fluid Mech.* 718: 398–427
S. Merbold, H. J. Brauckmann & C. Egbers (2013). Torque measurements and numerical determination in differentially rotating wide gap Taylor–Couette flow. *Phys. Rev. E* 87: 023014.

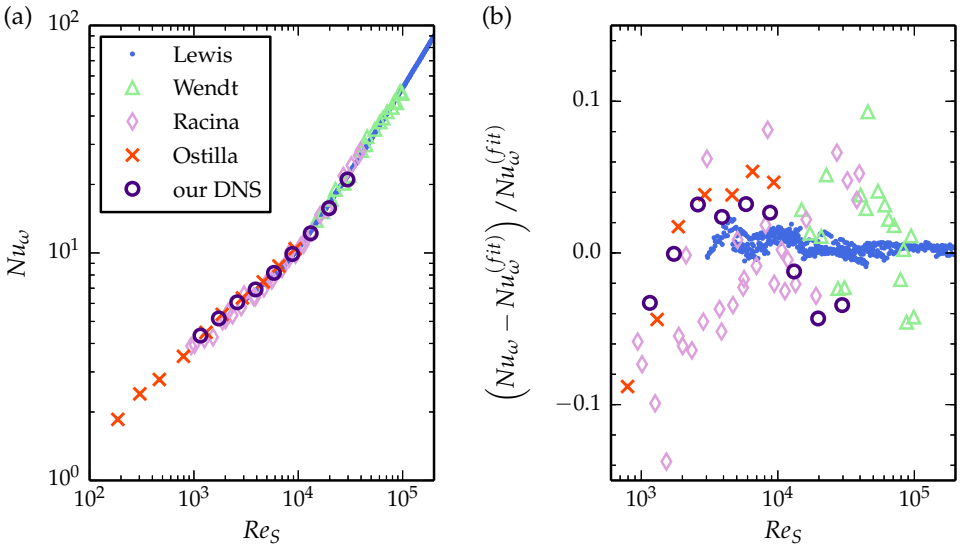

FIGURE 2.8: Comparison of torques as a function of Re_S for a stationary outer cylinder showing experimental results for $\eta = 0.724$ (Lewis & Swinney, 1999), for $\eta = 0.680$ (Wendt, 1933) and for $\eta = 0.76$ (Racina & Kind, 2006). In addition to the torques from our DNS with $\eta = 0.71$, we also show simulation results for $\eta = 0.714$ (Ostilla *et al.*, 2013). (a) In the double-logarithmic representation, some data by Wendt (1933) and Lewis & Swinney (1999) are hidden behind other symbols. (b) Small differences become apparent when plotting the relative deviation to the fit poposed by Lewis & Swinney (1999), i.e. their equation (3) transformed to a function $Nu_\omega(Re_S)$.

here can only represent periodic boundary conditions in axial direction, we are not able to analyse these effects.

In our simulations, an axial wavelength of 2 was selected for one vortex pair. In contrast, the measurement by Lewis & Swinney (1999) was carried out for an axial wavelength of 2.86. In light of the variation of the torque with the size of Taylor vortices (Brauckmann & Eckhardt, 2013a), deviations of $\sim 5\%$ of our torques to the fit by Lewis & Swinney (1999) can be expected. For small Reynolds numbers the torques fall below the fit. However, the latter has only been determined for $Re_S > 3 \times 10^3$ and does not necessarily apply to lower Reynolds numbers. The two numerical studies agree even better with each other than the experimental ones. This again proves that for stationary outer cylinder simulations with different aspect ratios but the same axial wavelength of Taylor vortices result in the same torque (see also Section 2.3). Ostilla *et al.* (2013) observed three vortex pairs in a domain of height $L_z = 2\pi$, resulting in an axial wavelength close to 2 as simulated here for $L_z = 2$. Furthermore, they simulated domains that completely wind around the cylinder. Our simulations impose a higher rotational symmetry of $n_{\mathrm{sym}} = 6$ or 9 for the highest shear Reynolds numbers. Therefore, the good agreement between the two numerical studies for $Re_S \approx 9 \times 10^3$ suggests that our azimuthal restriction to one sixth of the domain does not bias the torque computation. In conclusion, our simulations are consistent with previous experiments

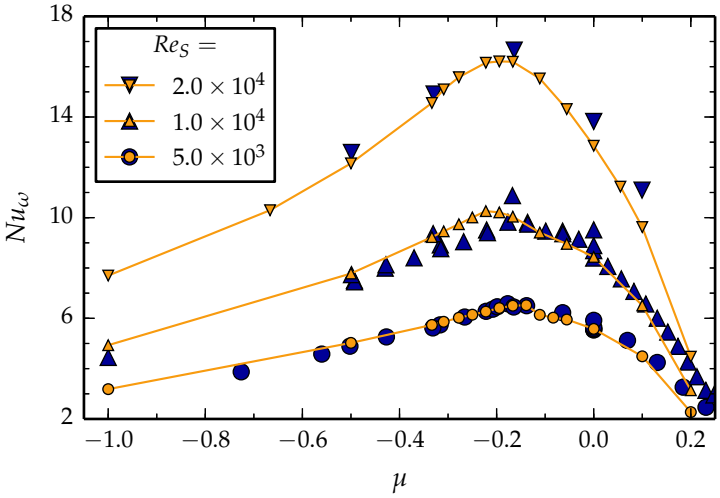

FIGURE 2.9: Comparison of the rotation dependence of torques for $\eta = 0.5$ and three different shear Reynolds numbers. The torques from the Cottbus experiment (▼ ▲ ●) with a height of $L_z = 20$ were measured using two oils of different viscosity (Merbold, Brauckmann & Egbers, 2013). Our DNS results (▼ ▲ ●) are obtained in a periodic domain of height $L_z = 2$, which for $Re_S \geq 10^4$ comprises only one third of the cylinder circumference, i.e. $n_{\text{sym}} = 3$.

to within 5% and even better conform with computations by Ostilla *et al.* (2013). Moreover, we note that a comparison of dimensionless torques G instead of $Nu_\omega = G/G_{\text{lam}}$ leads to a systematic deviation between datasets with slightly different radius ratios and is therefore not shown here. The difference is caused by the η-dependent prefactor in the laminar torque $G_{\text{lam}} = 2\eta/[(1-\eta)(1-\eta^2)]Re_i$. This observation shows the benefit of the Nusselt number Nu_ω also for comparisons between different TC set-ups.

torque versus rotation ratio

Next, we compare the rotation dependence of the torque from our DNS to various experimental studies. Figure 2.9 shows a comparison to the Cottbus experiment with the wide-gap radius ratio $\eta = 0.5$ (Merbold, Brauckmann & Egbers, 2013). In the experimental set-up, the cylinders have a height of $L_z = 20$ and the inner cylinder is subdivided into three parts so that only the torque acting on the central part is measured to reduce effects from the end caps. In contrast, our simulation results are obtained in a periodic domain of height $L_z = 2$ that is reduced to one third of the full azimuthal length for $Re_S = 10^4$ and 2×10^4 . Despite these restrictions, the numerical and experimental torques in Figure 2.9 are in good agreement. This shows again that the small numerical domain already carries the essential turbulent features to reproduce the torque of a much larger experiment. However, small deviations occur, especially at $Re_S = 10^4$ for counter-rotating cylinders with $\mu < -0.2$. Such deviations can be expected because of differences in the wavelength of Taylor vortices for these parameter values. While the simulation fixes the axial wavelength to $\lambda_z = 2$, vortices with a wavelength of $\lambda_z = 2.22$ are found in the experiment for $\mu < -0.18$. However, for $\mu > -0.18$ the experimental wavelength becomes $\lambda_z = 2$ as in the simulation. In both experiment

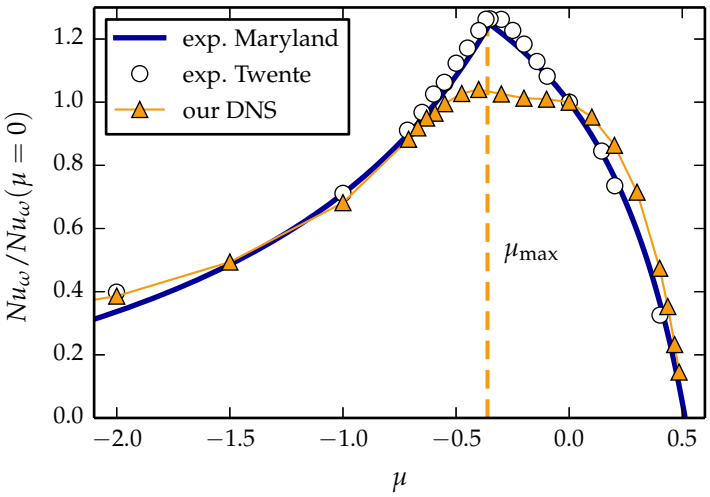

FIGURE 2.10: Comparison of the rotation dependence of torques showing results from the Maryland experiment with $\eta = 0.724$ (Paoletti & Lathrop, 2011), the Twente experiment with $\eta = 0.716$ (van Gils *et al.*, 2012) and our DNS ($\eta = 0.71$, $Re_S = 2 \times 10^4$). The experimental results are based on measurements in the range $3 \times 10^5 \lesssim Re_S \lesssim 3 \times 10^6$. To compensate for the increase of torques with Re_S, the results are divided by $Nu_\omega(\mu = 0)$. The solid line shows the fit by Paoletti & Lathrop (2011) to their data. The maximum location $\mu_{\max}$ in the DNS (dashed line) compares well to the experimental maxima at much higher Re_S.

and DNS, a maximum in the torque occurs at $\mu_{\max} \approx -0.2$, which will be further analysed in Chapter 3. Moreover, the experiment shows that the position of the maximum $\mu_{\max}$ does not change for higher Reynolds numbers up to $Re_S = 5 \times 10^5$ (Merbold, Brauckmann & Egbers, 2013). Consequently, the Reynolds number $Re_S = 2 \times 10^4$ reached in our DNS already suffices to capture the rotation dependence observed at much higher Re_S.

For the radius ratio $\eta \approx 0.7$, one can draw a similar conclusion from the comparison of DNS torques at $Re_S = 2 \times 10^4$ to experimental measurements from Maryland (Paoletti & Lathrop, 2011) and Twente (van Gils *et al.*, 2012) shown in Figure 2.10. As the experimental results are based on measurements with Re_S in the range between 3×10^5 and 3×10^6, a direct comparison of the absolute torque values makes little sense. Instead, we make use of the observation by Dubrulle *et al.* (2005), which is supported by experimental evidence (Paoletti & Lathrop, 2011; van Gils *et al.*, 2011, 2012; Paoletti *et al.*, 2012), that the torque variation can be represented by a factorisation into a scaling with Re_S and an amplitude that only depends on the rotation ratio μ. Thus, dividing Nu_ω by the corresponding value at $\mu = 0$ and an identical Re_S compensates for the Reynolds-number scaling and enables a torque comparison between studies at different Re_S. As shown in Figure 2.10, our simulations qualitatively reproduce the rotation dependence of the experiments, and the tails compare well even quantitatively. However, the maximum in the computed torques is not as pronounced as in the experiments. This is likely due to the much smaller Reynolds number ($Re_S = 2 \times 10^4$) in the simulation. In Brauckmann

& Eckhardt (2013a), we showed that the torque maximum only emerges when Re_S increases to 2×10^4 and that the exponent α of the torque scaling $G \propto Re_S^\alpha$ is largest for $\mu \approx -0.4$, i.e. near the maximum. Therefore, we expect that the amplitude of the maximum continues to grow for even higher Re_S. Nevertheless, the location of the maximum $\mu_{\max} = -0.36$ in the DNS torques already compares well to the experimental one $\mu_{\max} = -0.33$ at much higher Re_S (Paoletti & Lathrop, 2011; van Gils *et al.*, 2012).

In summary, our DNS of turbulent TCF fulfil three convergence criteria, and the torques from our simulations in a small domain are in good agreement with various experimental measurements. Differences in the Taylor vortex height and therefore our restriction to $L_z = 2$ can lead to small quantitative but not qualitative differences in the torque. Moreover, it is important to note that our numerical torques at $Re_S = 2 \times 10^4$ already show the same ($\eta = 0.5$) or a similar ($\eta = 0.7$) rotation dependence as experimental measurements at much higher Re_S. In the following, we therefore use the Reynolds number $Re_S = 2 \times 10^4$ as a test case to study the effect of rotation on turbulent TCF.

3

TURBULENT BURSTS AND TORQUE MAXIMA*

In this chapter, we study oscillations and large-scale vortices in the turbulence, as well as their influence on the torque. The turbulent regime of TCF is reached either after a sequence of instabilities or via a subcritical transition scenario (Andereck, Liu & Swinney, 1986; Koschmieder, 1993). In the first case, streamwise Taylor vortices typically develop that fill the entire cylinder gap and persist up to the turbulent regime (Koschmieder, 1979; Barcilon *et al.*, 1979; Huisman *et al.*, 2014). In the latter case, the turbulence is not always space-filling but can form turbulent spots or turbulent spirals for counter-rotating cylinders (Coles, 1965; Van Atta, 1966; Meseguer *et al.*, 2009b; Dong & Zheng, 2011). In addition to such azimuthal and axial modulations, Coughlin & Marcus (1996) described a flow state that is inhomogeneous in the radial direction and shows turbulent bursts. These intermittent turbulent bursts were also observed in experiments (Colovas & Andereck, 1997), and their presence was confirmed at much higher Reynolds numbers of $\sim 10^6$ in the Twente experiment (van Gils *et al.*, 2012). Furthermore, in the latter study, the onset of the bursting has been associated with the maximum that occurs in the torque for counter-rotating cylinders (van Gils *et al.*, 2011; Paoletti & Lathrop, 2011; Brauckmann & Eckhardt, 2013a; Merbold, Brauckmann & Egbers, 2013), see also Figure 2.9 and Figure 2.10.

In the following, we study the phenomenon of turbulent bursts in numerical simulations of TCF for various radius ratios and mean rotation states. We identify the critical value of the rotation ratio μ for the onset of turbulent bursting and determine the location of the torque maxima. Furthermore, in order to predict the bursting onset, we derive a physical model that is based on stability properties of the turbulent flow. Finally, we compare the model prediction to our numerical results for different radius ratios and describe the connection between model, bursting and torque maxima.

3.1 BOUNDARY-LAYER INTERMITTENCY

We analyse the phenomenon of the radial inhomogeneity in simulations of wide-gap TC systems where it turned out to be more pronounced. The analysis includes four values of the radius ratios η ranging from 0.5 to 0.9. In order to study the influence of the system rotation, the simulations are

* The main results of this chapter have been published in
H. J. Brauckmann & B. Eckhardt (2013b). Intermittent boundary layers and torque maxima in Taylor–Couette flow. *Phys. Rev. E* 87: 033004
H. J. Brauckmann & B. Eckhardt (2015). Intermittent boundary layers in Taylor–Couette flow. *EUROMECH Newsletter* 46: 8–14.

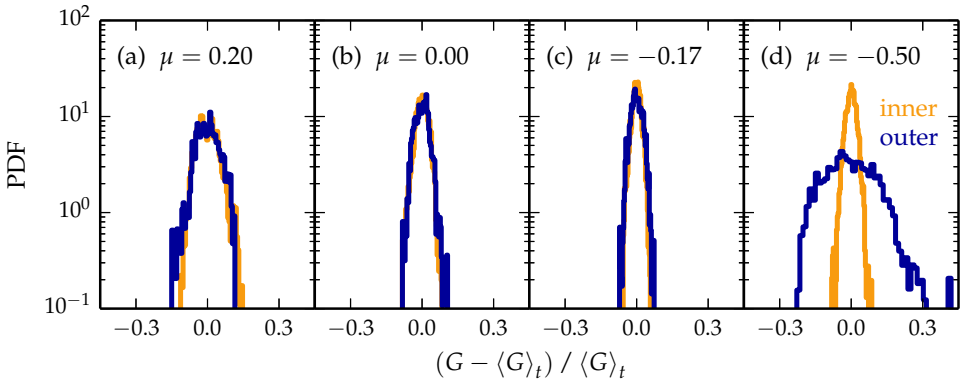

FIGURE 3.1: Distribution of temporal torque fluctuations calculated at the outer cylinder (—) and inner cylinder (—) for $\eta = 0.5$, $Re_S = 2 \times 10^4$ and various rotation ratios μ. All torques are normalised by the corresponding long-time mean value $\langle G \rangle_t$. Except for $\mu = -0.50$, the PDFs of the outer and inner torque lie almost on top of each other.

performed at a constant shear between the cylinders, defined by the shear Reynolds number Re_S (Dubrulle *et al.*, 2005), and for various values of the rotation ratio μ that characterises the mean rotation state. The shear Reynolds number is set to $Re_S = 2 \times 10^4$, since we intend to investigate the turbulent behaviour at high shear rates. This value is above $Re_S = 1.5 \times 10^4$ at which Lathrop, Fineberg & Swinney (1992a,b) found the transition to a fully turbulent regime for $\eta = 0.725$ and $\mu = 0$, where the torque conforms to a Prandtl–von Kármán skin friction law. In addition, the torque maximisation as a function of μ exemplifies that the high-shear behaviour only emerges for $Re_S > 10^4$: For $\eta = 0.71$, the torque-maximising μ value changes when Re_S increases from 4×10^3 to 2×10^4 (Brauckmann & Eckhardt, 2013a) and then compares well to the location of the torque maximum found in experiments at much higher $Re_S \sim 10^5$ to 10^6 (Paoletti & Lathrop, 2011; van Gils *et al.*, 2011), as shown in Figure 2.10. This suggests that the maximum location reaches an asymptotic value for high Re_S.

torque fluctuations

In this section, we analyse the turbulent near-wall fluctuations that vary with the rotation ratio μ, as illustrated for $\eta = 0.5$ by probability distribution functions (PDFs) of the instantaneous torque in Figure 3.1: For co-rotating cylinders, i.e. $\mu \geq 0$ in (a) and (b), as well as for slightly counter-rotating cylinders, i.e. $\mu = -0.17$ in (c), the torques at the inner and outer cylinder agree in their fluctuations. This agreement disappears for strongly counter-rotating cylinders ($\mu = -0.50$) as shown by the broader distribution of the outer torque in (d), indicating large fluctuations in the turbulence near the outer cylinder. At the same time, the torque fluctuations at the inner cylinder vary only little with μ.

turbulent bursts

Figure 3.2 reveals the turbulent dynamics that causes the difference between inner and outer fluctuations for strong counter-rotation: The torque time-series for $\mu = -0.5$ in (a) shows small and irregular fluctuations at the inner cylinder. In contrast, the torque at the outer cylinder exhibits large and relatively slow variations with periods of almost 100

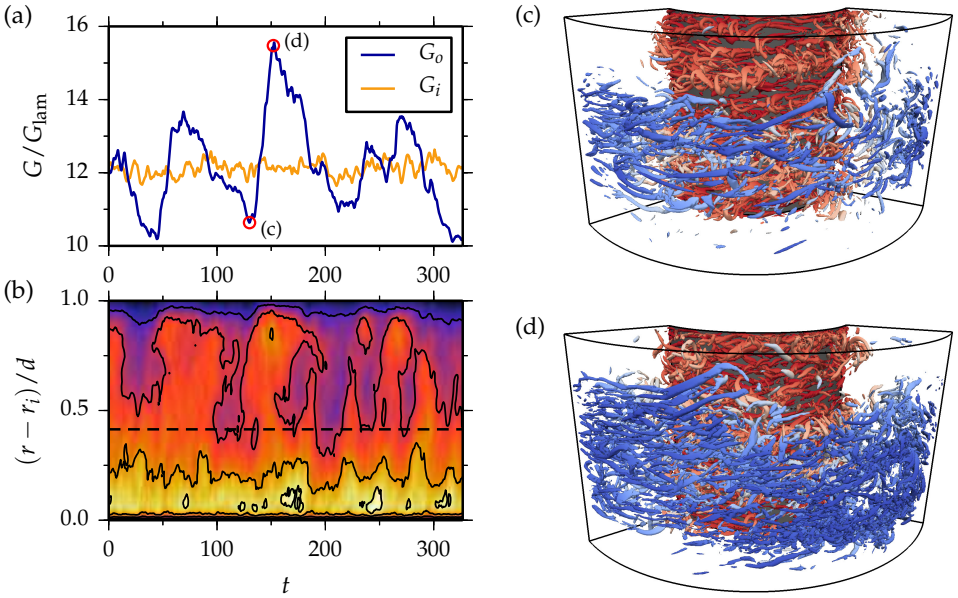

FIGURE 3.2: Turbulent bursts for $\eta = 0.5$, $Re_S = 2 \times 10^4$ and exact counter-rotation ($\mu = -0.5$). (a) Time-series of the torque calculated at the outer cylinder (G_o) and inner cylinder (G_i), compensated by the laminar value G_{lam}. (b) Spatio-temporal plot of the cross-flow energy $E_{\mathrm{cf}}(r,t)$ averaged over concentric cylindrical surfaces with white (black) showing maximum (minimum) energy. The laminar neutral surface is marked by the horizontal dashed line. The turbulent flow for the low- and high-torque state (marked by circles in (a)) is visualised in (c) and (d), respectively, by the iso-surface of $\lambda_2 = -2$, a vortex identification method (Jeong & Hussain, 1995). The colour coding represents the radial distance.

advective time units. While the variations are also superimposed by small fluctuations, they qualitatively still differ from the fluctuations at the inner cylinder. These large variations correspond to an intermittent turbulent activity in the fluid layer near the outer cylinder, as demonstrated by the cross-flow energy in Figure 3.2(b). The cross-flow energy,

$$E_{\mathrm{cf}}(r,t) = \left\langle u_r^2 + u_z^2 \right\rangle_A , \tag{3.1}$$

measures the energy contained in the radial and axial velocity components in a cylindrical fluid layer at radial distance r and at time t. Small and large E_{cf} values indicate a flow close to laminar and a turbulent flow, respectively. The spatio-temporal plot reveals a permanently strong turbulence near the inner cylinder, whereas the turbulence in the outer region varies in strength over time. Moreover, the strongly turbulent phases occur synchronised with the increase in the outer torque and will be denoted as *turbulent bursts*. The instantaneous flow at the minimum and maximum of one bursting cycle is visualised in Figure 3.2(c) and (d), respectively, using the λ_2-criterion† for the identification of small-scale vortices (Jeong & Hussain, 1995). In both cases, the inner cylinder is completely covered by

† λ_2 denotes the second largest eigenvalue of the tensor $\boldsymbol{S}^2 + \boldsymbol{\Omega}^2$, where $\boldsymbol{S}$ and $\boldsymbol{\Omega}$ are the symmetric and anti-symmetric parts of the velocity gradient tensor $\boldsymbol{\nabla u}$.

small-scale vortices. In contrast, the number and spatial expansion of vortices near the outer cylinder increases for the burst maximum in (d). The visualisations furthermore show that small turbulent vortices occur predominantly close to the cylinder walls, i.e. in the BLs, and less frequently in the centre of the flow.

radial stability difference

The radial partitioning into a permanently turbulent inner region and an intermittent outer region correlates with the stability of the laminar flow: While the inner region for radii $r \in (r_i, r_n)$ is linearly unstable, the flow is Rayleigh-stable in the outer range $r \in (r_n, r_o)$, with r_n denoting the radius where, in the inertial reference frame, the velocity profile passes through zero (Chandrasekhar, 1961). For the exemplary case $\eta = 0.5$ and $\mu = -0.5$, the neutral radius $r_n = 1.41$ is marked by a dashed line in Figure 3.2(b). The presence of the bursts reveals that the flow overcomes linear stability, but the laminar neutral radius r_n still coincides with the radial location of the transition from permanent to intermittent turbulence. Consequently, the stabilisation of the outer region is still reflected in the intermittent dynamics.

At a lower Reynolds number $Re_S \sim 2.3 \times 10^3$, Coughlin & Marcus (1996) found that the turbulent bursts develop as an instability of spatially ordered *interpenetrating spiral* flow that forms in the Rayleigh-unstable inner region. Here at $Re_S = 2 \times 10^4$, the inner region is turbulent without obviously ordered structures, such as spiral vortices, and the outer one still exhibits the bursting. Moreover, the observation extends to even larger Reynolds numbers $Re_S \sim 10^6$ in the experiment by van Gils *et al.* (2012), where the existence of turbulent bursts in the outer layer was inferred from a bimodal distribution of the angular velocity. Consequently, the connection to spirals is not required for the bursts to occur.

onset of bursting behaviour

The torque PDFs in Figure 3.1 already showed that turbulent bursts only occur for strongly counter-rotating cylinders, i.e. large negative values of μ. In the following, we identify the critical rotation ratio $\mu_c(\eta)$ for the onset of the bursting behaviour by utilising the observation that turbulent bursts are connected to increased torque fluctuations at the outer cylinder. Therefore, we measure the fluctuation amplitude by the standard deviation σ_G of the torque relative to the mean value G and define the critical value $\mu_c(\eta)$ by the requirement that σ_G/G calculated at the outer cylinder exceeds a reference value. The choice of the ratio σ_G/G as an indicator for the transition is supported by the observation that it varies only little with μ at the inner cylinder, see Figure 3.3. This procedure enabled us to identify the bursting onset as a function of μ for $\eta = 0.5$ and 0.71 (Brauckmann & Eckhardt, 2013b). We here extend the analysis to $\eta = 0.8$ and 0.9. In the previous study, the relative fluctuation amplitude σ_G/G was assumed to be constant (i.e. independent of μ) at the inner cylinder. Therefore, the value of σ_G/G at $\mu = 0$ served as the reference value that the outer fluctuations exceed. However, the data for $\eta = 0.8$ and 0.9 do not show constant inner fluctuations (Figure 3.3(c,d)). Nevertheless, the inner value of σ_G/G approaches an almost constant base level for $\mu \ll 0$, and so we here take

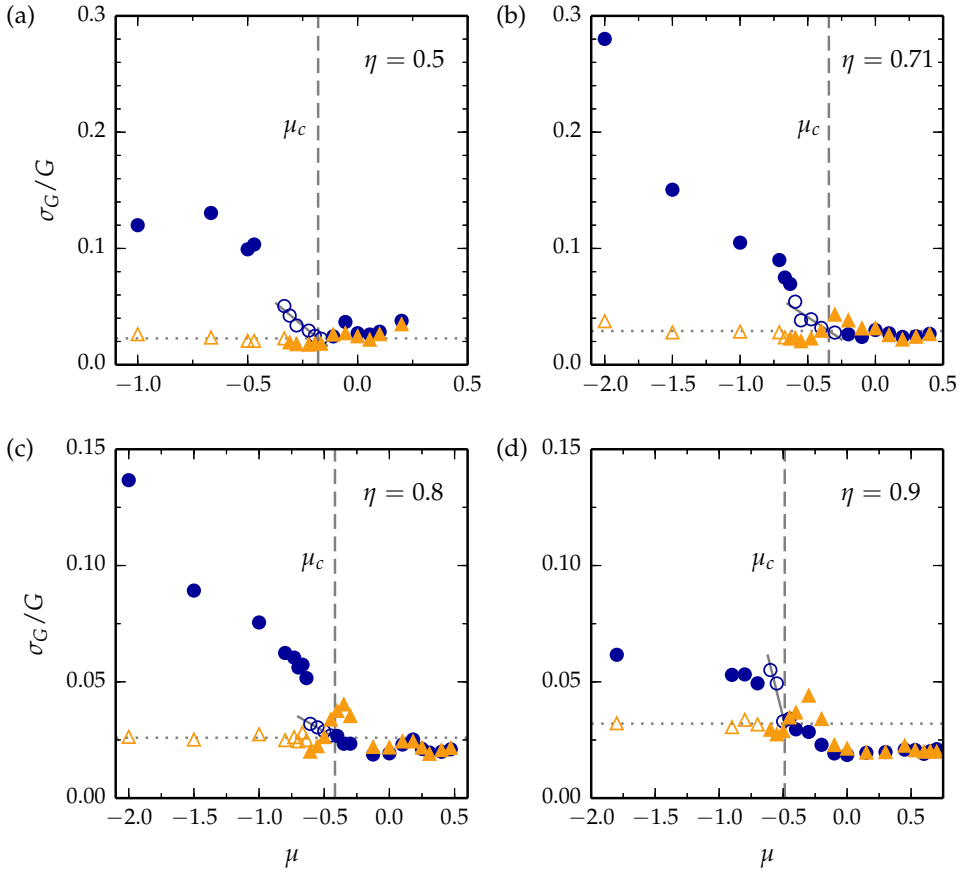

FIGURE 3.3: Standard deviation σ_G (divided by the mean G) of temporal torque fluctuations calculated at the outer cylinder (● ○) and inner cylinder (▲ △) for a constant shear $Re_S = 2 \times 10^4$ and varying rotation ratio μ. The dotted line marks the base level for the fluctuations at the inner cylinder for strong counter-rotation (average of open triangles). The solid line is a linear fit to 6 points in (a), to 5 points in (b), to 4 points in (c) and to 3 points in (d) which are marked as open circles. The vertical dashed line indicates the intersection point μ_c that defines the onset of enhanced outer fluctuations.

the average inner fluctuations (σ_G/G) for strong counter-rotation as the reference value. Figure 3.3 shows that the outer fluctuation amplitude exceeds the inner base level when μ decreases below a critical value $\mu_c(\eta)$. Similar to the procedure used in Brauckmann & Eckhardt (2013b), we determine the critical values

$$\begin{aligned} \mu_c(0.5) &= -0.180 \pm 0.014, & \mu_c(0.71) &= -0.344 \pm 0.050, \\ \mu_c(0.8) &= -0.418 \pm 0.025, & \mu_c(0.9) &= -0.488 \pm 0.025 \end{aligned} \tag{3.2}$$

critical rotation ratios

from the intersection of a linear fit to the outer fluctuations with the base level. The uncertainties are estimated as half of the difference in μ between the two data points surrounding the critical value. For $\eta = 0.5$ and 0.71, the re-evaluated onsets μ_c conform with the old values in Brauckmann & Eckhardt (2013b) within the uncertainties. It is noteworthy that the bursting onset μ_c depends on η; this feature will be discussed in detail in Section 3.3. However, the critical value seems not to change for

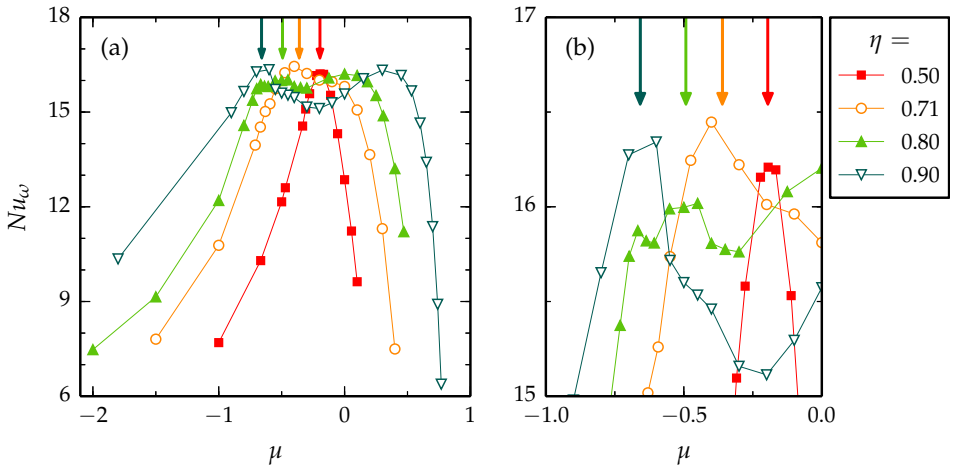

FIGURE 3.4: Variation of the torque ($Nu_\omega = G/G_{\text{lam}}$) with the rotation ratio μ for $Re_S = 2 \times 10^4$ and various radius ratios. For each η value, the location $\mu_{\max}$ of the torque maximum for counter-rotating cylinders was calculated from a quadratic fit to at least five data points and is marked by an arrow. Sub-figure (b) details the maxima in (a).

even higher Reynolds numbers, since the value for $\eta = 0.71$ conforms with $\mu_c(0.716) \approx -0.368$ determined for the onset of intermittent bursts in the experiment at $Re_S \sim 10^6$ (van Gils *et al.*, 2012). Note that the simulations furthermore show that inner and outer torque fluctuations agree in amplitude for a stationary outer cylinder and for co-rotation ($\mu \geq 0$). This is in clear contrast to the fluctuation enhancement due to the bursting for strong counter-rotation.

3.2 TORQUE MAXIMA

In turbulent TCF, another phenomenon that arises with changing mean system rotation has been studied recently: For a constant shear between the cylinders, the torque as a function of the rotation ratio μ shows a maximum, as first identified in two independent experiments with radius ratios $\eta = 0.7245$ (Paoletti & Lathrop, 2011) and $\eta = 0.716$ (van Gils *et al.*, 2011). For Reynolds numbers $Re_S \sim 10^5$ to 10^6, they report a torque maximisation at $\mu_{\max} = -0.333$ and $\mu_{\max} = -0.33 \pm 0.04$, respectively, i.e. for counter-rotating cylinders. Numerical simulations for $\eta = 0.71$ revealed that the location $\mu_{\max}$ of the maximum shifts with increasing shear (Brauckmann & Eckhardt, 2013a; Ostilla *et al.*, 2013): For $Re_S \leq 4 \times 10^3$, the maximum occurs for a stationary outer cylinder ($\mu = 0$) and subsequently shifts to negative μ values with increasing shear. Then, the maximum position at $Re_S = 2 \times 10^4$ conforms with the experimental observation at much higher Re_S, suggesting the beginning of an asymptotic regime for $Re_S \gtrsim 2 \times 10^4$, see also Section 2.6.

Figure 3.4 shows torques from our DNS at $Re_S = 2 \times 10^4$ for four radius ratios that also exhibit a maximum for counter-rotation. In addition, a second maximum for co-rotation occurs for $\eta = 0.8$ and 0.9 that is not

related to the bursting phenomenon discussed in this chapter. Therefore, the second peak will only be analysed in Chapter 4 and Chapter 5. We determine the locations $\mu_{\max}(\eta)$ of the first maximum from a quadratic fit $Nu_\omega = c_2\mu^2 + c_1\mu + c_0$ to at least five data points and find

$$\begin{aligned} \mu_{\max}(0.5) &= -0.195 \pm 0.019, & \mu_{\max}(0.71) &= -0.361 \pm 0.054, \\ \mu_{\max}(0.8) &= -0.492 \pm 0.058, & \mu_{\max}(0.9) &= -0.658 \pm 0.041. \end{aligned} \tag{3.3}$$

torque maximum locations

The uncertainties in $\mu_{\max}$ follow from the relative confidence interval δG of torque values, which results from temporal fluctuations. Based on the quadratic fit, this uncertainty in the torques transforms into one of the maximum location,

$$\Delta\mu_{\max} = \sqrt{-\frac{\delta G}{c_2}\left(Nu_\omega\right)_{\max}}, \tag{3.4}$$

derived from the maximal Nusselt number $\left(Nu_\omega\right)_{\max}$ and the fit coefficient c_2. The maximum location for $\eta = 0.71$ conforms (within the usual uncertainties) with the aforementioned experimental observation $\mu_{\max}(0.72) = -0.33$ (Paoletti & Lathrop, 2011; van Gils *et al.*, 2012). Furthermore, experiments in a wide-gap TC system with $\eta = 0.5$ are in agreement with our torque calculations (cf. Figure 2.9) and confirm that the maximum remains located at $\mu_{\max} = -0.20 \pm 0.02$ up to shear Reynolds numbers of 5×10^5 (Merbold, Brauckmann & Egbers, 2013).

One important observation for $\eta = 0.5$, 0.71 and 0.8 is the coincidence of the torque-maximising rotation ratio $\mu_{\max}$ (3.3) with the onset of the bursting behaviour μ_c (3.2). This agreement was first observed in the experiment by van Gils *et al.* (2012) and will be further discussed and rationalised in Section 3.4. Our results for $\eta = 0.9$, however, do not show the coincidence between $\mu_{\max}$ and μ_c, which is plausible since the dynamical properties of counter-rotating TCF change for η close to 1, as we will explain in Chapter 4.

Wendt's torque maximum

An additional data point for the maximum location follows from the torque measurements by Wendt (1933). Re-analysing his torque data for $\eta = 0.680$ in the same way as in recent experiments reveals a maximum near

$$\mu_{\max}(0.680) = -0.295 \pm 0.113, \tag{3.5}$$

as shown in Appendix A. Its relatively high uncertainty is due to a broad maximum and only few rotation ratios investigated by Wendt. Nevertheless, this maximum location conforms with current $\mu_{\max}$ values identified in experiments and in our simulations.

3.3 ONSET OF THE RADIAL INHOMOGENEITY

The results in Section 3.1 and Section 3.2 raise two questions that we seek to answer by a physical model in the following. First, we ask for the physical mechanism that causes the bursting onset so that we are able

to derive a prediction for the critical rotation ratio μ_c from it. Second, we seek to understand the reason for the observed agreement between torque-maximising rotation ratio and the bursting onset.

A first answer to these questions was given by van Gils *et al.* (2012): Since the turbulent momentum transport is expected to increase when the flow becomes more unstable, they suggested that the torque is maximised for the locations in parameter space (Re_i, Re_o) that are equally distant from the Rayleigh stability lines $Re_i = Re_o/\eta$ and $Re_i = 0$. These locations correspond to a line in the (Re_i, Re_o)-space that exactly bisects the unstable regime. The condition for this *angle bisector* results in the rotation ratio

angle bisector

$$\mu_b(\eta) = \frac{-\eta}{\tan\left[\frac{\pi}{2} - \frac{1}{2}\arctan(\eta^{-1})\right]} \tag{3.6}$$

for the estimated location of the torque maximum. Moreover, van Gils *et al.* (2012) argued that for $\mu < \mu_b$ the torque is reduced due to the stabilising effect of the counter-rotating outer cylinder, and that the latter also causes the bursts observed for these rotation ratios. While for $\eta = 0.716$ the angle bisector $\mu_b = -0.368$ conforms with their measured torque maximum $\mu_{\max} = -0.33 \pm 0.04$, it clearly deviates from our DNS result $\mu_{\max} = -0.20 \pm 0.02$ for $\eta = 0.5$, which was confirmed in the Cottbus experiment (Merbold, Brauckmann & Egbers, 2013), since equation (3.6) gives $\mu_b(0.5) = -0.309$.

theoretical model

Here, we first explain the location μ_c of the bursting onset and its dependence on the radius ratio η, before we rationalise the coincidence between μ_c and the maximum $\mu_{\max}$ in a second step. To this end, we introduce a physical model that is based on stability properties of the turbulent flow in general, and on the strength of turbulent Taylor vortices in particular. One principal element of this model is the radial partitioning of the flow into a Rayleigh-unstable inner region and a stabilised outer region. Furthermore, for a sufficiently strong counter-rotation, the turbulence from the inner region is no longer strong enough to sustain turbulence across the stable outer region. The latter, however, cannot remain laminar for all times since the radial transport of momentum mediated by turbulence has to be independent of the radial position (Eckhardt, Grossmann & Lohse, 2007b). Therefore, turbulence will occur intermittently in the stabilised outer region when the actively driven inner region detaches from the outer cylinder, which marks the onset of the bursting behaviour.

Coughlin & Marcus (1996) already noted that the occurrence of bursts is related to the appearance of a neutral surface at the radius r_n, where the laminar velocity profile becomes zero, i.e. $\hat{\omega}_{\mathrm{lam}}(r_n) = 0$ in the inertial reference frame. Inviscid stability calculations using Rayleigh's argument (Rayleigh, 1917) predict the neutral surface at

$$r_n(\mu) = r_i \sqrt{\frac{1-\mu}{\eta^2 - \mu}} \tag{3.7}$$

for counter-rotating cylinders, i.e. for $\mu \leq 0$ (Chandrasekhar, 1961). It divides the flow into an unstable inner region ($r_i < r < r_n$) and a stable outer

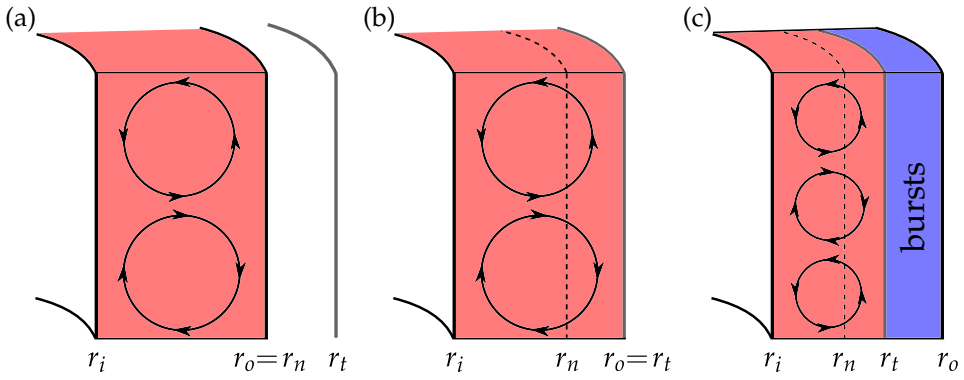

FIGURE 3.5: Illustration of the effective radial extension of Taylor vortices predicted by equation (3.8): (a) For $\mu > \mu_p$ the vortices are restricted by the outer cylinder (as here exemplified for $\mu = 0$), (b) they exactly fill the cylinder gap at $\mu = \mu_p$ and (c) they are only present in an inner region for $\mu < \mu_p$, leaving space for a stabilised outer region that is susceptible to turbulent bursts.

region ($r_n < r < r_o$). This simple calculation would predict a detachment of the active inner region and thus the occurrence of bursts for any $\mu < 0$ independent of η, which is inconsistent with the observed bursting onset for $\mu < \mu_c(\eta) < 0$, cf. equation (3.2). But experiments as well as viscous calculations show that flow structures from the inner region extend beyond r_n (Taylor, 1923; Donnelly & Fultz, 1960), which means that the neutral surface does not define a fixed boundary. Accordingly, we estimate this increase in the width of the inner region by the factor $a(\eta) \in [1.4, 1.6]$ that was deduced by Esser & Grossmann (1996) from their stability calculation. There, the width $a(\eta)(r_n - r_i)$ describes the increased size of Taylor vortices for counter-rotating cylinders. We take this estimate to the turbulent regime. Thus, the effective extension of flow structures from the inner region is

$$r_t(\mu) = r_i + a(\eta)\,(r_n - r_i), \tag{3.8}$$

with a factor

$$a(\eta) = (1-\eta)\left[\sqrt{\frac{(1+\eta)^3}{2(1+3\eta)}} - \eta\right]^{-1}. \tag{3.9}$$

Consequently, the condition $r_t(\mu_p) \equiv r_o$ determines the rotation ratio μ_p where the actively driven inner region detaches from the outer cylinder. Solving the condition for μ_p gives

$$\mu_p(\eta) = -\eta^2\,\frac{(a-1)^2\eta + a^2 - 1}{(2a-1)\eta + 1}, \tag{3.10}$$

prediction for bursting onset

that serves as prediction for the bursting onset for $\mu < \mu_p$, as Figure 3.5 illustrates: For $\mu > \mu_p$ in (a), the entire domain is unstable and thus driven to turbulence. Hypothetically, the vortices from the inner region would extend beyond r_o, but they are restricted by the outer cylinder in reality. At $\mu = \mu_p$ in (b), the turbulent Taylor vortices exactly fit into the cylinder gap. And finally, for $\mu < \mu_p$ in (c), the turbulence can no longer fill the

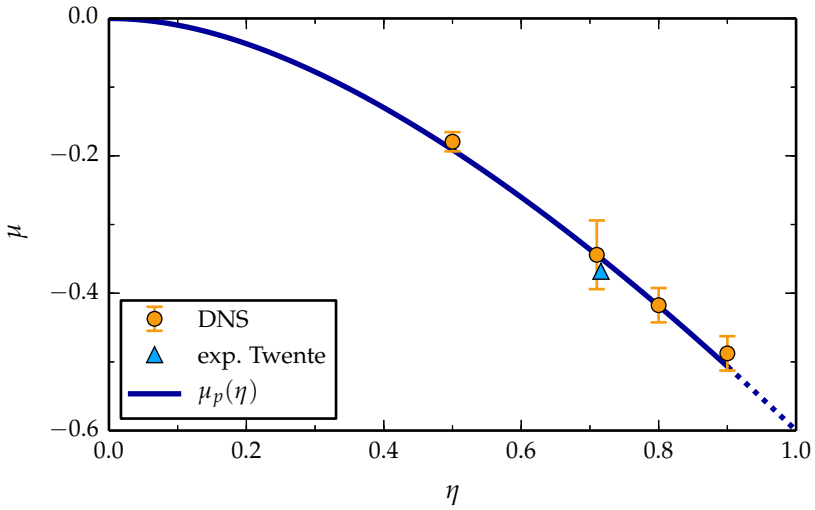

FIGURE 3.6: Onset of enhanced outer fluctuations: The critical rotation ratio $\mu_c(\eta)$ for the onset is shown as a function of the radius ratio η. Numerical values for $Re_S = 2 \times 10^4$ are extracted from Figure 3.3 and the value from the Twente experiment (van Gils *et al.*, 2012) was deduced from a bimodal distribution of the angular velocity. The line indicates the prediction $\mu_p(\eta)$ from equation (3.10). As the radial partitioning disappears for $\eta \to 1$, we indicate the resulting uncertainty in the prediction by continuing the curve with dashes for $\eta \gtrsim 0.9$.

entire gap, leaving space for a stabilised outer region that is susceptible to turbulent bursts. The sketch also illustrates that the increased size of the inner region as defined by the factor $a(\eta)$ necessitates a minimal counter-rotation for the neutral surface to lie between the cylinders.

Figure 3.6 shows that the prediction from (3.10) is in good agreement with the bursting onsets determined in our DNS for $Re_S = 2 \times 10^4$ (Figure 3.3). Moreover, $\mu_p(\eta)$ conforms with the critical rotation ratio for the occurrence of bursts, detected as a bimodal distribution of angular velocities in the experiments of van Gils *et al.* (2012) for $\eta = 0.716$. The bursts found by Coughlin & Marcus (1996) at the rotation ratio $\mu = -2.797$ are also in line with the prediction, since this value clearly lies in the intermittent regime below μ_p. For comparison, some numerical values of $\mu_p(\eta)$ are listed in Table 3.1 together with the empirically found bursting onsets μ_c.

3.4 ENHANCED LARGE-SCALE VORTICES

strengthening of Taylor vortices

We now turn to the second, still open question of why the location of the torque maximum coincides with the bursting onset. Previously, van Gils *et al.* (2012) argued that both coincide since the flow stabilisation caused by the counter-rotating outer cylinder reduces the radial momentum transport and thereby the torque. However, for the formation of a maximum at the bursting onset μ_c, the torque not only has to decrease for $\mu < \mu_c$, but also to increase for μ decreasing from zero to μ_c. We argue that the latter effect is caused by a strengthening of the turbulent Taylor vortices, which are the TCF analogue of the large-scale circulation found in Rayleigh–Bénard

η	μ_c	$\mu_{\max}$	μ_p	μ_b	μ_{LSC}	SOURCE
0.5	−0.180	−0.195	−0.191	−0.309	−0.223	DNS
0.680		−0.295	−0.321	−0.360		Wendt
0.71	−0.344	−0.361	−0.344	−0.367	−0.380	DNS
0.716	−0.368	−0.33	−0.349	−0.368		Twente
0.725		−0.333	−0.356	−0.370		Maryland
0.8	−0.418	−0.492	−0.419	−0.384	−0.442	DNS
0.9	−0.488	−0.658	−0.507	−0.401	−0.441	DNS

TABLE 3.1: The rotation ratio of the onset of intermittency μ_c and of the torque maximum $\mu_{\max}$ are compared with the prediction μ_p (3.10) and the angle bisector μ_b (3.6) by van Gils *et al.* (2012) for the radius ratios of the DNS and of the experiments from Twente (van Gils *et al.*, 2012), Maryland (Paoletti & Lathrop, 2011) and Wendt (1933). The rotation ratio μ_{LSC} specifies the position of the maximum in the mean-vortex contribution to the torque determined in Figure 3.7.

convection (Ahlers, Grossmann & Lohse, 2009). They can increase the torque since they effectively transport angular momentum in the radial direction. Our physical model sketched in Figure 3.5 supports such a strengthening of Taylor vortices near $\mu_p \approx \mu_c$: For $\mu > \mu_p$ in (a), the vortices are predicted to extend beyond the outer cylinder (i.e. $r_t > r_o$), which therefore inhibits the vortex motion. This restrictive outer boundary changes with μ decreasing towards μ_p in (b), since a layer close to the outer cylinder becomes stabilised and acts as a free-surface-like boundary condition. Less inhibited by the outer wall, the Taylor vortices can gain in strength, thereby transporting more momentum. Finally, for $\mu < \mu_p$ in (c), the bursting will destroy the vortices. Therefore, the momentum transport will decrease again.

To test this explanation for the torque maximisation, we extract the mean Taylor vortices from the turbulent flow and measure their contribution to the torque. To this end, we calculate the mean-vortex flow by averaging azimuthally and in time, $\overline{\boldsymbol{u}} = \langle \boldsymbol{u} \rangle_{\varphi,t}$, so that $\overline{\boldsymbol{u}}$ only represents the mean variations in the radial-axial plane. The remainder $\boldsymbol{u}'' = \boldsymbol{u} - \overline{\boldsymbol{u}}$ contains the turbulent fluctuations around the mean vortical motion, cf. Bilson & Bremhorst (2007). By substituting this velocity decomposition into the transverse current J^ω, equation (1.8), we obtain a partitioning of the total torque G into a contribution $\overline{G}$ that is caused by the mean vortical motion and a second contribution G'' that is due to turbulent fluctuations, i.e. $G = \overline{G} + G''$ with

$$\begin{aligned} \overline{G} &= \frac{Re_S^2}{r_2 - r_1} \int_{r_1}^{r_2} \left(\langle \overline{u}_r \overline{\mathcal{L}} \rangle - Re_S^{-1} r^2 \partial_r \langle \overline{\omega} \rangle \right) r \, \mathrm{d}r, \\ G'' &= \frac{Re_S^2}{r_2 - r_1} \int_{r_1}^{r_2} \langle u_r'' \mathcal{L}'' \rangle \, r \, \mathrm{d}r. \end{aligned} \tag{3.11}$$

contributions to the torque

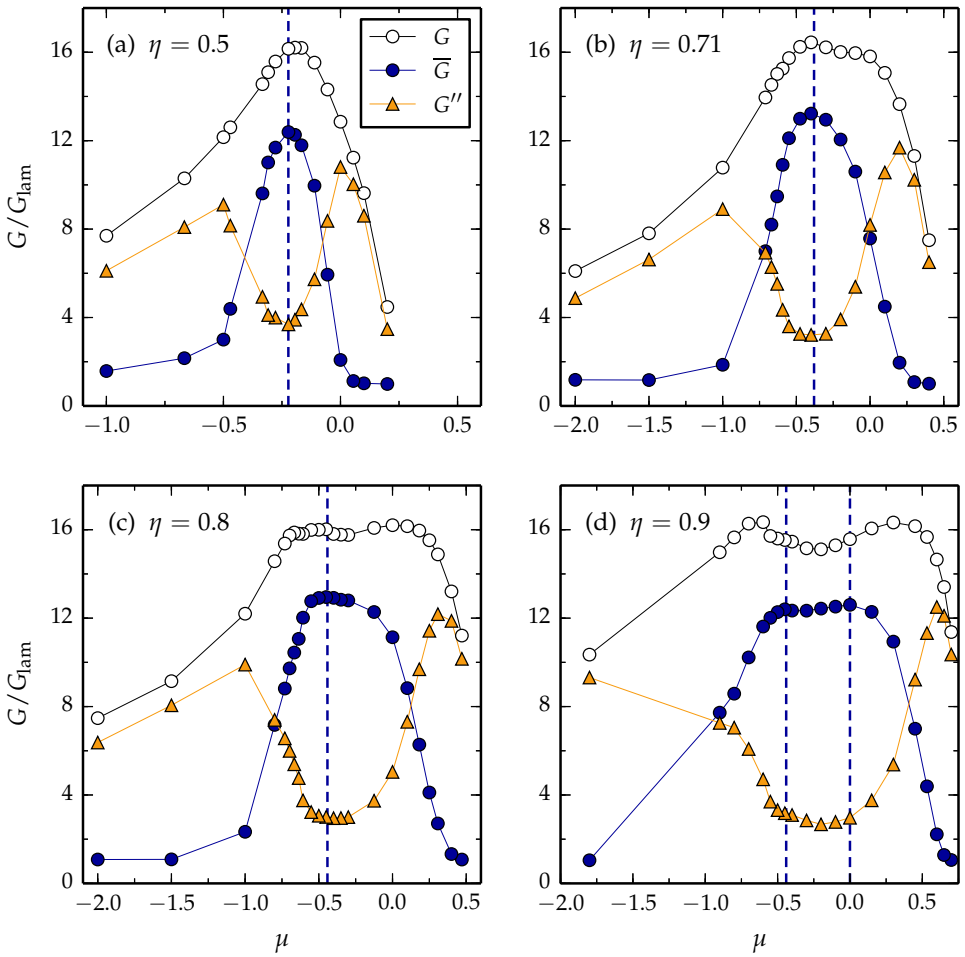

FIGURE 3.7: Comparison of the mean-vortex torque contribution $\overline{G}$ (●) and turbulent torque contribution G'' (▲) with the total torque G (○) for $Re_S = 2 \times 10^4$ and various radius ratios. The location μ_{LSC} of the maximum in the mean-vortex torque is marked by a dashed line, with two maxima occurring for $\eta = 0.9$ in (d).

Since the velocity decomposition implies $\langle \boldsymbol{u}'' \rangle = \mathbf{0}$ by definition, the mixed terms $\langle \overline{u}_r \mathcal{L}'' \rangle$ and $\langle u_r'' \overline{\mathcal{L}} \rangle$ as well as $\langle \omega'' \rangle$, which result from the velocity decomposition in the transverse current (1.8), vanish. To capture the correct amplitude of the turbulent Taylor vortices, we fix their axial position during the temporal average of $\overline{\boldsymbol{u}}$ and in (3.11) by correcting a potential axial drift‡. Such a drift would lead to a cancellation of the large-scale motion over time, even though it might be strong. Note that while the total transport G is constant over r, the individual terms in (3.11) vary with the radius. This motivates the additional radial average in (3.11) in order to quantify the overall strength of the torque contributions. We here average over the entire radial range with $r_1 = r_i$ and $r_2 = r_o$.

‡ To determine the axial drift, for each flow snapshot we calculate an axial profile of the radial velocity $\widetilde{u}_r(z)$, which was averaged azimuthally and radially in the central range $(r - r_i)/d \in [0.3, 0.7]$. We then determine the axial shift z_0 that minimises the distance of the function $\sqrt{2}\langle \widetilde{u}_r \rangle_{\mathrm{rms}} \cos[2\pi(z - z_0)/L_z]$ to the axial profile $\widetilde{u}_r(z)$. Subsequently, each flow field is axially shifted by its instantaneous position z_0.

Figure 3.7 compares both torque contributions to the total torque and reveals that the turbulence dominates the angular momentum transport for co-rotating cylinders since the mean-vortex torque $\overline{G}$ drops to the laminar value $G/G_{\mathrm{lam}} = 1$ for large μ. With increasing radius ratio, this drop occurs at a larger μ value in accordance with the shift of the Rayleigh stability boundary $\mu = \eta^2$ to larger rotation ratios. Similarly, the torque for strong counter-rotation is mainly caused by turbulent fluctuations. With increasing rotation ratio, the torque $\overline{G}$ due to the mean vortical motion becomes dominant approximately beyond $\mu = -\eta$ which corresponds to exact counter-rotation with $Re_o = -Re_i$. This onset of the mean vortical motion for $\mu > -\eta$ was previously observed experimentally by Ravelet, Delfos & Westerweel (2010). In addition, the mean vortices become stronger with μ decreasing from zero as evidenced by the torque contribution $\overline{G}$, except for $\eta = 0.9$ where the region of high mean-vortex torque is broader in μ. Again, the case $\eta = 0.9$ indicates that the flow behaviour changes for $\eta \to 1$, as will be explained in Chapter 4. We therefore omit a detailed discussion of the $\eta = 0.9$ case here. The vortex strengthening for $\mu < 0$ is consistent with our model, which predicts a change of the outer boundary from a rigid wall to a less restrictive free surface (cf. Figure 3.5). Like the total torque, the mean-vortex torque $\overline{G}$ shows a maximum for moderate counter-rotation. We determine its location $\mu_{\mathrm{LSC}}(\eta)$ by a quadratic fit to the data and find

maximum of mean-vortex torque

$$\begin{aligned} \mu_{\mathrm{LSC}}(0.5) &= -0.223 \pm 0.025, & \mu_{\mathrm{LSC}}(0.71) &= -0.380 \pm 0.059, \\ \mu_{\mathrm{LSC}}(0.8) &= -0.442 \pm 0.093, & \mu_{\mathrm{LSC}}(0.9) &= -0.441 \pm 0.058. \end{aligned} \tag{3.12}$$

In analogy to equation (3.4), the uncertainties in μ_{LSC} are calculated from the quadratic fit by assuming a 1% relative uncertainty in $\overline{G}$. Considering the uncertainties, the mean-vortex maximum location μ_{LSC} for $\eta = 0.5$, 0.71 and 0.8 is close to both the respective fluctuation onset μ_c and the predicted critical value μ_p as listed in Table 3.1. Moreover, Figure 3.7 suggests that the maximum in the mean-vortex torque forms the basis of the maximisation of the total torque for $\eta \leq 0.8$. Likewise, the presence of strong turbulent Taylor vortices for rotation ratios μ close to the maximum location $\mu_{\max}$ was confirmed at higher shear Reynolds numbers $Re_S \sim 10^5$ and $Re_S \sim 10^6$ in simulations (Ostilla-Mónico *et al.*, 2014c) and experiments (Huisman *et al.*, 2014). Overall, these observations suggest that the detachment of the unstable inner region first involves a strengthening of Taylor vortices and then their weakening when the bursting sets in, thereby causing the torque maximum. Consequently, the prediction for the bursting onset $\mu_p(\eta)$ derived from the detachment argument also serves as a prediction for the location of the maximum.

comparison to maximum locations

Therefore, in Figure 3.8 we compare the predictive line $\mu_p(\eta)$ from equation (3.10) as well as the angle bisector line $\mu_b(\eta)$ from (3.6) to empirically identified torque maximum locations. We find that the results for $\eta \approx 0.7$ from our DNS and the experiments in Twente and Maryland are consistent with both lines. Given the larger uncertainty, Wendt's experimental result

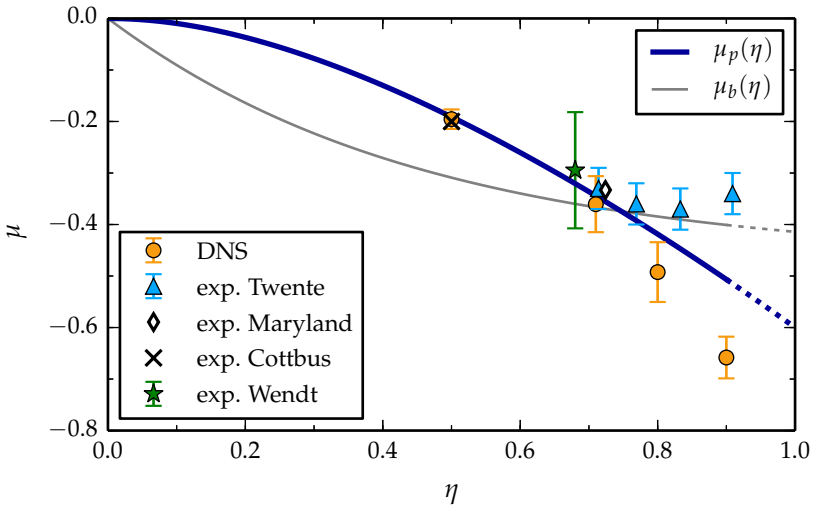

FIGURE 3.8: Location $\mu_{\max}$ of the torque maxima as a function of the radius ratio η. The circles mark the numerical results for $Re_S = 2 \times 10^4$ from Figure 3.4, and the other symbols show results for $Re_S \sim 10^5$ to 10^6 from experiments in Twente (Ostilla-Mónico *et al.*, 2014a), Maryland (Paoletti & Lathrop, 2011), Cottbus (Merbold, Brauckmann & Egbers, 2013) and by Wendt (1933). These are compared to the prediction $\mu_p(\eta)$ from equation (3.10) and to the angle bisector $\mu_b(\eta)$, equation (3.6), suggested by van Gils *et al.* (2012) for the maximum location.

for $\eta = 0.680$ also conforms with both the angle bisector and our prediction from the detachment argument. The maximum location in the wide-gap system ($\eta = 0.5$) is more distinctive, as the results from our DNS and the Cottbus experiment clearly favour the prediction $\mu_p(\eta)$. For $\eta > 0.7$, the results seem to be ambiguous: The torque maximum locations from the DNS differ from the experimental ones and are closer to $\mu_p(\eta)$, whereas the latter favour the angle bisector $\mu_b(\eta)$. However, we also note that the former are calculated at $Re_S = 2 \times 10^4$, and the latter are measured at much higher $Re_S \sim 10^5$ to 10^6. Accordingly, for large η the maximum location might still shift when Re_S increases beyond 2×10^4, in contrast to the agreement found between DNS and high-Re_S experiments for $\eta = 0.5$ and 0.71 (Section 2.6). But this shift in $\mu_{\max}$ is small in terms of the rotation number R_Ω, as the numerical and experimental result for $\eta = 0.9$ corresponds to $R_\Omega = 0.02$ and $R_\Omega = 0.04$, respectively. Finally, we note that in the limit of large cylinder radii for $\eta \to 1$, the stability properties of TCF change and the transition to turbulence follows a different route (Faisst & Eckhardt, 2000). Since the predictive model relies on the partitioning of the flow into an unstable inner and a stabilised outer region, we expect it to become invalid in the limit $\eta \to 1$ where this partitioning disappears. We account for the resulting uncertainty in the predictions by continuing the lines in Figure 3.8 with dashes for $\eta > 0.9$.

3.5 SUMMARY AND DISCUSSION

The presented results suggest that the torque increases with the onset of counter-rotation since the mean Taylor vortices gain in strength. For stronger counter-rotation, the torque drops again when the vortices detach from the outer cylinder wall and thereby create space for a stabilised outer region, which shows intermittent turbulent bursts. This picture resulted in the prediction $\mu_p(\eta)$ for both the bursting onset μ_c and the location of the torque maximum $\mu_{\max}$. For $\eta \approx 0.75$, which is close to the radius ratio where most experimental data are available, the angle bisector suggested by van Gils *et al.* (2012) and the current model result in indistinguishable predictions for the maximum location. But they differ for smaller radius ratios, where the numerical and experimental results for $\eta = 0.5$ are in line with our prediction $\mu_p(\eta)$. Hence, to further test the prediction, investigations of torque maxima for more radius ratios below 0.7 would be desirable.

While the prediction $\mu_p(\eta)$ presented here is in good agreement with all empirically observed bursting onsets (cf. Figure 3.6), it conforms with the torque maxima only for $\eta \lesssim 0.8$ and deviates for larger radius ratios (cf. Figure 3.8). Moreover, the torque maximum for $\eta = 0.8$ is not as pronounced as for the other radius ratios (cf. Figure 3.4). This suggests that, while the turbulent bursting is still present for large radius ratios, it becomes irrelevant for the determination of the torque maximum location. In this chapter, the results for $\eta = 0.9$ served as a precursor to illustrate the limitations of our physical model for large radius ratios. Furthermore, the flow partitioning into unstable inner and stabilised outer region disappears when η approaches 1. Since this partitioning has been linked to the bursts and the maximum location, we expect another torque-maximising mechanism in this limit. In the following Chapter 4, we therefore study the fate of the turbulent bursts and torque maxima in the limit $\eta \to 1$ and characterise the emerging new flow behaviour.

Moreover, numerical simulations for $\eta = 0.71$ revealed that for smaller $Re_S \leq 4 \times 10^3$, the torque maximum is located at $\mu_{\max} \approx 0$ (Brauckmann & Eckhardt, 2013a; Ostilla *et al.*, 2013), which differs from $\mu_{\max} = -0.33$ found experimentally at high Re_S. This low-Re_S maximum is not covered by the current predictive model. Thus, additional physical explanations are needed for the mildly turbulent regime. Some ideas in this direction will be presented in Chapter 5 where TCF is analysed using marginal stability theory.

4

THE LIMIT OF VANISHING CURVATURE*

The previous chapter showed that for a constant shear, the system rotation (parametrised by μ) has a considerable influence on the turbulence and momentum transport in TCF. In particular for counter-rotating cylinders, the flow is radially partitioned into a permanently turbulent inner region and a stabilised outer region with intermittent turbulent bursts. This radial difference in the turbulence is related to the curvature imposed by the cylinder walls. For small cylinder radii, i.e. η considerably below 1, the curvature becomes important. Conversely, for $\eta \to 1$ and a constant gap width d, the wall curvature vanishes since the cylinder radii diverge, and the TC system approximates RPCF, see Figure 4.1. In the latter system, no such difference in the turbulence near both walls exists. Consequently, also in TCF the radial partitioning of the flow has to disappear in the limit of vanishing curvature, when η approaches 1. Therefore, we here not only study the influence of rotation at a constant shear, but we also evaluate the effect of curvature on the turbulence. To this end, we analyse the changes occurring in the limit of vanishing curvature ($\eta \to 1$) and compare our results to the curvature-free limit of RPCF.

Since the torque-maximising rotation state has been linked to the occurrence of intermittent turbulence near the outer cylinder that decreases the momentum transport efficiency (van Gils *et al.*, 2012; Brauckmann & Eckhardt, 2013b) and the latter likely disappears for $\eta \to 1$, we also expect a change in the rotation dependence of the torque. Evidence for such deviations in behaviour between cases with $\eta < 0.9$ and larger η have also been noted in experiments with $\eta \approx 0.9$ (Ravelet, Delfos & Westerweel, 2010; Ostilla-Mónico *et al.*, 2014a). However, the rotation dependence in TC systems with a radius ratio significantly larger than 0.9 has not yet been explored and represents one of the main objectives of the present study. Moreover, we will study how turbulent characteristics, such as torques, mean profiles and fluctuations, change during the transition from TCF to RPCF and how TCF turns into RPCF.

In plane Couette flow, the effect of rotation depends on the relative orientation of rotation and vorticity. Cyclonic spanwise rotation, i.e. when the rotation vector is parallel to the vorticity of the laminar base flow, was found to have a stabilising effect on the turbulence (Komminaho, Lundbladh & Johansson, 1996) and to generate a striped pattern of coexisting laminar and turbulent regions (Tsukahara, 2011). Similar turbulent–laminar patterns were also observed at much higher shear rates by increasing the cyclonic rotation (Brethouwer, Duguet & Schlatter, 2012). On

* The results of this chapter have been published and the text follows closely the presentation in H. J. Brauckmann, M. Salewski & B. Eckhardt (2016). Momentum transport in Taylor–Couette flow with vanishing curvature. *J. Fluid Mech.* 790: 419–452.

the contrary, anticyclonic spanwise rotation, where the rotation is antiparallel to the base-flow vorticity, has a destabilising effect and was found to drive vortices reminiscent of turbulent Taylor vortices (Bech & Andersson, 1997; Barri & Andersson, 2010; Tsukahara, 2011). For strong anticyclonic rotations, these vortices break up again and become disorganised. The influence of rotation on the strength of vortices is of substantial interest also in the present study since such vortices can enhance the momentum transport and, therefore, contribute to the formation of torque maxima, as demonstrated in Section 3.4 and Brauckmann & Eckhardt (2013b).

Investigations of RPCF for anticyclonic rotation furthermore revealed that the mean downstream velocity profile exhibits a linear section in the centre of the gap. In this region, which can extend over a considerable fraction of the gap, the vorticity of the mean profile compensates the imposed vorticity of the spanwise rotation (Bech & Andersson, 1997; Barri & Andersson, 2010; Suryadi, Segalini & Alfredsson, 2014). As a consequence, in the central region, the gradient of the profile increases linearly with the imposed rotation rate. A physical explanation for these profile shapes in the central region comes from the observation that mean profiles of zero absolute vorticity comply with neutral stability in RPCF (Barri & Andersson, 2010; Suryadi, Segalini & Alfredsson, 2014). Such prominent changes of the profile gradient with varying system rotation were also observed for the angular velocity in TCF (Wendt, 1933; van Gils *et al.*, 2012; Brauckmann & Eckhardt, 2013a; Ostilla *et al.*, 2013; Ostilla-Mónico *et al.*, 2014a). However, it remains unclear how the mean profiles in TCF compare to those in RPCF and whether they converge in the limit of vanishing curvature ($\eta \to 1$).

The purpose of the present study is to examine the continuous transition from TCF to RPCF and to compare turbulent characteristics between both systems taking into account the following aspects. First, we quantify the effect of the vanishing curvature, when η tends to unity, by the decreasing strength of intermittent fluctuations near the outer cylinder and by the local stability for counter-rotating cylinders. Second, we show that as these intermittent fluctuations disappear, the rotation dependence of the torque also changes. Third, we look for flow characteristics that prove the convergence of TCF to RPCF and seek the η range in which the convergence can be observed. Fourth, the magnitudes of the momentum transport by coherent vortices are analysed to assess their importance for the formation of torque maxima. In addition, we evaluate the effect of turbulent fluctuations on the momentum transport. Finally, we look for a convergence of streamwise velocity profiles and introduce a unified description of profile gradients in the central region in TCF and RPCF.

This chapter is structured as follows. In Section 4.1 we describe the unified framework in which we study TCF and RPCF, including the equations of motion, common control parameters and the momentum transport equations. The vanishing of curvature effects is studied in Section 4.2, followed by an analysis of the total momentum transport in Section 4.3 and of the vortex-induced momentum transport in Section 4.4. Finally, we

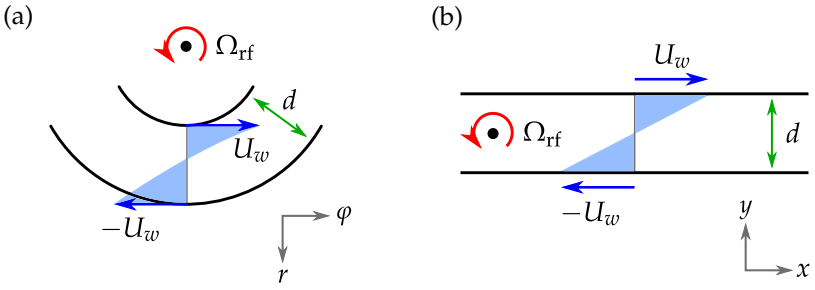

FIGURE 4.1: Schematic representations of the two flows. (a) TC system seen from above in the reference frame rotating with Ω_{rf}. Only one third of the azimuthal circumference is shown, reflecting the actual computational domain for $\eta = 0.5$. (b) RPCF, as obtained from (a) for vanishing curvature, i.e. when $\eta \to 1$ for a constant gap width d. While the spanwise z-coordinate points out of the paper in both systems, the wall-normal coordinates r and y are antiparallel.

discuss the rotation dependence of velocity profiles and of turbulent fluctuations contributing to the momentum transport in Section 4.5. We close with a summary and some concluding remarks.

4.1 UNIFIED FRAMEWORK FOR TCF AND RPCF

RPCF framework

Since several different combinations of parameters are used in TCF, we begin by discussing the limiting case of RPCF, so that we can then chose parameters that correspond to the ones in RPCF. As usual, RPCF refers to the flow between two parallel walls that move in opposite directions and are subject to system rotation in the spanwise direction. In the rotating reference frame, we describe this system in Cartesian coordinates (x, y, z) with the velocity field $\boldsymbol{u} = (u_x, u_y, u_z)$ and the walls at $y = -h$ and $y = h$ moving in the x-direction with velocities $-U_w$ and U_w, respectively. The entire system rotates with angular velocity $\boldsymbol{\Omega}_{rf} = \Omega_{rf}\boldsymbol{e}_z$ around the spanwise axis as depicted in Figure 4.1(b). We chose $d = 2h$ and $U_0 = 2U_w$ as characteristic scales for all lengths and velocities. In these units and in a reference frame rotating with Ω_{rf}, the Navier–Stokes equations and incompressibility condition become

$$\partial_t \boldsymbol{u} + (\boldsymbol{u}\cdot\boldsymbol{\nabla})\boldsymbol{u} = -\boldsymbol{\nabla} p - R_\Omega\, \boldsymbol{e}_z \times \boldsymbol{u} + \frac{1}{Re_S}\Delta\boldsymbol{u}, \qquad \boldsymbol{\nabla}\cdot\boldsymbol{u} = 0, \tag{4.1}$$

where p denotes the non-dimensionalised pressure; the centrifugal force has been absorbed into the pressure. The motion is characterised by two dimensionless parameters, the shear Reynolds number Re_S and the rotation number R_Ω which measures the ratio between system rotation and shear,

$$Re_S = \frac{U_0\, d}{\nu}, \qquad R_\Omega = \frac{2\Omega_{rf}\, d}{U_0}, \tag{4.2}$$

RPCF parameters

where ν denotes the kinematic viscosity of the fluid. In contrast to the often used plane Couette flow Reynolds number $Re = U_w h/\nu$, the definition

of the shear Reynolds number Re_S is based on the full velocity difference and wall distance, so that $Re_S = 4Re$.

TCF framework

Instead of plane walls, TCF is driven by concentric cylinders. Its geometric parameters are the inner and outer cylinder radii r_i and r_o and the axial height L_z. The radius ratio, defined as $\eta = r_i/r_o$, determines the curvature; it is thus the parameter that controls the transition to RPCF (which emerges for $\eta \to 1$). The inner and outer cylinders rotate with angular velocities ω_i and ω_o, respectively, and their ratio $\mu = \omega_o/\omega_i$ or its negative, $a = -\mu$, (van Gils *et al.*, 2011; Brauckmann & Eckhardt, 2013a; Ostilla *et al.*, 2013) is often used to define the rotation state of the system. In order to study TCF in the same framework as RPCF, we follow the analysis of Dubrulle *et al.* (2005) and describe the flow in a reference frame that rotates with the angular velocity Ω_{rf}. We make use of the cylindrical symmetry and introduce coordinates (r, φ, z) with velocities $\boldsymbol{u} = (u_r, u_\varphi, u_z)$. In analogy to RPCF, we choose Ω_{rf} such that the cylinder walls move symmetrically in opposite directions in the rotating reference frame, i.e. such that the condition $u_\varphi(r_i) = -u_\varphi(r_o) \equiv U_w$ is fulfilled as depicted in Figure 4.1(a). This gives

$$r_i(\omega_i - \Omega_{\text{rf}}) = -r_o(\omega_o - \Omega_{\text{rf}}) \quad \Leftrightarrow \quad \Omega_{\text{rf}} = \frac{r_i\omega_i + r_o\omega_o}{r_i + r_o}. \tag{4.3}$$

As the characteristic velocity scale U_0, we choose the velocity difference between the cylinder walls in the rotating reference frame, i.e.

$$\begin{aligned} U_0 &\equiv u_\varphi(r_i) - u_\varphi(r_o) = r_i\omega_i - r_o\omega_o + (r_o - r_i)\Omega_{\text{rf}} \\ &= \frac{2}{1+\eta}(r_i\omega_i - \eta r_o\omega_o). \end{aligned} \tag{4.4}$$

The last step in (4.4) results from substituting Ω_{rf} from equation (4.3). With a view towards the variables in RPCF, we take the gap width $d = r_o - r_i$ as the characteristic scale to measure all lengths. Instead of the radius ratio η, Dubrulle *et al.* (2005) specify a typical radius $\widetilde{r} = \sqrt{r_i r_o}/d$ and define the curvature number $R_C = 1/\widetilde{r}$ to characterise the curvature of the system. (The relation to η is given in equation (4.8) below, where the definitions of all parameters are collected.) Using these units, the equations of motion in cylindrical coordinates (Landau & Lifshitz, 1987) transformed to the rotating reference frame can be written as

$$\begin{aligned} \partial_t \boldsymbol{u} + (\boldsymbol{u}\cdot\widetilde{\boldsymbol{\nabla}})\boldsymbol{u} &= -\widetilde{\boldsymbol{\nabla}}p - R_\Omega\,\boldsymbol{e}_z\times\boldsymbol{u} + \frac{1}{Re_S}\widetilde{\Delta}\boldsymbol{u} \\ &\quad + R_C\,\frac{\widetilde{r}}{r}\left[u_\varphi^2\boldsymbol{e}_r - u_r u_\varphi \boldsymbol{e}_\varphi + \frac{1}{Re_S}\left(\partial_r\boldsymbol{u} + \frac{2}{r}\partial_\varphi(\boldsymbol{e}_z\times\boldsymbol{u})\right)\right] \\ &\quad + \frac{{R_C}^2}{Re_S}\,\frac{\widetilde{r}^2}{r^2}\,(u_r\boldsymbol{e}_r + u_\varphi\boldsymbol{e}_\varphi), \end{aligned} \tag{4.5}$$

$$\widetilde{\boldsymbol{\nabla}}\cdot\boldsymbol{u} = -R_C\,\frac{\widetilde{r}}{r}u_r, \tag{4.6}$$

with the modified Nabla and Laplace operators

$$\widetilde{\boldsymbol{\nabla}} = \boldsymbol{e}_r\partial_r + \boldsymbol{e}_\varphi\frac{1}{r}\partial_\varphi + \boldsymbol{e}_z\partial_z, \qquad \widetilde{\Delta} = \partial_r^2 + \frac{1}{r^2}\partial_\varphi^2 + \partial_z^2. \tag{4.7}$$

Again, the centrifugal force is absorbed in a modified pressure p. The terms in (4.5) and (4.6) are arranged in a form adapted from Faisst & Eckhardt (2000) in order to clarify that in the limit $\eta \to 1$ the equations of motion (4.5) and (4.6) indeed converge to the corresponding ones for RPCF (4.1) since the additional terms on the right-hand side vanish as $R_C \to 0$. The transition between Cartesian coordinates in RPCF and cylindrical coordinates in TCF requires the identifications $x = r\varphi$ and $y \sim r$.

The equations of motion show that the TC system is characterised by three dimensionless parameters (Dubrulle *et al.*, 2005),

$$\begin{aligned} Re_S &= \frac{U_0\, d}{\nu} = \frac{2}{1+\eta}(Re_i - \eta Re_o), \\ R_\Omega &= \frac{2\Omega_{\mathrm{rf}}\, d}{U_0} = (1-\eta)\frac{Re_i + Re_o}{Re_i - \eta Re_o}, \qquad R_C = \frac{1}{\widetilde{r}} = \frac{1-\eta}{\sqrt{\eta}}, \end{aligned} \tag{4.8}$$

TCF parameters

that result from (4.3) and (4.4), where $Re_i = r_i\omega_i d/\nu$ and $Re_o = r_o\omega_o d/\nu$ denote the traditional Reynolds numbers that measure the dimensionless velocity of the inner and outer cylinders in the inertial frame of reference. Note that Re_S and R_Ω are defined in strict analogy to RPCF (4.2) so that R_Ω has the opposite sign to the rotation number used by Dubrulle *et al.* (2005), Ravelet, Delfos & Westerweel (2010) and Paoletti *et al.* (2012).

4.1.1 *Parameters for the limit of vanishing curvature*

We are interested in the transition from TCF to RPCF, in the limit when the radius ratio $\eta = r_i/r_o$ approaches one. This limit is often called the small-gap limit, since it can be obtained for fixed outer radius when the radius of the inner cylinder approaches that of the outer one and the gap width $d = r_o - r_i$ ultimately vanishes. However, in units of the width d, the radii increase like $r_i, r_o \sim 1/(1-\eta)$ and diverge as η approaches one; this is why this situation was called the *limit of large radii* in Faisst & Eckhardt (2000). Moreover, the curvature vanishes ($R_C \to 0$) as $\eta \to 1$, suggesting that curvature effects become less important. However, rotation effects can be maintained.

divergence of Re_i and Re_o

For every radius ratio η, the traditional Reynolds numbers can be expressed in terms of the shear Reynolds number and the rotation number as

$$Re_i = \frac{Re_S}{2} + \frac{\eta}{2(1-\eta)} Re_S\, R_\Omega, \qquad Re_o = -\frac{Re_S}{2} + \frac{1}{2(1-\eta)} Re_S\, R_\Omega \tag{4.9}$$

and more specifically as $Re_i = Re_S/2$ and $Re_o = -Re_S/2$ in the non-rotating case ($R_\Omega = 0$) independent of η. In contrast, for finite rotation ($R_\Omega \neq 0$), the cylinder Reynolds numbers Re_i and Re_o diverge in the vanishing-curvature limit as $\eta \to 1$. As a consequence, the ratio of angular velocities,

$$\mu = \eta \frac{Re_o}{Re_i} = \frac{-\eta(1-\eta) + \eta R_\Omega}{(1-\eta) + \eta R_\Omega}, \tag{4.10}$$

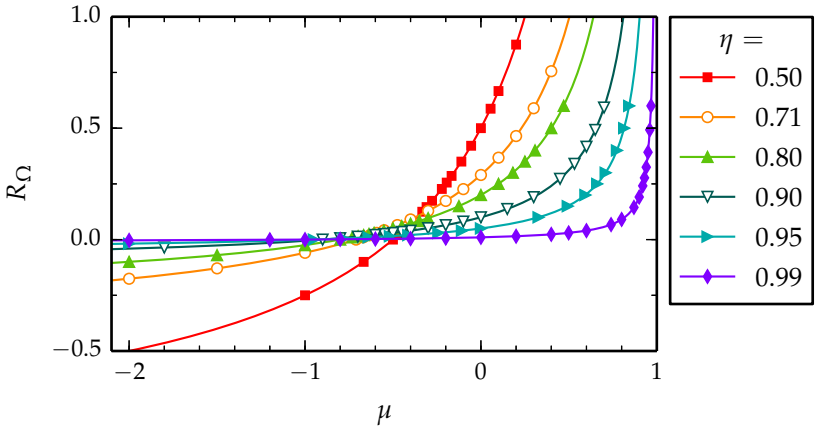

FIGURE 4.2: Transformation between the ratio of angular velocities $\mu = \omega_o/\omega_i$ and the rotation number R_Ω for various radius ratios η. For TC systems with vanishing curvature ($\eta \to 1$), most μ values result in almost no system rotation ($R_\Omega \approx 0$) and $R_\Omega > 0$ is achieved only for μ close to one. The symbols mark the values of μ and R_Ω realised by our simulations for $Re_S = 2 \times 10^4$.

converges to $\mu = -1$ for $R_\Omega = 0$ and to $\mu = 1$ for any $R_\Omega \neq 0$ in the vanishing-curvature limit, as shown in Figure 4.2. These limiting values illustrate that the transition between TCF and RPCF is singular in the traditional parameters, Re_i, Re_o and μ, but not in the parameters Re_S and R_Ω that we will generally use here. We note that one exception to this parameter choice occurs in Section 4.2 where the effect of curvature for counter-rotating cylinders can be characterised more adequately by the ratio of angular velocities μ. Furthermore, while R_C measures the curvature and thus clarifies its disappearance ($R_C \to 0$) for $\eta \to 1$, we will identify the different TC geometries by the radius ratio η as this parameter is more commonly used.

4.1.2 *Momentum transport in TCF and RPCF*

To study the mean turbulent characteristics of the flow, we calculate wall-normal profiles of the velocity and other flow fields by averaging over surfaces parallel to the wall. The averages are denoted by $\langle\cdots\rangle_A$. The surfaces are concentric cylinders in the case of TCF, $\langle\cdots\rangle_A(r) = \langle\cdots\rangle_{\varphi z}$, and planes parallel to the bounding walls in the case of RPCF, $\langle\cdots\rangle_A(y) = \langle\cdots\rangle_{xz}$. Equations for the averages follow from the Navier–Stokes equations. The average of the φ-component of the equations of motion (4.5) of TCF results in the continuity equation for the specific angular momentum $\mathcal{L} = ru_\varphi$

angular momentum transport in TCF

$$\partial_t\langle\mathcal{L}\rangle_A + r^{-1}\partial_r(rJ^{\mathcal{L}}) = 0 \quad \text{with} \quad J^{\mathcal{L}} = \langle u_r\mathcal{L}\rangle_A - Re_S^{-1}r^2\partial_r\langle\omega\rangle_A, \quad (4.11)$$

where $J^{\mathcal{L}}$ denotes the angular-momentum flux in dimensionless units (Marcus, 1984a), $\omega = u_\varphi/r$ the angular velocity and $r^{-1}\partial_r(rJ^{\mathcal{L}})$ the divergence in radial direction. In the statistically stationary state, where $\partial_t\langle\mathcal{L}\rangle_A = 0$, the transverse current $J^\omega = rJ^{\mathcal{L}}$ becomes independent of the radius (Eckhardt, Grossmann & Lohse, 2007b). In physical units, the torque T needed

to drive the cylinders can be calculated from the dimensionless angular-momentum flux $J^{\mathcal{L}}$ as $T = \rho_f \nu^2 d\, Re_S^2\, A(r)\, J^{\mathcal{L}}$, with the dimensionless cylindrical surface area $A(r) = 2\pi r L_z$ and the mass density of the fluid ρ_f. The remaining prefactors compensate for the non-dimensionalisation of (4.11). We define the dimensionless torque per axial length,

$$G = \frac{T}{2\pi L_z \rho_f \nu^2 d} = Re_S^2\, r J^{\mathcal{L}} = Re_S^2\, J^{\omega}, \tag{4.12}$$

and introduce the Nusselt number,

$$Nu_\omega = G/G_{\text{lam}} = J^{\omega}/J^{\omega}_{\text{lam}}, \tag{4.13}$$

that measures the torque in units of the torque of the laminar profile G_{lam} (Dubrulle & Hersant, 2002; Eckhardt, Grossmann & Lohse, 2007a).

Equations corresponding to (4.11)–(4.13) can also be derived for RPCF. Averaging the downstream component of the equations of motion (4.1) results in a continuity equation for the specific momentum in the x-direction

$$\partial_t \langle u_x \rangle_A + \partial_y J^u = 0 \qquad \text{with} \qquad J^u = \langle u_y u_x \rangle_A - Re_S^{-1} \partial_y \langle u_x \rangle_A \tag{4.14}$$

momentum transport in RPCF

(see also Pope, 2000, §7.1), where J^u denotes the momentum flux in dimensionless units. In the statistically stationary state, it is independent of the wall-normal coordinate y. In analogy to the torque T, the force F needed to keep the plane walls at a constant velocity can be calculated from the momentum flux J^u multiplied by the dimensionless surface area $A_{xz} = L_x L_z$ through which the flux passes, $F = \rho_f \nu^2 Re_S^2\, A_{xz}\, J^u$. Finally, we define the Nusselt number for the momentum transport in RPCF as in (4.13),

$$Nu_u = F/F_{\text{lam}} = J^u/J^u_{\text{lam}}, \tag{4.15}$$

that measures the force in units of the value F_{lam} for the laminar flow. Lastly, since we only study statistically stationary cases, we also average in time to improve the statistics. This means that instead of the area-average $\langle \cdots \rangle_A$, we use the area-time average $\langle \cdots \rangle_{\varphi z t}$ for TCF or $\langle \cdots \rangle_{x z t}$ for RPCF to obtain wall-normal profiles. For simplicity, we denote the area-time average by $\langle \cdots \rangle$.

relations between TCF and RPCF

This completes our set of relations between TCF and RPCF that we want to study here. We have identified correspondences between the continuity equations (4.11) and (4.14), the torque and the force ($T \leftrightarrow F$), the angular-momentum flux and the momentum flux ($J^{\mathcal{L}} \leftrightarrow J^u$), the Nusselt numbers ($Nu_\omega \leftrightarrow Nu_u$) and the mean profiles that enter the diffusive part of the flux in (4.11) and (4.14) ($\langle \omega \rangle(r) \leftrightarrow \langle u_x \rangle(y)$). Using the dimensionless shear Reynolds number Re_S and rotation number R_Ω (4.2), we can now study the momentum transport in both systems within the same framework and in a non-singular manner.

We conclude this section by pointing out a peculiar property of the relations that we will take up again in later sections. While the equations of motion (4.1) and (4.5) depend on both driving parameters Re_S and R_Ω, the

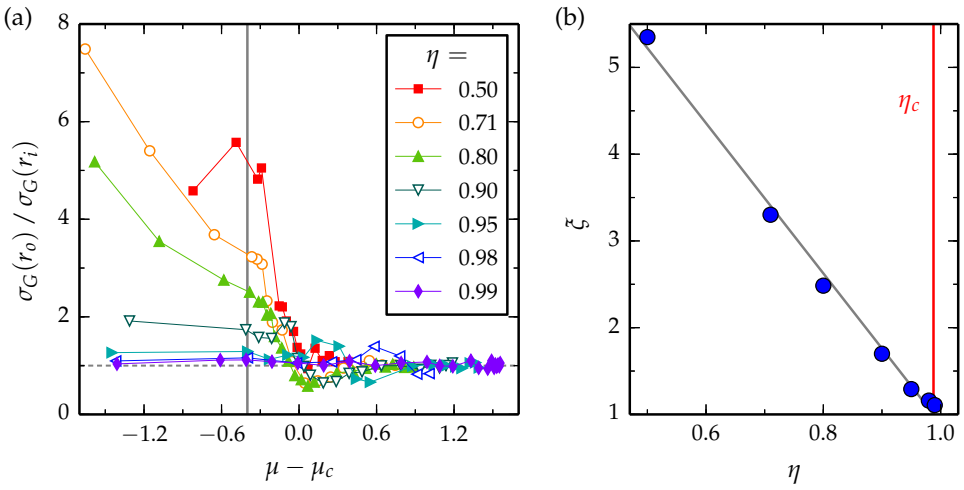

FIGURE 4.3: Enhanced outer fluctuations for $Re_S = 2 \times 10^4$ as a function of the radius ratio η, assessed by the standard deviation of temporal torque fluctuations σ_G. (a) Ratio of σ_G computed at the outer and at the inner cylinder versus the shifted rotation ratio $\mu - \mu_c$, where μ_c denotes the critical value for the onset of enhanced fluctuations from Figure 3.6. For $\eta \geq 0.95$, μ_p was subtracted instead of μ_c. (b) Typical fluctuation ratio $\xi = \sigma_G(r_o)/\sigma_G(r_i)$ calculated by interpolation at $\mu - \mu_c = -0.4$ marked by the vertical line in (a). The diagonal line represents a best fit to the data and indicates the disappearance of the fluctuation asymmetry near $\eta_c = 0.99 \pm 0.01$.

momentum transport equations (4.11) and (4.14) do not explicitly depend on the rotation number R_Ω, as noted for RPCF by Salewski & Eckhardt (2015). The rotation only indirectly influences the momentum fluxes $J^{\mathcal{L}}$ and J^u by changing the turbulent velocity correlations ($\langle u_r \mathcal{L} \rangle$ and $\langle u_y u_x \rangle$) and the mean profiles ($\langle \omega \rangle$ and $\langle u_x \rangle$), as we will discuss for the correlations in Section 4.4.1 and Section 4.5.3 and for the profiles in Section 4.5.2.

4.2 VANISHING OF CURVATURE EFFECTS

Section 3.1 showed that the stabilisation of the flow caused by counter-rotating the outer cylinder results in turbulent bursts in the outer region. The strength of this intermittent behaviour, and thus of the radial difference in the turbulence, was quantified by increased torque fluctuations at the outer cylinder. As the stabilisation and intermittency in the outer region are expected to be curvature effects, we here study their fate in the limit of vanishing curvature.

In Figure 4.3(a), we analyse the variation of the torque fluctuation amplitudes with changing radius ratio $\eta \to 1$. For the sake of visual clarity when comparing all investigated η, we show the ratio between the standard deviation σ_G of the torque at the outer and at the inner cylinder. A value greater than one indicates enhanced outer fluctuations. Moreover, the rotation ratio μ is shifted by the critical value μ_c in order to align the respective regions of enhanced outer fluctuations. The small difference

in σ_G for $\eta \geq 0.95$ is the reason why we omitted a similar analysis as in Figure 3.3 for the three highest radius ratios. To quantify the fluctuation asymmetry for strong counter-rotation, we define a typical fluctuation ratio $\xi = \sigma_G(r_o)/\sigma_G(r_i)$ at the shifted rotation ratio $\mu - \mu_c = -0.4$ for each radius ratio. Figure 4.3(b) shows that this asymmetry measure, ξ, decreases monotonically with η towards a value of 1, which signifies equal fluctuation strengths near the inner and outer cylinder. The fluctuation asymmetry vanishes for a radius ratio of $\eta_c = 0.99 \pm 0.01$, which does not differ significantly from 1. This suggests that small differences between inner and outer cylinder turbulence exist for all $\eta < 1$. Therefore, in this case, curvature has an effect for any $\eta \neq 1$.

disappearance of the fluctuation asymmetry

The disappearance of the fluctuation asymmetry may also be related to the local stability properties of the flow. The results in Figure 4.3 suggest that the separation into an unstable inner region and a stabilised outer region disappears as $\eta \to 1$. However, the neutral surface for counter-rotation, where in the inertial frame the velocity profile passes through zero, discriminates the stability regions and exists for all η. Therefore, the radial partitioning has to vanish in a different way for $\eta \to 1$, as we will see from local stability results. Eckhardt & Yao (1995) investigated the evolution of local perturbations to the laminar Couette profile $\hat{\omega}_{\text{lam}}(r)$ (equation (1.10)) along Lagrangian trajectories. For the perturbation modes with radial and axial wavenumbers k_1 and k_3, they calculated radially dependent eigenvalues

local stability analysis

$$\lambda_{\pm}(r) = -\frac{1}{Re_S} k_1^2 (1+\beta) \pm \left[-\frac{2\hat{\omega}_{\text{lam}}}{r} \partial_r \left(r^2 \hat{\omega}_{\text{lam}} \right) \frac{\beta}{1+\beta} \right]^{1/2}, \tag{4.16}$$

with the squared wavenumber ratio $\beta = k_3^2/k_1^2$ (see also the local stability results by Dubrulle (1993)). Note that the $\hat{\omega}_{\text{lam}}$-dependent factor in the second term of (4.16) corresponds to Rayleigh's stability discriminant. In the following, we focus on the largest (most unstable) eigenvalue that can be calculated for given Re_S and μ by maximising $\lambda_+(r)$ at the most unstable radial position $r = r_i$. For that purpose, we minimise the viscous damping (first term in (4.16)) by selecting the smallest possible radial wavenumber

$$k_1 = \begin{cases} \pi/(r_o - r_i), & \mu \geq 0 \\ \pi/(r_n - r_i), & \mu < 0 \end{cases} \qquad \text{with} \qquad r_n = r_i \sqrt{\frac{1-\mu}{\eta^2 - \mu}}. \tag{4.17}$$

Subsequently, we determine the wavenumber ratio $\beta_{\max}$ that maximises equation (4.16). With these optimal values for k_1 and β, we study the radial variation of the largest eigenvalue $\widetilde{\lambda}_+$.

To analyse the local stability for strong counter-rotation, Figure 4.4 shows radial profiles of $\widetilde{\lambda}_+$ for $Re_S = 2 \times 10^4$ and the specific angular velocity ratio $\mu = -\eta$. This value is comparable to the value $\mu - \mu_c = -0.4$ used in the study of the fluctuation asymmetry in Figure 4.3. The positive real part of the eigenvalue $\widetilde{\lambda}_+$ inside the neutral surface indicates

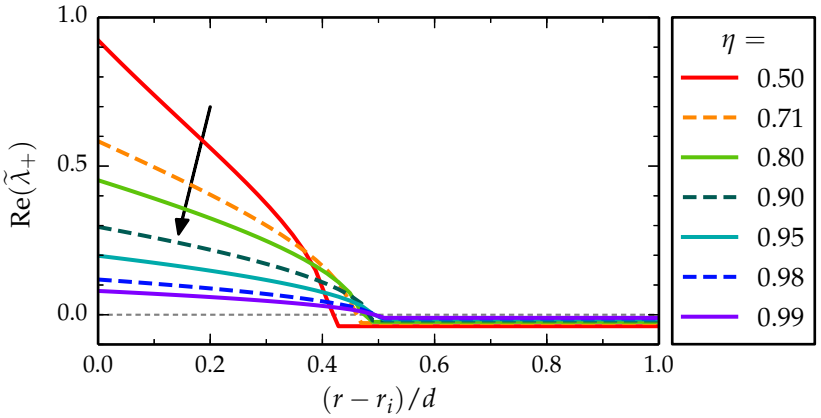

FIGURE 4.4: Radial dependence of the centrifugal instability for $Re_S = 2 \times 10^4$ and $\mu = -\eta$ (i.e. $R_\Omega = 0$) where the neutral surface is located in the centre of the cylinder gap. The real part of the largest eigenvalue $\widetilde{\lambda}_+$ from the local stability analysis along Lagrangian paths (Eckhardt & Yao, 1995) is shown for various radius ratios η. The radial partitioning of stability decreases with increasing $\eta \to 1$ (indicated by the arrow).

disappearance of stability difference

instability in the inner region while the outer region is vicously damped. Most importantly, the radial variation of the local stability decreases with η which is reminiscent of the disappearance of the radial differences in the fluctuation behaviour. With increasing η, the eigenvalues move in opposite directions: in the inner region, they become less unstable and approach neutral stability from above, whereas in the outer region, they approach the neutral value from below.

The results of this section show that for counter-rotation the turbulence in the inner and outer region differs for all $\eta < 1$, as the enhanced outer fluctuations demonstrate. However, this curvature effect, as well as the radial variation of the local stability, disappear with vanishing curvature for $\eta \to 1$. The disappearance of the intermittent bursts in the outer region is also relevant for an understanding of the variation of torque, since in Chapter 3 the appearance of these bursts has been linked to the emergence of a torque maximum, see also van Gils *et al.* (2012) and Brauckmann & Eckhardt (2013b). The absence of this intermittency should therefore change the variation of torque with rotation, as we now discuss.

4.3 VARIATION OF THE MOMENTUM TRANSPORT

We now turn to the rotation dependence of the mean torque with increasing Re_S and with variations in radius ratio. Figure 4.5 shows the Nusselt number Nu_ω, the torque in units of its laminar value. For the wide-gap TC system with $\eta = 0.5$, the torque maximum initially occurs at $R_\Omega \sim 0.3$ for $Re_S = 5 \times 10^3$ and then shifts to $R_\Omega = 0.26$ for $Re_S = 2 \times 10^4$ corresponding to $\mu = -0.20$, as also shown in Figure 2.9, Brauckmann & Eckhardt (2013b) and Merbold, Brauckmann & Egbers (2013). For $\eta = 0.71$ this shift in the maximum is more pronounced, with R_Ω varying from 0.27 at

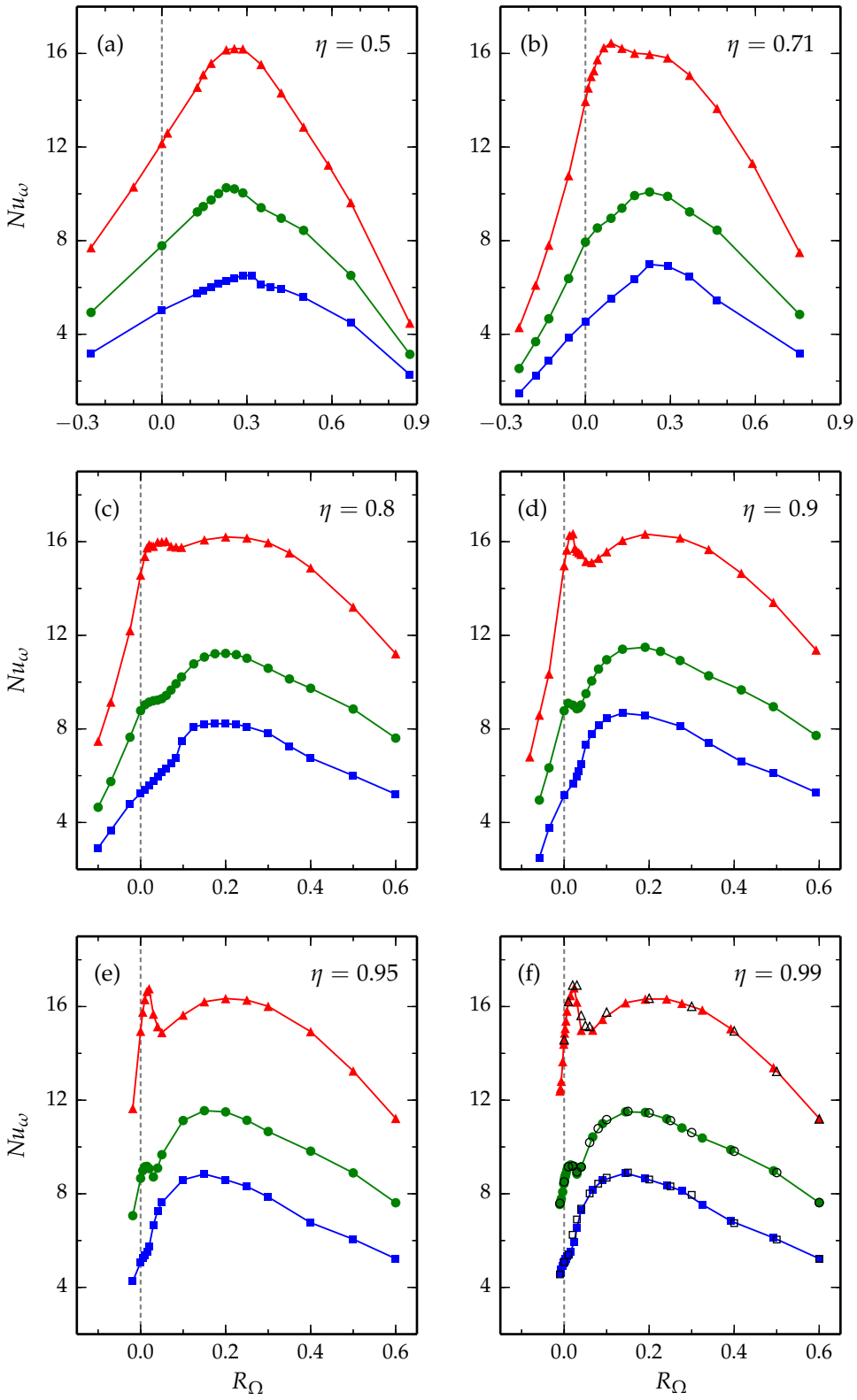

FIGURE 4.5: Variation of the momentum transport (Nu_ω) with changing system rotation (R_Ω) calculated for the radius ratios η specified in the sub-figures. The simulations are performed for $Re_S = 5 \times 10^3$ (■), $Re_S = 10^4$ (●) and $Re_S = 2 \times 10^4$ (▲). The open symbols in (f) show results from simulations of RPCF. Note the increased R_Ω-scale in (a) and (b).

$Re_S = 5 \times 10^3$ to 0.11 at $Re_S = 2 \times 10^4$ (Figure 4.5(b)). For even higher Re_S, the experiments of Paoletti & Lathrop (2011) and van Gils *et al.* (2011, 2012) show no further shift in the position of the torque maximum so that $R_\Omega = 0.11$ is likely to be close to the asymptotic value for high Re_S. As discussed in Chapter 3, these high-Re_S torque maxima for $\eta = 0.5$ and 0.71 coincide with the onset of intermittent bursts in the outer region.

two torque maxima

The situation changes drastically for low-curvature TCF with $\eta \geq 0.9$ as shown in Figure 4.5(d)–(f): instead of a single maximum, one notes a broad torque maximum near $R_\Omega = 0.2$ and a second narrow maximum near $R_\Omega = 0.02$. This narrow maximum emerges with increasing shear and, at $Re_S = 2 \times 10^4$, is similar in magnitude to the broad maximum. Indications for the narrow maximum were first seen by Ravelet, Delfos & Westerweel (2010)† in a low-curvature TC experiment ($\eta = 0.917$): Their data show a very slight bump in the torque near $R_\Omega = 0.02$ for $Re_S = 1.4 \times 10^4$ and 1.7×10^4 and a monotonic increase with R_Ω for $R_\Omega \gtrsim 0.05$. However, their figure 8 only shows torque measurements for $R_\Omega < 0.125$ so that the broad maximum found here at $R_\Omega = 0.2$ lies outside their investigated range. The presence of two maxima, a broad one and a narrow one that emerges with increasing Re_S, was also observed in RPCF (Salewski & Eckhardt, 2015). They compare well to the Nu_ω maxima in low-curvature TCF as demonstrated for $\eta = 0.99$ in Figure 4.5(f).

Finally, the torque for $\eta = 0.8$ (Figure 4.5(c)) shows a behaviour intermediate between that of the narrow-gap and the wide-gap TC systems. While the broad torque maximum known from systems with larger radius ratios is present, the second maximum around $R_\Omega = 0.02$ is not as narrow and as clearly visible as for $\eta \geq 0.9$. On the other hand, the extrapolation of equation (3.10), which captures the maximum for $\eta = 0.5$ and 0.71, to the case $\eta = 0.8$ predicts a maximum at $\mu_p = -0.419$ and $R_{\Omega,p} = 0.069$. This is close to the low-curvature narrow maximum and suggests that the two will interfere. Indeed, the magnification in Figure 4.6(b) of the region in R_Ω around the low-curvature narrow peak shows both, a slight maximum at $R_\Omega = 0.02$ and a broader one around $R_\Omega = 0.05$.

collapse of Nu_ω for various η

In Figure 4.6, we show the torque as a function of the rotation number for various radius ratios. In order to compensate for the slightly different Re_S of the compared torques, we use the observation by Dubrulle *et al.* (2005) that the torque variation can be decomposed into a scaling with Re_S modulated by an amplitude that describes the dependence on R_Ω and we thus normalise the torques by ${Re_S}^{0.78}$. For $\eta \geq 0.9$, the Nusselt numbers for different radius ratios collapse. The figure also contains data from RPCF which also agree nicely with those of low-curvature TCF. Data collapse is also observed with other quantities. Dubrulle *et al.* (2005) previously noted that the torque G normalised by its value for stationary outer cylinder $G(\mu = 0)$ varies only little with η when plotted as function of R_Ω. Similarly, Paoletti *et al.* (2012) found a collapse of another torque ratio $G/G(R_\Omega = 0)$ as a function of R_Ω for various radius ratios. Our

† The rotation number Ro used by these authors is of opposite sign, i.e. $Ro = -R_\Omega$.

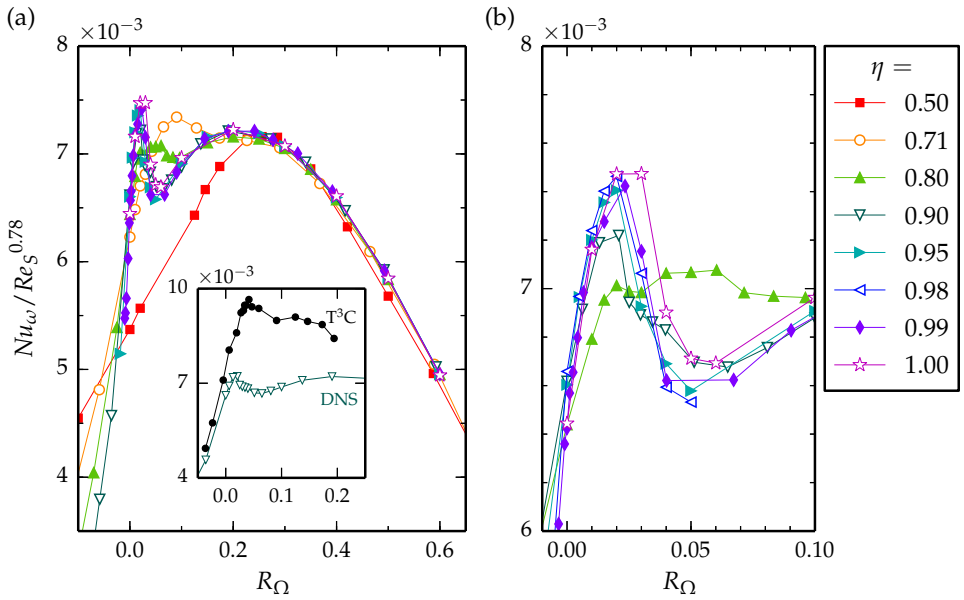

FIGURE 4.6: Comparison of the momentum transport (Nu_ω) for various radius ratios as a function of the system rotation (R_Ω) at $Re_S = 2 \times 10^4$. The values are compensated with a scaling in Re_S employing the scaling exponent measured by van Gils *et al.* (2012). Sub-figure (b) details the narrow maximum in (a). For purposes of clarity, the results for $\eta = 0.98$ are only included in (b) where the ones for $\eta = 0.5$ and $\eta = 0.71$ are left out. The open stars labelled by $\eta = 1.00$ show results from RPCF simulations. The inset in (a) compares our DNS results for $\eta = 0.9$ to the T³C-experiment with $\eta = 0.909$ and Re_S of a few 10^5 (Ostilla-Mónico *et al.*, 2014a) and reveals a slight shift of the maximum with increasing Re_S from $R_\Omega = 0.02$ to $R_\Omega = 0.04$.

Figure 4.6 shows that a normalisation by the laminar torque suffices to compensate for the curvature dependence and to achieve the collapse for $\eta \geq 0.9$. Note that $\mu = 0$ corresponds to $R_\Omega = 1 - \eta$ so that the normalisation by $G(\mu = 0)$ has an additional η-dependence compared to the normalisation by $G(R_\Omega = 0)$. In all three cases, the collapse of the data is of similar quality and does not favour one particular normalisation. However, plots with respect to μ (cf. Figure 3.4) do not yield such a collapse, confirming that R_Ω is the appropriate parameter in which to describe the transition from TCF to RPCF.

influence of curvature

For lower η, the collapse of the torques is limited to the region $R_\Omega \gtrsim 0.1$ for $\eta = 0.8$ and to $R_\Omega \gtrsim 0.25$ for $\eta = 0.5$ and 0.71. For these rotation numbers, turbulent bursting does not occur in the outer region. For smaller R_Ω, where the bursting in the outer region occurs, the Nusselt numbers in Figure 4.6(a) depend on η, suggesting that only this radial flow partitioning introduces the strong curvature dependence of the torques. In conclusion, the impact of the system rotation (parametrised by R_Ω) on the turbulent momentum transport becomes independent of η if the flow is not partly stabilised by counter-rotating the outer cylinder or if this curvature effect becomes negligible for large radius ratios.

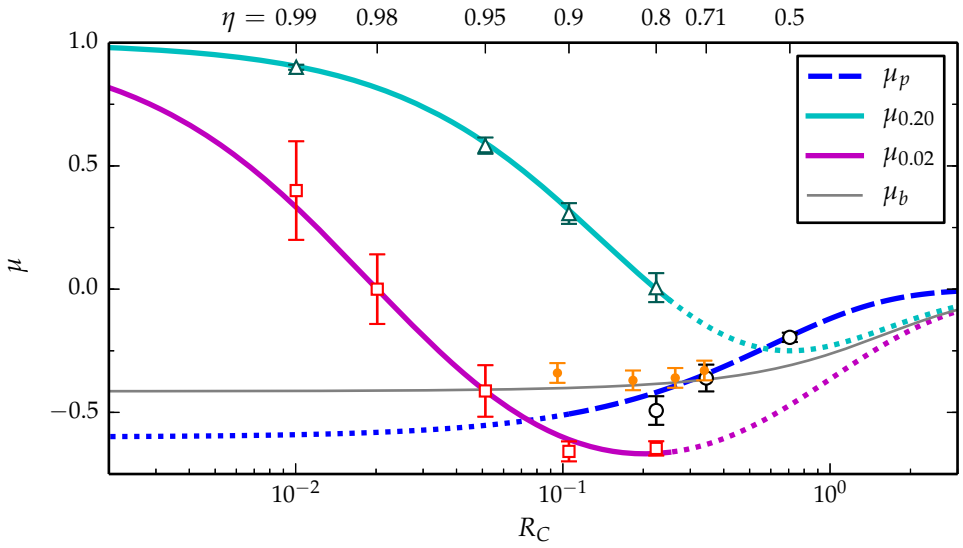

FIGURE 4.7: Location $\mu_{\max}$ of the torque maxima as a function of the curvature number $R_C = (1-\eta)/\sqrt{\eta}$. The open circles, triangles and squares summarise our numerical results for the detachment, broad and narrow maximum, respectively, at $Re_S = 2 \times 10^4$ from Figure 4.6. The maximum locations $\mu_{\max}$ were calculated from quadratic fits to the peaks in $Nu_\omega(\mu)$, except for the narrow maximum for $\eta \geq 0.95$, which is not well approximated by a parabola and therefore determined by the location of the largest data point. The small circles indicate the experimental results by Ostilla-Mónico *et al.* (2014a) for $Re_S \sim 10^5$ to 10^6. These are complemented by the prediction $\mu_p(\eta)$ from equation (3.10) (Brauckmann & Eckhardt, 2013b) and by the angle bisector $\mu_b(\eta)$, equation (3.6), by van Gils *et al.* (2012). In addition, two $\mu(\eta)$-lines for constant rotation number $R_\Omega = 0.2$ and $R_\Omega = 0.02$ are shown, corresponding to the broad and narrow torque maxima.

location of torque maxima

The position of the torque maxima for $Re_S = 2 \times 10^4$ and $\eta \geq 0.9$, which in R_Ω is given by constant rotation numbers $R_\Omega = 0.2$ and $R_\Omega = 0.02$, translates into η-dependent rotation ratios μ, which are represented by the thick solid lines in Figure 4.7. The torque maximum locations $\mu_{\max}$ from the DNS (triangles and squares) closely follow these lines for $\eta \geq 0.9$. In particular, this reveals that for $\eta = 0.99$ both the broad and the narrow torque maximum occur for co-rotating cylinders, i.e. for $\mu > 0$. Therefore, the narrow maximum cannot be related to the detachment mechanism described in Chapter 3 that causes the torque maximum at counter-rotation for $\eta = 0.5$ and 0.71. For the latter radius ratios, the maximum location $\mu_{\max}$ agrees with the predictive line $\mu_p(\eta)$ in Figure 4.7. Finally, the intermediate radius ratio $\eta = 0.8$ shows indications of all three torque maxima close to the lines in Figure 4.7, with the detachment and the narrow maximum lying close together and being not as pronounced as the broad maximum, cf. Figure 4.6.

In addition, Figure 4.7 shows the torque maxima identified for various radius ratios in experiments at much higher Reynolds numbers (Ostilla-Mónico *et al.*, 2014a). While the maximum positions $\mu_{\max}$ for $\eta = 0.714$, 0.769 and 0.833 conform with the trend of the detachment maximum, the one for $\eta = 0.909$ clearly deviates from both μ_p and our simulations; this

will be discussed in detail at the end of this section. Moreover, the angle bisector line $\mu_b(\eta)$, which was suggested by van Gils *et al.* (2012) for the position of the maximum $\mu_{\max}$, lies close to the experimental torque maxima. However, $\mu_b(\eta)$ clearly deviates from the torque maximum for $\eta = 0.5$ (Merbold, Brauckmann & Egbers, 2013) and differs in its functional behaviour for $\eta \to 1$ from our DNS results.

rotation dependence for higher Re_S

For the range of shear Reynolds numbers $Re_S \sim 10^4$ investigated here, the rotation dependence of the torque significantly changes with increasing Re_S, cf. Figure 4.5. It is likely that this transformation process continues beyond $Re_S = 2 \times 10^4$. However, concerning the detachment torque maximum for $\eta = 0.5$ and 0.71 it was shown that, after an initial transformation with increasing shear, the rotation dependence of the simulated torques at $Re_S = 2 \times 10^4$ already compares well to experimental torque measurements at much higher $Re_S \sim 10^5$ to 10^6 (Brauckmann & Eckhardt, 2013a; Merbold, Brauckmann & Egbers, 2013). On the other hand, concerning the two torque maxima in low-curvature TCF ($\eta \gtrsim 0.9$), Ostilla-Mónico *et al.* (2014a) find in their torque measurements for $\eta = 0.833$ and 0.909 that the power-law exponent γ of the torque scaling $Nu_\omega \sim {Re_S}^\gamma$ depends on the system rotation for Re_S below a few 10^5, which indicates that the transformation of the rotation dependence still continues up to $Re_S \sim 10^5$. As regards the second narrow torque maximum, we expect that it grows further in relation to the broad maximum for $Re_S > 2 \times 10^4$ and that this may shift the torque-maximising rotation number slightly.

The torque maximum from the experiment at $\eta = 0.909$ and Re_S above 10^5 (Ostilla-Mónico *et al.*, 2014a) supports this assumption, as shown in the inset of Figure 4.6(a) which compares experiment and DNS: The experimental torque-maximising rotation ratio $\mu_{\max} = -0.34$ corresponds to $R_\Omega = 0.04$ which only slightly deviates from $R_\Omega = 0.02$ for the narrow maximum at lower $Re_S = 2 \times 10^4$. In conclusion, apart from small changes with Re_S, our simulations already capture the beginning of the general turbulent behaviour at much higher shear rates.

4.4 MOMENTUM TRANSPORT DUE TO VORTICAL MOTION

In this and the following sections, we investigate the momentum transport characteristics that underlie the rotation dependence of the Nusselt number discussed above. Vortical motions, such as Taylor vortices and their turbulent remnants, are known to effectively contribute to this transport by moving fast fluid from the inner cylinder outwards and slow outer fluid inwards. Their effects on the turbulence have been discussed previously (Lathrop, Fineberg & Swinney, 1992a; Lewis & Swinney, 1999; Martínez-Arias *et al.*, 2014). Brauckmann & Eckhardt (2013b) quantified the link of the vortical motion to the torque and found that the torque contribution of the mean vortical motion was largest near the torque maximum, see Section 3.4. Flow visualisations of DNS by Salewski & Eckhardt (2015) show distinct vortical states which underlie the narrow and broad maxima for

RPCF. Furthermore, using experiments at $Re_S \sim 10^6$ (Huisman *et al.*, 2014) and DNS at $Re_S \sim 10^5$ (Ostilla-Mónico *et al.*, 2014c), these structures have been detected over a range of rotation numbers where their presence is associated with a single torque maximum.

To investigate the effects of vortical structures on the torque, we first extract the mean vortical motion underlying the turbulence in the full simulation and measure its contribution to the momentum transport. The mean vortices consist of temporally and streamwise-averaged turbulent Taylor vortices and are analogous to the large-scale circulation found in turbulent Rayleigh–Bénard convection (Ahlers, Grossmann & Lohse, 2009). Next, since Taylor vortices do not depend on the streamwise direction, we also consider the torque which results from streamwise-independent flow. We then summarise our results in Figure 4.8.

4.4.1 *Mean vortical motion*

We follow the procedure introduced in Section 3.4 (Brauckmann & Eckhardt, 2013b) and decompose the flow of the full DNS into a mean contribution $\overline{\boldsymbol{u}} = \langle \boldsymbol{u} \rangle_{\varphi,t}$ (or $\overline{\boldsymbol{u}} = \langle \boldsymbol{u} \rangle_{x,t}$ for RPCF) that includes the mean vortical motion in the rz-plane (yz-plane) and into the turbulent fluctuations around these mean vortices $\boldsymbol{u}'' = \boldsymbol{u} - \overline{\boldsymbol{u}}$, similar to the triple decomposition by Reynolds & Hussain (1972). As explained in Section 3.4, this velocity decomposition applied to the angular-momentum flux (4.11) results in a separation of the torque into a contribution that is caused by the mean vortical motion $\overline{G}$ and a second contribution that is due to turbulent fluctuations G'', i.e. $G = \overline{G} + G''$ with

contributions to the torque

$$\begin{aligned} \overline{G} &= \frac{Re_S^2}{r_2 - r_1} \int_{r_1}^{r_2} \left(\langle \overline{u}_r \overline{\mathcal{L}} \rangle - Re_S^{-1} r^2 \partial_r \langle \overline{\omega} \rangle \right) r \, \mathrm{d}r, \\ G'' &= \frac{Re_S^2}{r_2 - r_1} \int_{r_1}^{r_2} \langle u_r'' \mathcal{L}'' \rangle \, r \, \mathrm{d}r. \end{aligned} \tag{4.18}$$

Analogous expressions for the decomposition of the driving force into $F = \overline{F} + F''$ can be obtained for RPCF by substituting the velocity decomposition into the momentum flux equation (4.14). As explained in Section 3.4, during the temporal average, we correct a potential spanwise drift of the turbulent Taylor vortices in order to represent their correct amplitude in the mean flow $\overline{\boldsymbol{u}}$. Such a drift would lead to a cancellation of the large-scale motion over time, even though it might be strong. In contrast to the r-independent total current J^ω, the individual terms in (4.18) vary with the radius. Therefore, we introduced the additional radial average in (4.18) in order to quantify the typical strength of the torque contributions. Since we are interested in the mean vortical motion, which dominates in the central region and not in the BLs, we restrict this average to the range between $(r_1 - r_i)/d = 1/4$ and $(r_2 - r_i)/d = 3/4$.

narrow peak in $\overline{G}$ for large η

In Figure 4.8, the torque due to the mean vortical motion $\overline{G}$ is compared to the total torque G. For all cases, $\overline{G}$ exhibits a maximum. For $\eta \geq 0.8$ and

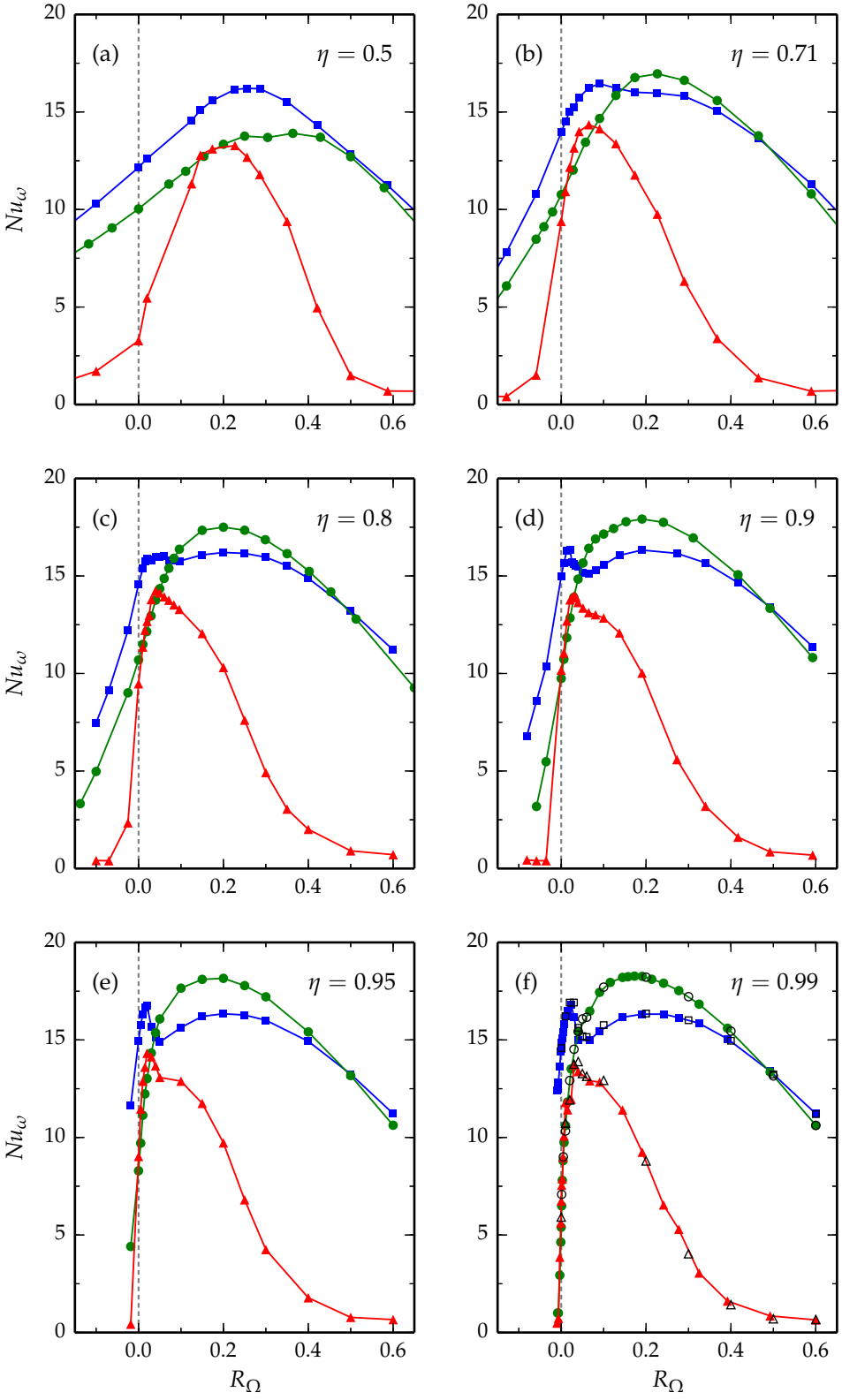

FIGURE 4.8: Comparison of the total torque G (■) to the torque that results from the streamwise-invariant flow G_{2D} (●) and to the torque due to the mean vortical motion $\overline{G}$ (▲) for $Re_S = 2 \times 10^4$. All torques are measured in units of the laminar torque G_{lam} giving Nusselt numbers Nu_ω. The open symbols in (f) show corresponding results from RPCF simulations.

RPCF, the maximum of $\overline{G}$, where the momentum transport by the mean vortices is most effective, nearly coincides with the narrow maximum of the total torque G. Moreover, it is apparent that a distinct narrow peak also occurs in mean-vortex torque $\overline{G}$ for large η. This suggests that the narrow, high-Re_S maximum is linked to efficient mean vortices. For lower radius ratios, i.e. $\eta = 0.5$ and 0.71, the coincidence between the maxima in $\overline{G}$ and G is not as significant; nevertheless, as the analysis in Section 3.4 and Brauckmann & Eckhardt (2013b) demonstrates, this coincidence does exist for $\eta = 0.5$ and 0.71 when the radial average in (4.18) covers the complete radial gap instead of the central region. Finally, the mean-vortex torques $\overline{G}$ in Figure 4.8 reveal that the mean Taylor vortices occur and grow in strength for $R_\Omega > 0$ as previously observed in the experiment by Ravelet, Delfos & Westerweel (2010).

4.4.2 *Importance of streamwise-invariant structures*

We perform simulations that force the flow to be invariant in the downstream direction by taking no Fourier mode in the φ-direction (x-direction for RPCF). For TCF this corresponds to axisymmetric simulations. Note that this procedure differs from two-dimensional simulations in a cross-section because three velocity components are still active, but only spatial variations in two directions (wall-normal and spanwise) are allowed. Since the Reynolds numbers are well above the linear instability of TCF and RPCF, even the axisymmetric flow is chaotic and typically comprises one vortex pair. These simulations of streamwise-invariant vortical flow result in torques, denoted as G_{2D}, that we compare to the total torques G in Figure 4.8. The torque G_{2D} also shows a broad maximum, which has an η-dependent shift in its location: for $\eta \sim 1$, the maximum is at $R_\Omega = 0.18$; and for $\eta = 0.5$, it is near $R_\Omega = 0.35$. For some radius ratios, namely $\eta = 0.8$, $\eta = 0.9$, this places the G_{2D}-maximum at nearly the same R_Ω as the broad maximum in the total torque; however, the streamwise-invariant simulations overestimate the amplitude of the maximum. In fact, for $\eta \geq 0.8$ and RPCF, the G_{2D}-maximum resembles the broad maximum in the total torque. Furthermore, it also appears to agree with the plateau that occurs in the total torque beside the actual torque maximum for $\eta = 0.71$ (Figure 4.8(b)). This suggests that the plateau for $Re_S = 2 \times 10^4$, as well as the broad maximum at lower Re_S (cf. Figure 4.5(b)), follow from the same mechanism that causes the broad maximum for $\eta \geq 0.8$.

broad maximum also in G_{2D}

The analysis reveals several features of the contribution of vortical motion to the torque for different degrees of curvature. The streamwise-averaged mean flow ($\overline{G}$) appears to reproduce the narrow torque maximum, but this is not reflected by the streamwise-invariant flow (G_{2D}). This seems to be counterintuitive when considering that $\overline{\boldsymbol{u}}$ is streamwise invariant like the simulations underlying G_{2D}, but neither the detachment maximum in the total torque for $\eta \leq 0.8$ nor the narrow maximum for $\eta \geq 0.8$ occur in the torques from the streamwise-invariant simulations.

As a consequence, these maxima must arise from more complicated flows which allow for streamwise fluctuations and cause an additional increase of the momentum transport. The reasons for the strong momentum transport differ between the broad and narrow torque maximum, as will be discussed in Section 4.5.3 and Chapter 5.

4.5 FLOW CHARACTERISATION

In Section 4.3 we discussed that the momentum transport converges to a universal behaviour for the low-curvature TCF ($\eta \geq 0.9$), in that the rotation dependence becomes independent of η. Furthermore, the dependence on R_Ω agrees with that observed in RPCF. In the following, we analyse how the convergence for $\eta \geq 0.9$ to RPCF extends to other flow characteristics such as mean profiles and turbulent fluctuations.

4.5.1 *Angular momentum profiles*

collapse of angular momentum profiles

Here, we analyse the mean profiles of the specific angular momentum $\hat{\mathcal{L}} = r\hat{u}_\varphi$ in the inertial frame, which is radially transported between the cylinders. To compensate for the varying mean system rotation, we show rescaled profiles $\widetilde{\mathcal{L}} = \left(\langle\hat{\mathcal{L}}\rangle - \mathcal{L}_o\right)/(\mathcal{L}_i - \mathcal{L}_o)$ in Figure 4.9 where $\mathcal{L}_i$ and $\mathcal{L}_o$ denote the specific angular momentum of the inner and outer cylinder. As a result, the profiles for various radius ratios η at the same rotation number R_Ω collapse as long as the flow is not subject to the radial partitioning of stability for moderate counter-rotation (cf. Section 3.1): The rotation number $R_\Omega = 0.5$ corresponds to co-rotation ($\mu \geq 0$) for all investigated η, and all profiles of $\widetilde{\mathcal{L}}$ in Figure 4.9(d) collapse well. However at $R_\Omega = 0.2$, only the simulation for $\eta = 0.5$ with $\mu = -0.22$ shows the bursting in the outer region and a deviating profile in Figure 4.9(c). Similarly, at $R_\Omega = 0.02$ (Figure 4.9(b)), the profiles for $\eta \leq 0.9$ with μ values in the bursting regime clearly deviate from the profiles for $\eta = 0.95$ and 0.99 with $\mu > \mu_p$ which are closer together. Finally, no collapse is observed for $R_\Omega = 0$ which always corresponds to exact counter-rotation. In addition, Figure 4.9 shows u_x profiles from RPCF with the rotation-induced gradient subtracted, i.e. $\langle u_x\rangle - R_\Omega y$, which agree well with the collapsed $\widetilde{\mathcal{L}}$ profiles from TCF when rescaled to the same interval. The reason for this correspondence between $\langle u_x\rangle - R_\Omega y$ in RPCF and the angular momentum profiles in TCF will be discussed in the next section.

flattening of angular momentum profiles

The $\widetilde{\mathcal{L}}$ profiles tend toward a universal shape for increasing R_Ω, as the radial partitioning of stability disappears. The specific angular momentum in the centre becomes nearly flat (with a slightly positive slope) and approaches $\widetilde{\mathcal{L}} = 0.5$ which corresponds to $\langle\hat{\mathcal{L}}\rangle = (\mathcal{L}_i + \mathcal{L}_o)/2$ and indicates that the angular momentum is well mixed. Already Wendt (1933) noted that in the unstable regime the angular momentum becomes almost constant in the centre which was also repeatedly observed for the case of a stationary outer cylinder (Wattendorf, 1935; Taylor, 1935; Smith & Town-

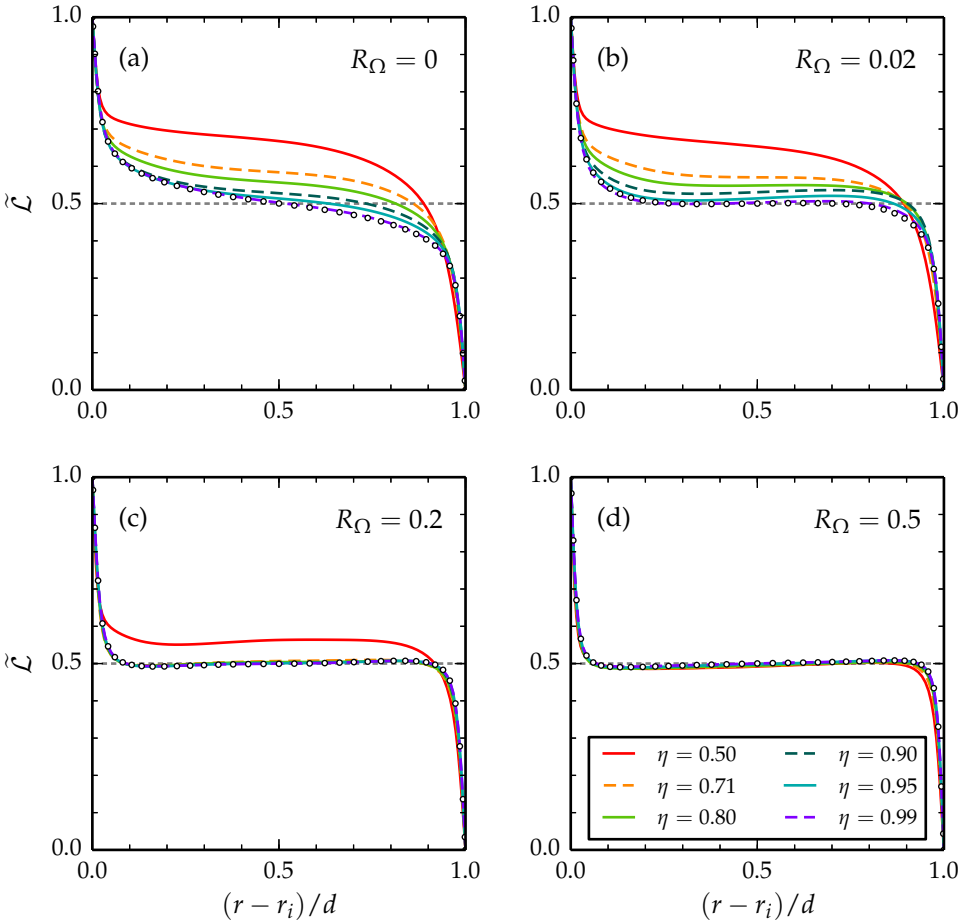

FIGURE 4.9: Profiles of the rescaled specific angular momentum in the inertial frame $\widetilde{\mathcal{L}} = (\langle\hat{\mathcal{L}}\rangle - \mathcal{L}_o)/(\mathcal{L}_i - \mathcal{L}_o)$ for $Re_S = 2 \times 10^4$, the rotation numbers R_Ω specified in the figures and six different radius ratios. The corresponding RPCF profile $\langle u_x\rangle - R_\Omega y$ rescaled to the interval $[0, 1]$ is shown by the dots. Each figure contains profiles for $\eta = 0.5$, 0.71, 0.8, 0.9, 0.95 and 0.99 as listed in (d). Some of the profiles collapse, especially in (c) and (d). In (a) and (b) the profile centre level decreases monotonically with increasing $\eta \to 1$. The dotted line shows the arithmetic mean angular momentum $\widetilde{\mathcal{L}} = 0.5$.

send, 1982; Lewis & Swinney, 1999; Dong, 2007). Note that the angular momentum profile becomes flat in the inertial frame but not in the rotating frame. Flat $\hat{\mathcal{L}}$ profiles resemble the situation in Rayleigh–Bénard convection where the transport of heat results in a well-mixed temperature in the bulk (Tilgner, Belmonte & Libchaber, 1993; Kerr, 1996; Brown & Ahlers, 2007; Ahlers *et al.*, 2012).

4.5.2 *Mixing of angular momentum and neutral stability*

The observation that the specific angular momentum $\hat{\mathcal{L}} = r\hat{u}_\varphi$ becomes almost flat in the centre is remarkable and calls for an explanation. Moreover, it is of interest whether an analogous phenomenon can be found in RPCF. To address both questions, we will study the stability properties of the

mean profile around which the turbulence fluctuates. As long as the mean profile ($\langle\omega\rangle(r)$ in TCF and $\langle u_x\rangle(y)$ in RPCF) is unstable due to a strong a gradient in the centre, it further enforces turbulence which increases the mixing of angular (or linear) momentum; the mixing flattens and therefore re-stabilises the profile. However, a stable, low-gradient profile decreases turbulent mixing, so that the profile becomes steeper and eventually unstable again. Therefore, we assume that both processes balance in the statistically averaged sense and the mean turbulent profile becomes neutrally stable in the centre.

For TCF with stationary outer cylinder, Wattendorf (1935) and Taylor (1935) already noted that the mean angular momentum profile in the middle tends towards one of neutral stability according to Rayleigh's inviscid criterion (Rayleigh, 1917), which predicts a constant angular momentum profile for this case. Neglecting viscous effects in the central part of the flow becomes justifiable at high Reynolds numbers. The flat $\widetilde{\mathcal{L}}$ profiles in Figure 4.9 indeed realise Rayleigh's neutral stability criterion in the centre, thus, supporting the aforementioned assumptions. More precisely, in the inertial frame, Rayleigh's discriminant for neutral stability (Chandrasekhar, 1961) reads

inviscid neutral stability for TCF

$$0 \equiv \frac{2\langle\hat{\omega}\rangle}{r}\,\partial_r\big(r^2\langle\hat{\omega}\rangle\big) = \left(R_\Omega - 1 + \frac{\widetilde{r}^2}{r^2}\right)\frac{1}{r}\partial_r\langle\hat{\mathcal{L}}\rangle \tag{4.19}$$

$$= \left(R_\Omega - 1 + \frac{\widetilde{r}^2}{r^2}\right)\left(R_\Omega - 1 + \frac{\widetilde{r}^2}{r^2} + r\partial_r\langle\omega\rangle\right), \tag{4.20}$$

here expressed so that it serves as a condition for a neutrally stable turbulent mean profile in either $\hat{\mathcal{L}}$ or ω in the middle. For that purpose, we used the relation $\partial_r\hat{\omega} = \partial_r\omega$ and substituted the mean profile $\langle\hat{\omega}\rangle$ by the laminar solution $\hat{\omega}_{\mathrm{lam}}(r)$ from equation (1.10) because in the centre $\hat{\omega}_{\mathrm{lam}}$ provides a reasonable approximation to the magnitude of the turbulent mean profile as evidenced by the comparison in Brauckmann & Eckhardt (2013a). Since in the middle r is close to the geometric radius $\widetilde{r} = \sqrt{r_i r_o}/d$, equation (4.20) implies that $r\partial_r\langle\omega\rangle \approx -R_\Omega$ for $R_\Omega \neq 0$. Ostilla *et al.* (2013) obtained a similar linear relationship by assuming that the Coriolis force term balances the convective term in the φ-component of the equations of motion (4.5). Equations (4.19) and (4.20) then show that both force balance (Ostilla *et al.*, 2013) and inviscid stability (Rayleigh, 1917) predict a profile with flat angular momentum.

The equivalent stability formulation in RPCF was derived from an analogy between rotating shear flows and buoyant flows (Bradshaw, 1969; Tritton, 1992): The stability expressed by a quantity similar to the Richardson number in stratified flows results in the neutral stability condition

inviscid neutral stability for RPCF

$$R_\Omega\big(R_\Omega - \partial_y\langle u_x\rangle\big) \equiv 0, \tag{4.21}$$

which is approximately contained in (4.20) since $\widetilde{r}/r \approx 1$ in the middle, and $r\partial_r\langle\omega\rangle$ corresponds to $-\partial_y\langle u_x\rangle$. The difference in sign originates from the fact that the radial coordinate in TCF is antiparallel to the wall-normal

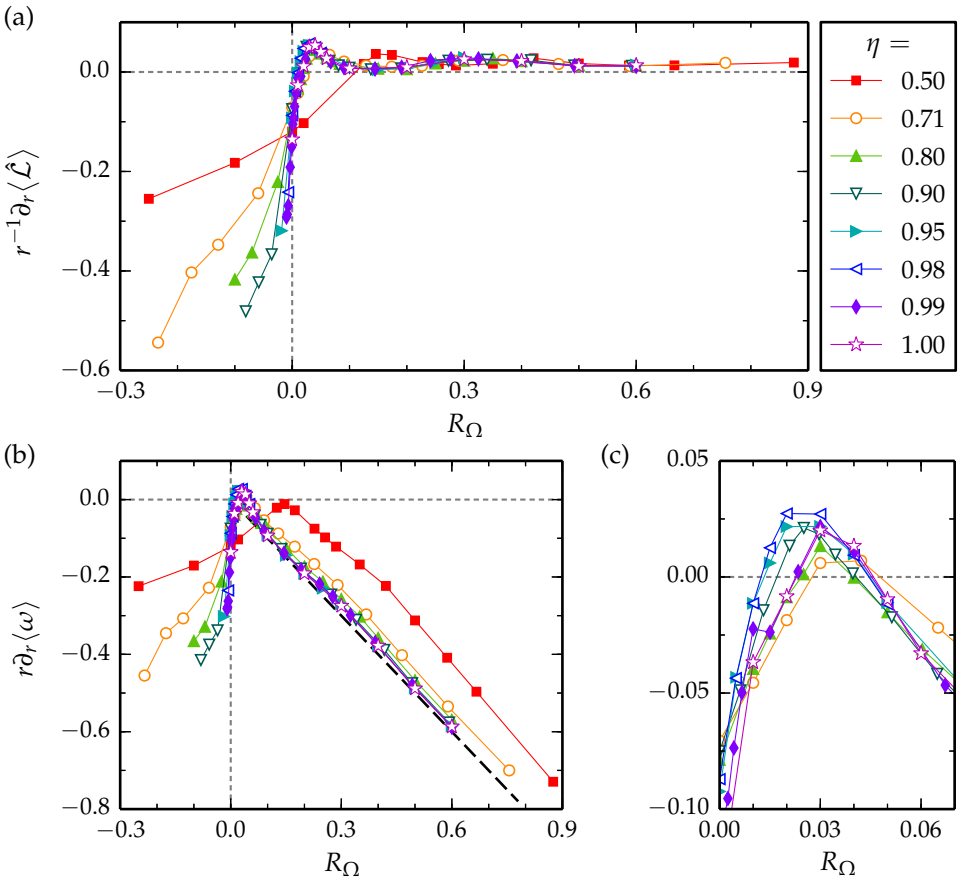

FIGURE 4.10: Profile gradients in the middle region versus the rotation number R_Ω for $Re_S = 2 \times 10^4$ and various radius ratios η. (a) Radial gradient of the (inertial-frame) angular momentum profile $\langle\hat{\mathcal{L}}\rangle$ in TCF and the corresponding quantity $(R_\Omega - \partial_y\langle u_x\rangle)$ in RPCF, (b) gradient of the angular velocity profile $\langle\omega\rangle$ in TCF and the negative downstream velocity gradient $-\partial_y\langle u_x\rangle$ in RPCF, (c) detail of the maximum in (b). The black dashed line in (b) indicates the estimate $r\partial_r\langle\omega\rangle = -\partial_y\langle u_x\rangle = -R_\Omega$ from the neutral stability conditions (4.20) and (4.21). All gradients are calculated by averaging the compensated profile derivative $r^{-1}\partial_r\langle\hat{\mathcal{L}}\rangle$ or $r\partial_r\langle\omega\rangle$ over the central region $(r - r_i)/d \in [0.4, 0.6]$.

coordinate in RPCF, cf. Figure 4.1. For RPCF we also assume that the turbulent mean profile in the middle becomes neutrally stable and fulfils (4.21), as proposed previously by Suryadi, Segalini & Alfredsson (2014). In conclusion, the negative profile slope $-\partial_y\langle u_x\rangle$ in RPCF corresponds to the angular velocity gradient $r\partial_r\langle\omega\rangle$ in TCF. Moreover, comparing (4.21) to (4.19) reveals that the combination $(R_\Omega - \partial_y\langle u_x\rangle)$ in RPCF plays the role of the angular momentum gradient $r^{-1}\partial_r\langle\hat{\mathcal{L}}\rangle$ in TCF, and we therefore compare the modified RPCF profile $\langle u_x\rangle - R_\Omega y$ to the angular momentum profiles in Figure 4.9.

profile gradients in the central region

To test the assumption of neutrally stable mean profiles, the dependence of the profile gradients on R_Ω and the proposed analogies between TCF and RPCF, we evaluate the relevant profile gradients in the central region for $Re_S = 2 \times 10^4$ and various radius ratios. Figure 4.10(a) shows that

the specific angular momentum becomes almost flat with a slightly positive slope for $R_\Omega \gtrsim 0.02$, except for $\eta = 0.5$ where $\hat{\mathcal{L}}$ is well mixed only for $R_\Omega \gtrsim 0.1$. Experiments show that the slightly positive angular momentum slope persists for much higher Re_S (Smith & Townsend, 1982; Lewis & Swinney, 1999). In addition, for most $R_\Omega > 0$, the profile slopes measured by $r^{-1}\partial_r\langle\hat{\mathcal{L}}\rangle$ collapse for different η, which demonstrates the universality of the weak R_Ω-dependence. Furthermore, the quantity $(R_\Omega - \partial_y\langle u_x\rangle)$ from RPCF also shows this high level of agreement expected from the neutral stability analogy (4.19) and (4.21). In contrast, the profile gradients for $R_\Omega < 0$ ($R_\Omega < 0.1$ for $\eta = 0.5$) clearly vary with the radius ratio. For these rotation numbers, a pronounced stable region exists which introduces a strong curvature dependence as discussed for the torques in Section 4.3.

The flattening of the specific angular momentum implies that the angular velocity gradients depend on R_Ω, as shown in Figure 4.10(b,c) and in similar figures in Ostilla-Mónico *et al.* (2014a). In the unstable regime with $R_\Omega > 0$, the profile slopes $r\partial_r\langle\omega\rangle$ approach the neutral stability estimate $r\partial_r\langle\omega\rangle = -\partial_y\langle u_x\rangle = -R_\Omega$ as η tends to 1. Moreover for low-curvature TCF ($\eta \gtrsim 0.9$), they coincide with the u_x-profile gradients in RPCF which supports the proposed analogy between $\langle\omega\rangle$ and $\langle u_x\rangle$. The approximate scaling $\partial_y\langle u_x\rangle \sim R_\Omega$ in RPCF conforms with observations by Bech & Andersson (1997) and Suryadi, Segalini & Alfredsson (2014). However for smaller η, the $\langle\omega\rangle$ gradients depend more strongly on the curvature than the $\langle\hat{\mathcal{L}}\rangle$ gradients, consistent with the additional radial dependence in condition (4.20). Furthermore, we note that a slight local super-rotation (corresponding to a shear-inversion in RPCF) occurs in the central region for $R_\Omega \approx 0.03$ as detailed in Figure 4.10(c). This inversion may result from an efficient momentum transport by the large-scale vortices moving fast fluid from the inner wall outwards and slow fluid inwards. The maximum in the mean vortex torque $\overline{G}$ around $R_\Omega \approx 0.03$ indeed supports this picture, cf. Figure 4.8.

flattest ω profile near narrow torque maximum

For the low-curvature TCF with $\eta \gtrsim 0.9$, the flattest ω profile (i.e. maximum in $r\partial_r\langle\omega\rangle$) and the narrow torque maximum occur for almost the same rotation number ($R_\Omega \approx 0.03$ versus 0.02) which extends an observation in Ostilla-Mónico *et al.* (2014a) for $\eta \leq 0.909$ to larger radius ratios and to the limiting case of RPCF, where the flattest u_x profile is linked to the narrow maximum in Nu_u. This connection also exists for $\eta = 0.8$, thus, supporting the independence of the narrow maximum at $R_\Omega = 0.02$ from the detachment maximum at $R_\Omega = 0.05$. For $\eta = 0.5$ and $\eta = 0.71$ the R_Ω value of the flattest angular velocity profile does not coincide with the location of the torque maximum, which is another evidence that this detachment maximum differs from the narrow torque maximum observed for $\eta \gtrsim 0.9$. In contrast, Ostilla-Mónico *et al.* (2014a) found the flattest ω profile for $\eta = 0.5$ at $R_\Omega = 0.25$ and for $\eta = 0.714$ at $R_\Omega = 0.12$ which agree with the corresponding torque-maximising rotation numbers. However, the difference might result from the fact that their values are ex-

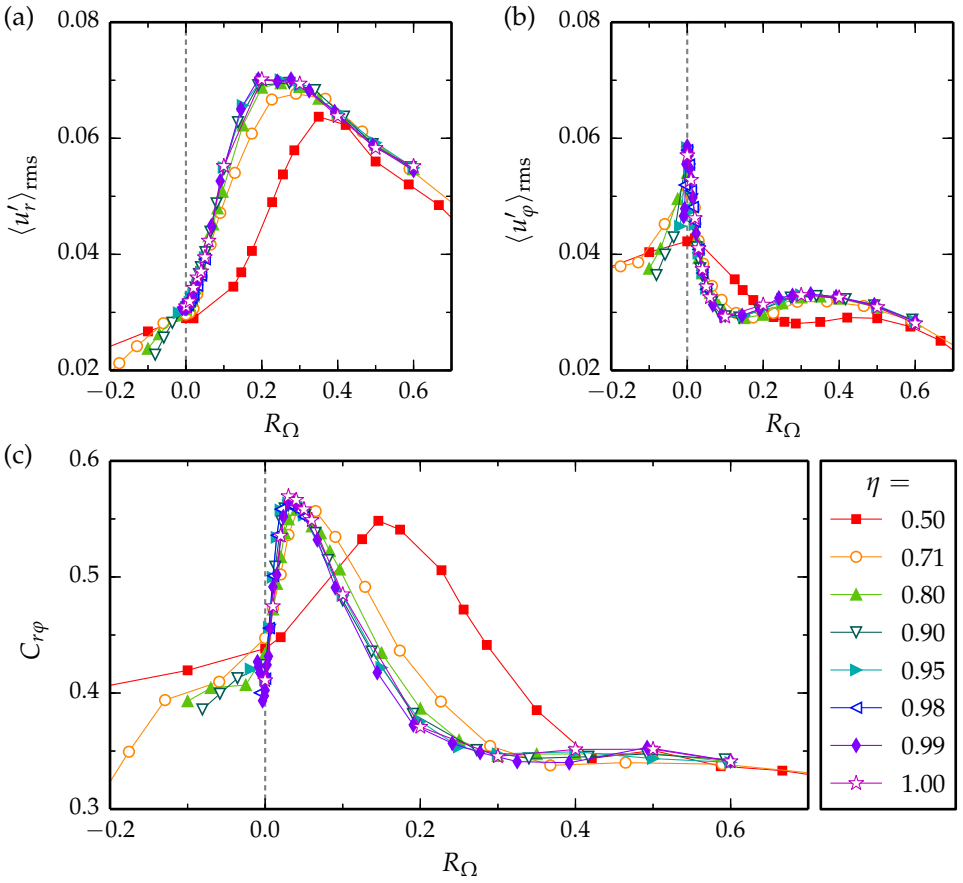

FIGURE 4.11: Fluctuation amplitude of the wall-normal velocity $\langle u_r' \rangle_{\mathrm{rms}}$ ($\langle u_y' \rangle_{\mathrm{rms}}$ for RPCF) in (a) and of the streamwise velocity $\langle u_\varphi' \rangle_{\mathrm{rms}}$ ($\langle u_x' \rangle_{\mathrm{rms}}$) in (b) and their cross-correlation coefficient $C_{r\varphi}$ (C_{yx}) in (c) as a function of the rotation number R_Ω for $Re_S = 2 \times 10^4$ and various radius ratios η. All quantities are radially average in the central region $(r - r_i)/d \in [1/3, 2/3]$ where momentum is mainly transported by the convective current $J_c^{\mathcal{L}} = r\langle u_r' u_\varphi' \rangle$ ($J_c^u = \langle u_y' u_x' \rangle$).

trapolated from simulations at $Re_S \lesssim 5 \times 10^3$ lower than the $Re_S = 2 \times 10^4$ used here.

The gradients of the ω profile (u_x profile in RPCF) are relevant when analysing the momentum transport in the centre and the torque (force) needed to drive the walls. They measure the diffusive part of the current $J^{\mathcal{L}}$ (J^u, respectively) which is mediated by viscosity, i.e. the last term in equations (4.11) and (4.14). A flat profile means that the convective current $J_c^{\mathcal{L}} = \langle u_r \mathcal{L} \rangle$ ($J_c^u = \langle u_y u_x \rangle$ in RPCF) accomplishes all momentum transport in the middle.

4.5.3 *Turbulent fluctuations*

Finally, we study the effect of the mean system rotation (R_Ω) on the characteristics of the convective momentum transport by turbulent fluctuations. We demonstrate that not all deviations from the laminar state contribute to the net convective momentum transport but only the turbulent fluctu-

ations around the mean profile. This becomes apparent when introducing the velocity deviation from the mean profile $\boldsymbol{u}' = \boldsymbol{u} - \langle \boldsymbol{u} \rangle$ by using the original average $\langle \cdots \rangle = \langle \cdots \rangle_{\varphi z,t}$; note that this differs from $\boldsymbol{u}'' = \boldsymbol{u} - \langle \boldsymbol{u} \rangle_{\varphi,t}$, which was introduced in Section 4.4.1 to describe turbulent fluctuations around the mean vortical motion, see also Bilson & Bremhorst (2007). As a result of incompressibility (4.6) the mean radial flow vanishes, i.e. $\langle u_r \rangle = 0$, so that $u_r' = u_r$. Moreover, by substituting the azimuthal velocity decomposition $u_\varphi = \langle u_\varphi \rangle + u_\varphi'$ into the convective angular-momentum flux,

$$J_c^{\mathcal{L}} = r\langle u_r\, u_\varphi \rangle = r\langle u_r \rangle \langle u_\varphi \rangle + r\Big\langle u_r\, u_\varphi' \Big\rangle = r\Big\langle u_r'\, u_\varphi' \Big\rangle, \tag{4.22}$$

we see that only the correlated fluctuations u_r' and u_φ' contribute to the net convective transport. Inspired by the analysis of Burin, Schartman & Ji (2010), we measure their amplitude by area- and time-averaged RMS values $\langle u_r' \rangle_{\mathrm{rms}}$ and $\langle u_\varphi' \rangle_{\mathrm{rms}}$ that enable the definition of a cross-correlation coefficient

decomposition of the convective current

$$C_{r\varphi} = \frac{\Big\langle u_r'\, u_\varphi' \Big\rangle}{\langle u_r' \rangle_{\mathrm{rms}} \langle u_\varphi' \rangle_{\mathrm{rms}}} \qquad \text{so that} \qquad J_c^{\mathcal{L}} = r\, \langle u_r' \rangle_{\mathrm{rms}} \langle u_\varphi' \rangle_{\mathrm{rms}}\, C_{r\varphi}. \tag{4.23}$$

The corresponding quantities in RPCF are

$$C_{yx} = \frac{\Big\langle u_y'\, u_x' \Big\rangle}{\langle u_y' \rangle_{\mathrm{rms}} \langle u_x' \rangle_{\mathrm{rms}}} \qquad \text{so that} \qquad J_c^{u} = \langle u_y' \rangle_{\mathrm{rms}} \langle u_x' \rangle_{\mathrm{rms}}\, C_{yx}. \tag{4.24}$$

Consequently, we may consider increases in the convective (angular) momentum transport as being due to violent fluctuations of the wall-normal or streamwise velocities, or due to a strong cross-correlation between them. All three effects are analysed as functions of R_Ω for $Re_S = 2 \times 10^4$ in Figure 4.11.

broad maximum in wall-normal flow

Generally, we observe for $\eta \geq 0.8$ and RPCF that the fluctuation amplitudes and correlation coefficients collapse well in the unstable range with $R_\Omega \gtrsim 0$, which again indicates that low-curvature TCF and RPCF show the same rotation dependence. The wall-normal flow grows in amplitude when rotation sets in ($R_\Omega > 0$) and is suppressed by strong rotation forming a maximum around $R_\Omega \approx 0.25$ for $\eta \geq 0.71$; this nearly coincides with the broad torque maximum at $R_\Omega = 0.2$ for $\eta \geq 0.8$, and it resembles the maximum observed in the torque G_{2D} from streamwise-invariant simulations (cf. Figure 4.8). The co-occurrence of the maximum wall-normal flow with the broad peak supports the picture that the broad torque maximum is associated with strong vortical motion. While the co-occurrence holds for the plateau next to the actual maximum for $\eta = 0.71$ (Figure 4.5(b)), the correlation between the maxima is less clear for $\eta = 0.5$.

On the other hand, the streamwise velocity fluctuations are strongest without system rotation, forming a sharp maximum around $R_\Omega = 0$, except for the high-curvature TCF with $\eta = 0.5$ (Figure 4.11(b)). A corresponding peak in the torques is missing since the narrow torque maximum at $R_\Omega = 0.02$ clearly drops off towards $R_\Omega = 0$ (cf. Figure 4.6(b)).

efficient transport near narrow torque maximum

However, for $\eta \geq 0.9$ the maximum in the cross-correlation coefficients at $R_\Omega \approx 0.03$ (Figure 4.11(c)) comes closer to the narrow torque maximum suggesting that the latter is associated with a very efficient (angular) momentum transport by moderately strong but correlated vortices. Moreover, the peak in the cross-correlation coefficients coincides with the maximum in the torque $\overline{G}$ due to the mean vortical flow (cf. Figure 4.8). The maximum in $C_{r\varphi}$ at $R_\Omega = 0.15$ and at $R_\Omega = 0.05$ for $\eta = 0.5$ and $\eta = 0.71$, respectively, does not coincide with the torque maximum for the corresponding radius ratio indicating that the latter differs from the narrow maximum for $\eta \gtrsim 0.9$.

4.6 SUMMARY AND CONCLUSIONS

By describing TCF in the rotating reference frame, as proposed by Dubrulle *et al.* (2005), we were able to study its limit to RPCF as the radius ratio η approaches 1. In this framework, shear and mean system rotation are quantified by the same parameters Re_S and R_Ω in both systems and curvature effects measured by R_C disappear with $\eta \to 1$. The data collapse observed for $\eta \geq 0.9$ shows that Re_S and R_Ω are the appropriate parameters with which to describe the transition from TCF to RPCF. Moreover, we analysed the analogy between the angular momentum transport in TCF and the linear momentum transport in RPCF by utilising the correspondence between the currents $J^{\mathcal{L}}$ and J^u which are connected to the torque G and the force F in the respective geometries.

As a consequence of curvature, the TCF for counter-rotating cylinders features a radial partitioning of stability that results in enhanced intermittent fluctuations in the outer region. In Chapter 3, the occurrence of the intermittency with changing system rotation has been linked to the torque maximum that forms as a function of R_Ω for $\eta = 0.5$ and 0.71, see also van Gils *et al.* (2012) and Brauckmann & Eckhardt (2013b). Here, we demonstrated that the stability difference between the inner and outer region, and therefore the fluctuation asymmetry, decrease with declining curvature and eventually disappear as $\eta \to 1$. As a consequence, the detachment torque maximum also vanishes for $\eta \gtrsim 0.9$.

For this low-curvature TCF, we identified two new torque maxima, a broad one at $R_\Omega = 0.2$ that exists for all studied Re_S and a narrow one at $R_\Omega = 0.02$ that emerges as Re_S increases to 2×10^4. The broad torque maximum is accompanied by a strong vortical flow as evidenced by the large wall-normal velocity and can be reproduced in streamwise-invariant simulations, which also points to streamwise vortices causing a high angular momentum transport. On the other hand, the narrow torque maximum coincides with an effective mean flow where the angular momentum transport is maximised not due to large-amplitude vortices but because of correlated vortices, resulting in an effective convective transport. The momentum transport in RPCF features the same characteristics and also shows the two maxima.

Moreover, our simulations at $Re_S = 2 \times 10^4$ reveal that Nusselt numbers, profile slopes and fluctuation amplitudes collapse well for $\eta \geq 0.9$ when plotted as a function of R_Ω and agree with the corresponding quantities in RPCF. These results empirically demonstrate the convergence of TCF with small but finite curvature to RPCF. In this limit, the dependence on the system rotation parametrised by R_Ω becomes universal in both systems. In addition, the angular momentum profiles in TCF show this universal behaviour since they collapse remarkably well for different radius ratios $\eta \geq 0.5$ as long as no stabilised outer region occurs. Furthermore, we demonstrated that for unstable flow ($R_\Omega > 0$) the turbulent mean profiles in TCF and RPCF feature gradients in the centre that conform with neutral stability. Rayleigh's inviscid neutral stability criterion has an analogous counterpart in RPCF and implies that the profile slopes $r\partial_r\langle\omega\rangle$ and analogously $-\partial_y\langle u_x\rangle$ approximate $-R_\Omega$ in the central region. In the low-curvature TCF and in RPCF, the flattest ω profile (or u_x profile) and the narrow torque maximum appear at almost the same R_Ω value as also found for smaller $\eta \leq 0.909$ by Ostilla-Mónico *et al.* (2014a). However for $\eta = 0.909$, these authors observed only one maximum in the torque for Re_S above 10^5 which appears at $R_\Omega = 0.04$ close to our narrow maximum at $R_\Omega = 0.02$ and shows the same signature in the profile gradient. This fact, and the stronger growth of the narrow torque maximum with Re_S, suggest that it will outperform the broad maximum as the shear increases further. Further simulations or experiments for low-curvature flows with $\eta > 0.9$ and Re_S beyond 2×10^4 could provide welcome tests of this prediction.

The study of the transition from TCF to RPCF has revealed more changes in the flow structures and the turbulent characteristics than anticipated. Perhaps the most intriguing observation is the transition from a single maximum in torque to two maxima for $\eta \gtrsim 0.9$. We could here characterise the two maxima by their relation to prominent features of the turbulent flow and momentum transport. While this provides some insights into their origin, a better physical understanding of the maxima and an explanation for their remarkably universal position in R_Ω would be desirable.

5

STABLE AND TURBULENT BOUNDARY LAYERS

In shear flows, hydrodynamic instabilities drive vortical motions that transport momentum between the moving walls. Consequently, one of the walls experiences a momentum loss, which is balanced by the force driving the wall to keep the motion at a constant speed (Oertel, 2010). We here investigate this general connection between hydrodynamical instabilities and the resulting driving force (or torque) using the example of TCF, where we focus on the effect of the system rotation. The rotation is known to influence the stability of TCF (Taylor, 1923; Chandrasekhar, 1961; Esser & Grossmann, 1996; Dubrulle *et al.*, 2005) as well as the torque driving the cylinders, i.e. the rotational analogue of the driving force, which as a function of the system rotation shows a maximum. In Chapter 3, the torque maximum for $\eta = 0.5$ and 0.71 was rationalised by the occurrence of intermittent turbulent bursts for counter-rotating cylinders (van Gils *et al.*, 2012; Brauckmann & Eckhardt, 2013b). In the limit of vanishing curvature discussed in Chapter 4, the bursting behaviour as well as the corresponding maximum disappear, and two new torque maxima, a broad and a narrow one, emerge for $\eta \geq 0.9$. Moreover, we found that the mean angular momentum profiles have a universal shape as long as no stabilised outer region caused by counter-rotating cylinders occurs. Based on these observations, our aim is to predict the new rotation dependence of the torque for $\eta \geq 0.9$ by a simplified model, to understand the origin of the two torque maxima and to rationalise the mean profile shapes as well as their dependence on the system rotation.

In order to study these questions, we adopt the following explanatory picture: The mean rotation of the TC system causes a centrifugal instability that drives vortical flows. These vortices radially redistribute the angular momentum. As a result, the mean profile in the centre is flattened, which leads to higher angular velocity gradients in the BLs close to the cylinder walls. Consequently, the torque, which is proportional to the wall shear stress, rises above its laminar value. Altogether, this description clearly illustrates that instability mechanisms, mean velocity profiles and torques are closely connected. In this chapter, we utilise this connection to construct a model for the flow that describes the mean profiles and thereby predicts the torque. The model will be based on marginal stability arguments that have been applied to various flows including thermal convection (Malkus, 1954; Howard, 1966), channel flow (Malkus, 1956, 1983; Reynolds & Tiederman, 1967; Gol'dshtik, Sapozhnikov & Shtern, 1970) and TCF with stationary outer cylinder (King *et al.*, 1984; Marcus, 1984b; Barcilon & Brindley, 1984). As an extension of these TCF studies, we will

here present a model for the general case of independently rotating cylinders. Moreover, we will benchmark the model against our DNS results.

While the assumption of laminar BLs plays a central role in marginal stability models, in reality, BLs become turbulent for sufficiently high shear rates (Schlichting & Gersten, 2006). In TCF with $\eta \approx 0.7$ and stationary outer cylinder, the transition to turbulent BLs was indeed observed in experiments (Lathrop, Fineberg & Swinney, 1992a,b; Lewis & Swinney, 1999) and in numerical simulations (Ostilla-Mónico *et al.*, 2014b). Since turbulent BLs would invalidate one key assumption of the model, we will look for this transition in our numerical simulations.

It is important to note that in this chapter, we leave the rotating frame of reference and describe all results in the inertial frame since this facilitates the representation. For simplicity, we here omit the hat accent ($\hat{}$) used before and denote the velocity in the inertial frame by $\boldsymbol{u}$.

This chapter is organised as follows. In Section 5.1 we summarise the numerical results, i.e. the rotation dependence of the torque and the shape of angular momentum profiles, which we both aim to understand by the subsequent modelling in Section 5.2. After explaining the modelling approach in Section 5.2.1, we test to which extent the marginal stability assumptions of the model rationalise the rotation dependence of torque and profiles, by comparing model predictions to simulation results in Section 5.2.2. Discrepancies between model and numerical results point to a change in the BL dynamics that is analysed in Section 5.3. We conclude with a brief summary and further discussions.

5.1 NUMERICAL RESULTS

parameter range

First, we summarise the results that we aim to explain by the subsequent modelling. Our analysis here is based on TCF simulations at three shear rates $Re_S = 5 \times 10^3$, 10^4 and 2×10^4, realising various values of the rotation number in the range $-0.1 \leq R_\Omega \leq 0.95$. However, we focus on the results for $Re_S = 2 \times 10^4$ which show both torque maxima. Since we are interested in the turbulent behaviour of low-curvature TCF that appears for radius ratios $\eta \gtrsim 0.9$ (Chapter 4), we here investigate the two extreme cases $\eta = 0.9$ and $\eta = 0.99$. As before, we chose an axial domain height of $L_z = 2$, which suffices to represent one pair of counter-rotating Taylor vortices. Furthermore, the azimuthal length of the domain is reduced to $L_\varphi = 3.98$ and $L_\varphi = 6.31$ (with periodic boundary conditions) for $\eta = 0.9$ and $\eta = 0.99$, respectively.

5.1.1 *Rotation dependence of the torque*

In the simulations, we calculate the dimensionless torque per axial length, $G = T/(2\pi L_z \rho_f \nu^2 d)$, which is exerted on the cylinders. At the cylinder walls, it is proportional to the mean wall shear stress,

connection between torque and ω profile

$$G = -Re_S \, r_x^3 \partial_r \langle \omega \rangle|_{r_x} , \tag{5.1}$$

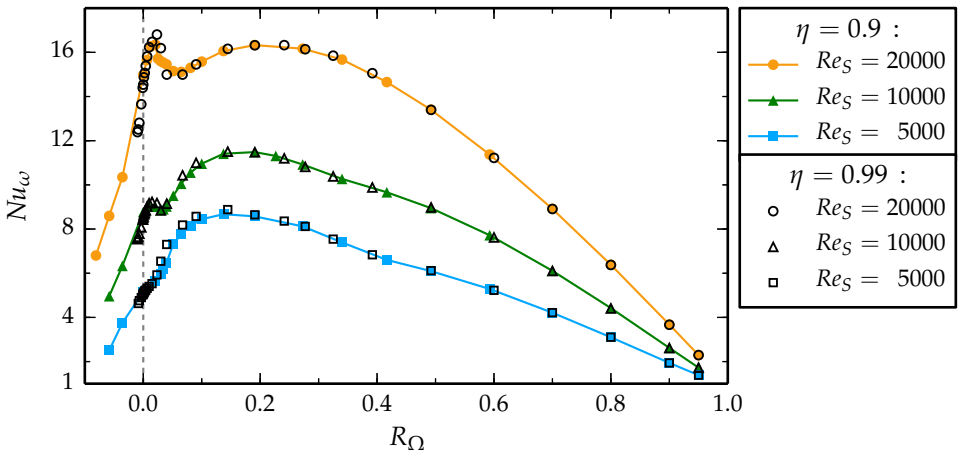

FIGURE 5.1: Variation of the torque (Nu_ω) with the system rotation parametrised by R_Ω for a constant shear Re_S. In addition to the broad maximum for $Re_S = 5000$, a second maximum at $R_\Omega = 0.02$ emerges with increasing shear. The torque shows the same R_Ω-dependence for both radius ratios $\eta = 0.9$ and $\eta = 0.99$.

and thereby connected to the mean angular velocity profile $\langle\omega\rangle$ at both cylinder radii $r_x = r_i$ and $r_x = r_o$. Our aim is to understand the variation of the torque with the system rotation (R_Ω), which is shown for $\eta = 0.9$ and 0.99 in Figure 5.1. The main features are the broad maximum at $R_\Omega \approx 0.2$ that exists for all three Re_S values and the narrow maximum at $R_\Omega = 0.02$ that only emerges with increasing shear. At $Re_S = 2 \times 10^4$, both torque maxima are of similar amplitude. For $\eta = 0.99$ both torque-maximising rotation numbers $R_\Omega = 0.2$ and $R_\Omega = 0.02$ correspond to co-rotating cylinders. Consequently, neither of the two maxima can be explained by the intermittent bursts for counter-rotating cylinders (van Gils *et al.*, 2012; Brauckmann & Eckhardt, 2013b) and, thus, they differ from the torque maximum found for $\eta < 0.9$. It is noteworthy that the R_Ω-dependence of the torque is universal for low-curvature TCF with $\eta \geq 0.9$ (cf. Section 4.3), as demonstrated again by the collapse of the torques for $\eta = 0.9$ and $\eta = 0.99$ in Figure 5.1. A similar collapse was also observed by Dubrulle *et al.* (2005) and Paoletti *et al.* (2012).

explanation for maxima needed

In conclusion, the two new torque maxima in low-curvature TCF both call for an explanation. Therefore, we seek to identify the physical mechanisms that are responsible for the formation of the broad and narrow torque maximum. As a step towards this goal, in Section 5.2 we will present a model of TCF which is based on a few assumptions about the effective turbulent behaviour. This will enable us to identify some key principles needed to rationalise the rotation-number dependence of the torque.

5.1.2 *Angular momentum profiles*

almost flat angular momentum profiles

Since our model will be based on the mean profile of the specific angular momentum $\mathcal{L} = ru_\varphi$ in the inertial frame, we first need some empirical knowledge of the profile shapes. Therefore, we calculate time-, azi-

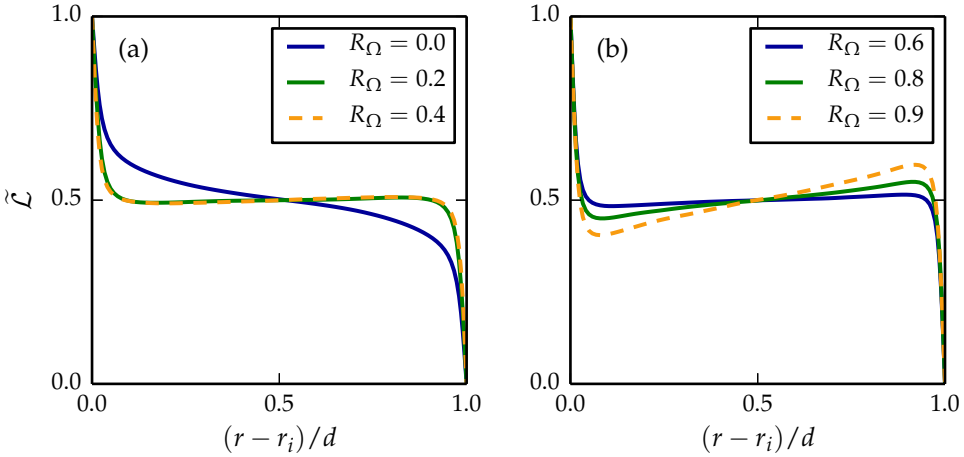

FIGURE 5.2: Angular momentum profiles for various rotation numbers R_Ω at a constant shear $Re_S = 2 \times 10^4$ in a low-curvature TC system with $\eta = 0.99$. The angular momentum profile $\langle \mathcal{L} \rangle$ in the inertial frame was rescaled to the interval $(0, 1)$ using the transformations $\widetilde{\mathcal{L}} = (\langle \mathcal{L} \rangle - \mathcal{L}_o)/(\mathcal{L}_i - \mathcal{L}_o)$, where $\mathcal{L}_i$ and $\mathcal{L}_o$ denote the specific angular momentum of the inner and outer cylinder.

muthally and axially averaged angular momentum profiles $\langle \mathcal{L} \rangle$ from turbulent simulations at $Re_S = 2 \times 10^4$. To exemplify the profile shapes characteristic of low-curvature TCF, Figure 5.2 shows $\mathcal{L}$ profiles for $\eta = 0.99$, which are rescaled to the interval $(0, 1)$ in order to compare them between simulations at different R_Ω. For most rotation numbers, the angular momentum profiles become almost flat in the middle and reach a central value of $\widetilde{\mathcal{L}} \approx 0.5$. Our previous analysis in Section 4.5.1 revealed this profile behaviour also for other radius ratios, as long as no stabilisation of the flow due to a counter-rotating outer cylinder occurs. That angular momentum profiles become nearly flat in the centre was also observed in TC experiments with the outer cylinder held stationary (Wattendorf, 1935; Taylor, 1935; Smith & Townsend, 1982; Lewis & Swinney, 1999).

In the limit $\eta \to 1$, TCF becomes linearly unstable for sufficiently high Re_S only in the range $0 < R_\Omega < 1$ (Dubrulle *et al.*, 2005). The $\mathcal{L}$ profile for the lower stability boundary $R_\Omega = 0$ (corresponding to perfect counter-rotation with $r_i \omega_i = -r_o \omega_o$) features a central region of negative slope, see Figure 5.2(a). Moreover, the profiles show an increasingly larger gradient in the middle as R_Ω tends to 1, cf. Figure 5.2(b). However, this increase is only caused by the rescaling of the profiles by the difference $(\mathcal{L}_i - \mathcal{L}_o)$: In the limit $R_\Omega \to 1$, this quantity vanishes since the marginal stability boundary $R_\Omega = 1$ is determined by Rayleigh's criterion and the equality of angular momentum at the inner and outer cylinder (Rayleigh, 1917).

universality of profile gradients

Indeed, Figure 5.3 shows that the profile gradients in the centre measured in advective units do not increase for large R_Ω and are close to zero for $R_\Omega \gtrsim 0$. Furthermore, the gradients only slightly vary with Re_S (Figure 5.3(a)) and do not differ between simulations for $\eta = 0.9$ and 0.99 (Figure 5.3(b)), which highlights the universal behaviour of the $\mathcal{L}$ profiles in the centre. It is important to note that a radially constant angular mo-

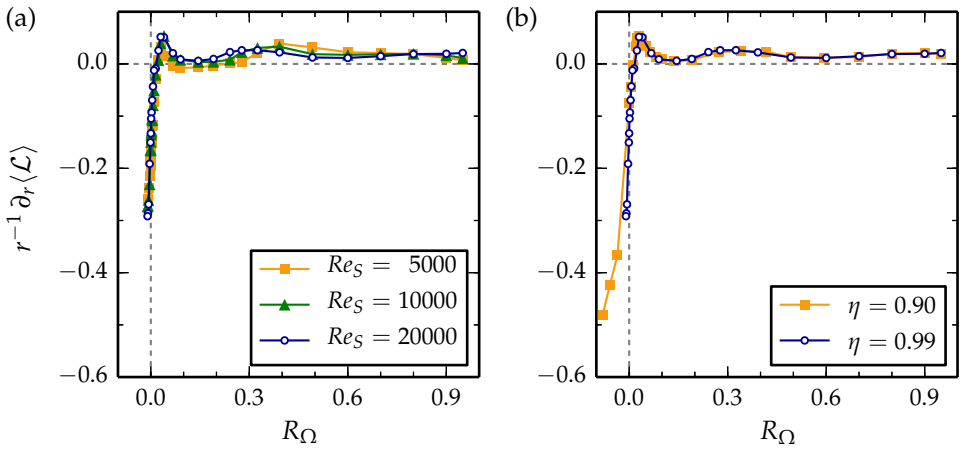

FIGURE 5.3: Angular momentum gradients in the middle region as a function of the rotation number R_Ω. (a) The gradients for $\eta = 0.99$ only slightly vary with Re_S. (b) At $Re_S = 2 \times 10^4$, the gradients for two different radius ratios coincide. For most values of R_Ω, the angular momentum profiles are almost flat in the middle region with a slight positive slope. We calculated the gradient by averaging the profile derivative divided by the radius ($r^{-1}\partial_r\langle\mathcal{L}\rangle$) over the central region $(r - r_i)/d \in [0.4, 0.6]$.

mentum complies with marginal stability according to Rayleigh's inviscid criterion and that at high Re_S, viscosity plays an important role only close to the walls and not in the central region. Thus, one can interpret the constant angular momentum profiles in the middle to be in a marginally stable state (Wattendorf, 1935; Taylor, 1935), see also Section 4.5.2. However, marginal stability is not exactly fulfilled, and the $\mathcal{L}$ profiles show a slightly positive slope in the middle as previously observed by Smith & Townsend (1982), Lewis & Swinney (1999) and Dong (2007). The general occurrence of an almost flat central region in the angular momentum profile for $R_\Omega \gtrsim 0$ serves as one key ingredient for the subsequent model.

5.2 MARGINAL STABILITY MODEL

The rotation-number dependence of the torque and of the mean profiles, which we seek to understand, results from a complicated turbulent flow that arises from the hydrodynamic equations of motion. Our model, however, will not be based on the full equations of motion. Instead, we hypothesise a few simple rules, which the turbulent flow has to obey in the statistical average. The rules are motivated by the physical concept of marginal stability, which can be benchmarked against the real turbulence by comparing model predictions to DNS results afterwards. This modelling approach is inspired by similar arguments used to estimate the heat transport in thermal convection (Malkus, 1954; Howard, 1966). Moreover, our model is based on a previous marginal stability model for TCF with stationary outer cylinder (King *et al.*, 1984; Marcus, 1984b), which is here extended to the general case of independently rotating cylinders.

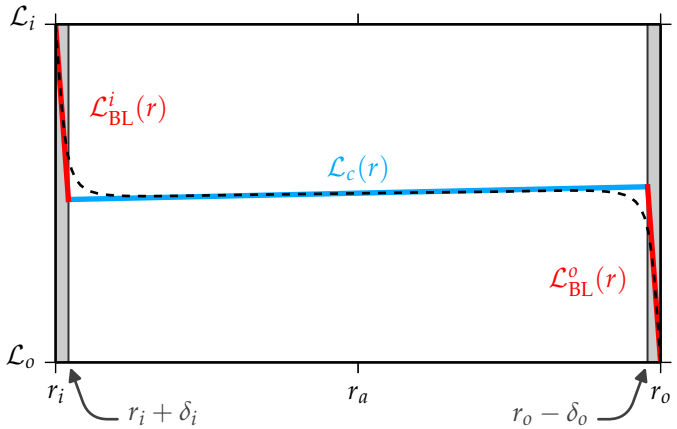

FIGURE 5.4: The marginal stability model describes the angular momentum profile by three linear regions: the inner and outer BL $\mathcal{L}^i_{\mathrm{BL}}(r)$ and $\mathcal{L}^o_{\mathrm{BL}}(r)$ having a thickness of δ_i and δ_o, respectively, and the central region $\mathcal{L}_c(r)$. The model profile (solid lines) calculated for $\eta = 0.99$, $Re_S = 2 \times 10^4$ and $R_\Omega = 0.5$ is compared to the corresponding DNS profile (dashed line).

5.2.1 *Structure of the model*

three model assumptions

The model consists of the following three assumptions:

(i) In the inertial reference frame, the angular momentum profile can be approximated by a sequence of three linear functions as sketched in Figure 5.4: The inner BL profile $\mathcal{L}^i_{\mathrm{BL}}(r)$ extending from r_i to the radius $r_i + \delta_i$, the outer BL profile $\mathcal{L}^o_{\mathrm{BL}}(r)$ extending from the radius $r_o - \delta_o$ to r_o and the central profile $\mathcal{L}_c(r)$ in between. Here, δ_i and δ_o denote the inner and outer BL thickness. This assumption is motivated by the profile shapes observed in the DNS (Figure 5.2), which, however, exhibit a smooth transition from the BL to the central part. Therefore, the piecewise linear profile should be regarded as a simple approximation that hopefully reproduces the essential functional dependence on R_Ω.

(ii) Next, we require that the angular momentum profile in the centre features a small positive slope, meaning that it nearly fulfils marginal stability according to Rayleigh's criterion for inviscid flows (Rayleigh, 1917). We approximate the profile slope by the Re_S- and R_Ω-independent constant $s = 0.02 r_a$, where the proportionality to the mean radius $r_a = (r_i + r_o)/2$ accounts for the observation that the profile gradient divided by the radius ($r^{-1}\partial_r \langle \mathcal{L} \rangle$) becomes almost independent of η, Re_S and R_Ω for $R_\Omega \gtrsim 0$, cf. Figure 5.3. Thus, in advective units the central profile reads

$$\mathcal{L}_c(r) = \mathcal{L}_a + s(r - r_a) \qquad \text{with} \qquad s = 0.02 r_a, \tag{5.2}$$

where $\mathcal{L}_a$ denotes the angular momentum at the mean radius r_a. Note that while we fixed the slope s, the variable $\mathcal{L}_a$ is yet unknown

and may depend on the external parameters (η, Re_S, R_Ω). Similarly, the extent of the central region defined by the BL thicknesses δ_i and δ_o is yet unknown.

(iii) Analogous to the centre, the BLs are assumed to be in a marginally stable state which determines the thicknesses δ_i and δ_o. More precisely as proposed by King *et al.* (1984), each BL is modelled as marginally stable TC system extending from the inner or outer cylinder to the respective external edge of the BL.

increased effective width of BLs

In contrast to a real TC system, the virtual cylinder formed by the BL edge behaves more like a free surface, which influences the stability as also noted by King *et al.* (1984). Thus, the BL edge effectively leaves more space for the instability modes than a rigid wall would. A similar configuration occurs in TCF with counter-rotating cylinders where the formed vortices are wider than the unstable inner region (Taylor, 1923), pointing to an increased effective length scale for the instability modes (Donnelly & Fultz, 1960; Esser & Grossmann, 1996). Therefore, we define the effective gap width of the virtual TC systems as $d_i = \widetilde{a}\delta_i$ and $d_o = \widetilde{a}\delta_o$ with the constant $\widetilde{a} > 1$. A comparison between model and DNS in Section 5.2.2 will reveal that $\widetilde{a} = 1.5$ represents a reasonable choice in case of $Re_S = 2 \times 10^4$. Altogether, the virtual TC system of the inner BL can be characterised by an effective radius ratio η_i, a first Reynolds number $\mathcal{R}_1^i$ for the real cylinder and a second Reynolds number $\mathcal{R}_2^i$ for the BL edge:

$$\eta_i = \frac{r_i}{r_i + d_i}, \qquad \mathcal{R}_1^i = \frac{\check{\mathcal{L}}_i d_i}{r_i \nu}, \qquad \mathcal{R}_2^i = \frac{\check{\mathcal{L}}_c(r_i + d_i)\, d_i}{(r_i + d_i)\nu}, \tag{5.3}$$

with $d_i = \widetilde{a}\delta_i$. Here, the angular momenta $\check{\mathcal{L}}_i$ and $\check{\mathcal{L}}_c(r_i + d_i)$ are given in physical units and therefore labelled with a wedge accent (ˇ). Since the new unit of length in (5.3) is the effective gap width d_i, the dimensionless radii become $r_1^i = \eta_i/(1-\eta_i)$ and $r_2^i = 1/(1-\eta_i)$ for the BL TC system. Similarly, the virtual TC system of the outer BL is characterised by an effective radius ratio η_o, a first Reynolds number $\mathcal{R}_1^o$ for the BL edge and a second Reynolds number $\mathcal{R}_2^o$ for the real cylinder:

$$\eta_o = \frac{r_o - d_o}{r_o}, \qquad \mathcal{R}_1^o = \frac{\check{\mathcal{L}}_c(r_o - d_o)\, d_o}{(r_o - d_o)\nu}, \qquad \mathcal{R}_2^o = \frac{\check{\mathcal{L}}_o d_o}{r_o \nu}, \tag{5.4}$$

with $d_o = \widetilde{a}\delta_o$. Here, the effective gap width d_o is the new unit of length, and the dimensionless radii become $r_1^o = \eta_o/(1-\eta_o)$ and $r_2^o = 1/(1-\eta_o)$.

three model variables and conditions

Since the constants s and $\widetilde{a}$ were already set based on empirical observations, all in all, the model includes three unknown variables (the central angular momentum $\mathcal{L}_a$ and the BL thicknesses δ_i and δ_o) that need to be determined for each set of external parameters (η, Re_S, R_Ω). Using the following three conditions, they can be calculated: First, we implement the assumption of marginal stability from (iii) by requiring that both BLs described by the parameters (5.3) and (5.4) fulfil the stability criterion for laminar TCF by Esser & Grossmann (1996). We resort to their study since

it provides an analytic expression for the stability boundary in the full parameter space, which is in good agreement with experimental results. These two conditions for the BLs determine δ_i and δ_o, but they also depend on the unknown $\mathcal{L}_a$, which enters $\mathcal{R}_2^i$ and $\mathcal{R}_1^o$ via the central profile $\mathcal{L}_c(r)$ from (5.2) evaluated at $r = r_i + d_i$ and $r = r_o - d_o$, respectively.

torque equality

In the statistically stationary state and averaged over long times, the torque exerted on the inner cylinder equals that exerted on the outer cylinder, which serves as the third condition needed to determine $\mathcal{L}_a$. Since the torque is proportional to the mean wall shear stress, cf. equation (5.1), which is calculated from the linearly approximated BL profiles $\mathcal{L}^i_{\mathrm{BL}}(r)$ and $\mathcal{L}^o_{\mathrm{BL}}(r)$, the dimensionless torques at the inner and outer cylinder read

$$\begin{aligned} G_i &= Re_S\left(-r_i\,\partial_r\mathcal{L}^i_{\mathrm{BL}}\Big|_{r_i} + 2\mathcal{L}_i\right) = Re_S\left(r_i\frac{\mathcal{L}_i - \mathcal{L}_c(r_i+\delta_i)}{\delta_i} + 2\mathcal{L}_i\right), \\ G_o &= Re_S\left(-r_o\,\partial_r\mathcal{L}^o_{\mathrm{BL}}|_{r_o} + 2\mathcal{L}_o\right) = Re_S\left(r_o\frac{\mathcal{L}_c(r_o-\delta_o) - \mathcal{L}_o}{\delta_o} + 2\mathcal{L}_o\right). \end{aligned} \tag{5.5}$$

Thus, the third condition becomes $G_i = G_o$ and also depends on all three model variables $\mathcal{L}_a$, δ_i and δ_o. Consequently, all three conditions are coupled, and we solve them numerically because the employed stability equations by Esser & Grossmann (1996) are implicit. For given parameter values (η, Re_S, R_Ω), this procedure results in model predictions for $\mathcal{L}_a$, δ_i and δ_o, which additionally provide a model estimate for the torque by utilising equation (5.5). In this context, it is important that the BL thicknesses δ_i and δ_o are used to approximate the profile derivatives in (5.5), whereas the increased gap widths d_i and d_o are relevant for the Reynolds numbers in (5.3) and (5.4) that describe the stability of the BLs.

DNS quantities for comparison

Finally, the model predictions can be complemented by the corresponding quantities calculated from our numerical simulations. While the definitions of the central angular momentum $\mathcal{L}_a = \mathcal{L}(r_a)$ and of the torque G also apply to the DNS, a BL-thickness definition inspired by the model is needed for general $\mathcal{L}$ profiles from simulations or experiments. Therefore, we also approximate angular momentum profiles from the DNS by three lines similar to the model profile in Figure 5.4. We define the distance of the two intersection points to the corresponding wall as BL thicknesses δ_i and δ_o. These lines are obtained by a linear fit to the middle region of the DNS profile and by using the derivatives $\partial_r\langle\mathcal{L}\rangle|_{r_i}$ and $\partial_r\langle\mathcal{L}\rangle|_{r_o}$ as the slope for the line describing the inner and outer BL, respectively.

5.2.2 *Model predictions*

We study the marginal stability model for a constant shear $Re_S = 2\times10^4$ and for the two radius ratios $\eta = 0.99$ and $\eta = 0.9$. The first η value was chosen to analyse the limit where the cylinder curvature plays a negligible role. For $\eta = 0.99$, the dimensionless cylinder radii become $r_i/d = 99$ and $r_o/d = 100$; thus, inner and outer BL behave similarly. Therefore, we only show results for the inner BL here. On the other hand, $\eta = 0.9$ corresponds

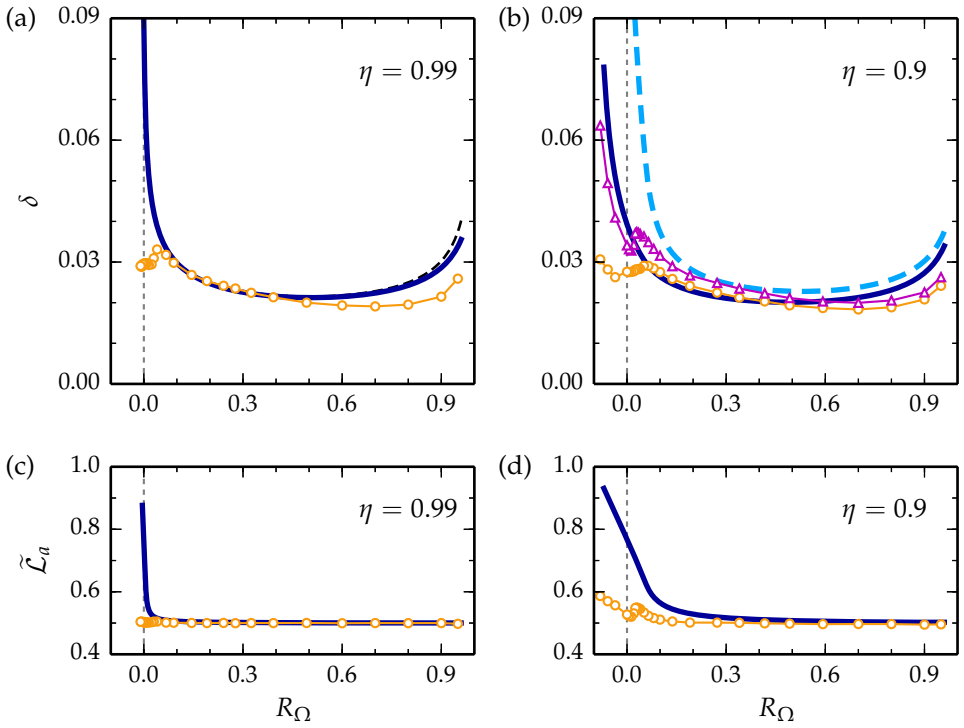

FIGURE 5.5: Comparison of the model predictions (lines) with the DNS results (symbols) for $Re_S = 2 \times 10^4$ and two radius ratios showing BL thicknesses in (a,b) and the central angular momentum $\mathcal{L}_a = \langle \mathcal{L} \rangle (r_a)$ rescaled by the transformation $\widetilde{\mathcal{L}}_a = (\mathcal{L}_a - \mathcal{L}_o)/(\mathcal{L}_i - \mathcal{L}_o)$ in (c,d) as a function of R_Ω. Since $\delta_o \approx \delta_i$ for $\eta = 0.99$, (a) only includes the inner BL thickness δ_i (solid line, circles). In (b) the outer BL thickness δ_o is shown by the dashed line (model) and by triangles (DNS). Assuming a constant profile in the centre, i.e. inserting $s = 0$ into (5.2), increases the BL thickness predicted by the model for large R_Ω as illustrated for δ_i by the black dashed line in (a).

to the smallest radius ratio, for which we still observe the two torque maxima that are characteristic of the low-curvature TCF (see Section 4.3). Since the cylinder radii are approximately ten times smaller compared to the $\eta = 0.99$ case, we expect the curvature to become relevant. Thus, the $\eta = 0.9$ case enables us to analyse how curvature effects are represented in the marginal stability model.

BL thickness comparison

Figure 5.5 compares the model prediction for BL thickness and central angular momentum to corresponding DNS results and shows the variation of these quantities with the mean system rotation parametrised by R_Ω. For $\eta = 0.99$, the model and DNS results for δ_i coincide in a wide R_Ω range. However, they deviate for $R_\Omega \gtrsim 0.5$, but both still show the same upward trend for large R_Ω (Figure 5.5(a)). Clearly, the model drastically overestimates the BL thickness when the system rotation (R_Ω) tends to zero. This discrepancy will be explained and resolved in Section 5.3. We observe a similar agreement between model and DNS for $\eta = 0.9$ in Figure 5.5(b), where the variation of the inner and outer BL thickness with R_Ω resembles the $\eta = 0.99$ case. However, for $\eta = 0.9$ the outer BL is

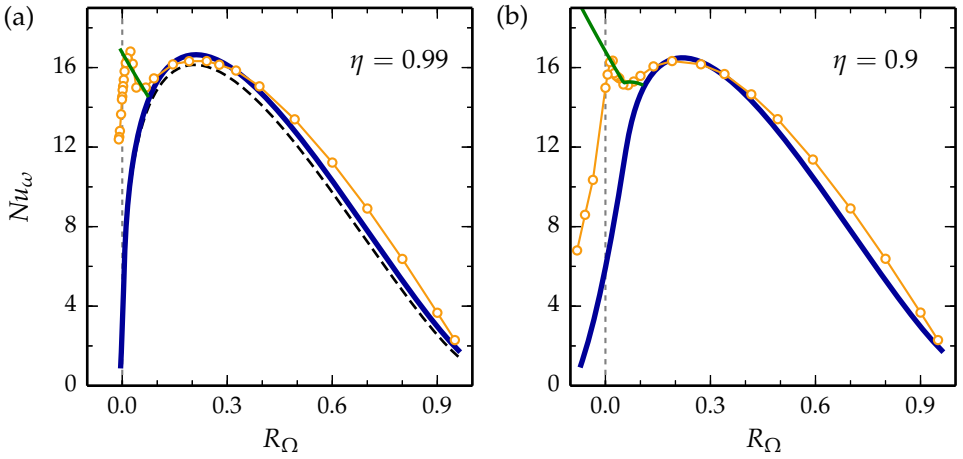

FIGURE 5.6: Comparison of the torques ($Nu_\omega = G/G_{\text{lam}}$) estimated by the model (blue line) and calculated in the DNS (circles) as a function of R_Ω for $Re_S = 2 \times 10^4$ and two radius ratios. The green line for $R_\Omega < 0.07$ in (a) and for $R_\Omega < 0.1$ in (b) originates from an improved model discussed in Section 5.3 which rationalises the beginning of the narrow maximum. Assuming a constant profile in the centre, by inserting $s = 0$ into (5.2), only slightly changes the model prediction for the torque as exemplified by the dashed line in (a).

thicker than the inner one, and the marginal stability model correctly reproduces this curvature effect. Furthermore, the curvature causes a radial difference in stability when the cylinders counter-rotate, which happens in case of $\eta = 0.9$ for $R_\Omega < 0.1$. Then, the counter-rotating outer cylinder stabilises an outer layer while the inner region is still centrifugally unstable (Chandrasekhar, 1961). Such a stabilisation permits a thicker BL, and both DNS and model reflect the radial difference in stability by a much larger δ_o than δ_i for negative and slightly positive R_Ω values.

comparison of $\mathcal{L}_a$

The model prediction for the central angular momentum $\mathcal{L}_a$ agrees well with the DNS result, except for small R_Ω values, as shown in Figure 5.5(c,d). For most rotation numbers, $\mathcal{L}_a$ reaches the mean value $(\mathcal{L}_i + \mathcal{L}_o)/2$ corresponding to $\widetilde{\mathcal{L}}_a = 0.5$, which indicates that both BLs feature the same angular momentum drop. This symmetric behaviour changes in the marginal stability model as shown by the increase of $\widetilde{\mathcal{L}}_a$ for $R_\Omega \to 0$, which implies a larger angular momentum difference over the outer BL. Together with this profile asymmetry, the aforementioned stabilisation of the outer BL caused by counter-rotating cylinders occurs and, thus, enables a larger shear gradient in the outer BL while maintaining marginal stability. For $\eta = 0.9$, the predicted $\widetilde{\mathcal{L}}_a$ starts to increase at a larger R_Ω value than for $\eta = 0.99$. This is in accordance with the fact that counter-rotation corresponds to $R_\Omega < 0.1$ and $R_\Omega < 0.01$ for $\eta = 0.9$ and $\eta = 0.99$, respectively.

torque comparison

Equation (5.5) translates these profile characteristics, i.e. $\mathcal{L}_a$, δ_i and δ_o, into a marginal stability prediction for the torque, which is compared to the DNS results for $\eta = 0.99$ and $\eta = 0.9$ in Figure 5.6. Similar to the behaviour of the BL thicknesses (cf. Figure 5.5(a,b)), the torques coincide in the range $0.1 \lesssim R_\Omega \lesssim 0.5$ and show small deviations for larger rotation

numbers. Thereby, the model reproduces the broad torque maximum at $R_\Omega = 0.2$, suggesting that the marginal stability of mean profiles causes this rotation-number dependence of the torque. In contrast, the model does not reproduce the narrow torque maximum at $R_\Omega = 0.02$ from the DNS, but it predicts a strong decrease in Nu_ω as R_Ω tends to zero. Consequently, the formation of the second torque maximum must result from another mechanism than marginal stability, which will be discussed in the following section.

effect of the model constants $\widetilde{a}$ and s

Finally, we note that the only model parameter, whose value was not determined by the model assumptions, is the constant $\widetilde{a} > 1$ which describes the effectively larger gap widths $d_i = \widetilde{a}\delta_i$ and $d_o = \widetilde{a}\delta_o$ for the Reynolds numbers of the BLs. The introduction of $\widetilde{a}$ is physically justified by the free-surface boundary condition at the BL edge, and its value determines the general magnitude of model torques in Figure 5.6. However, the variation of the torque with R_Ω does not depend on the value of $\widetilde{a}$. We chose the constant $\widetilde{a} = 1.5$ so that the amplitude of the model-torque maximum matches the DNS torques. In contrast, the magnitude of the profile slope in the centre was set to $s = 0.02 r_a$ beforehand in accordance with empirical observations. Alternatively, one could have postulated that the central profile exactly realises marginal stability according to Rayleigh's criterion, which requires a constant angular momentum and thus the slope $s = 0$. In a previous marginal stability model, the angular momentum was assumed to be constant in the central region (King *et al.*, 1984; Marcus, 1984b), and the effect of setting $s = 0$ in our model is exemplified for $\eta = 0.99$ by the dashed line in Figure 5.5(a) and Figure 5.6(a): The BL-thickness predictions with $s = 0$ and $s = 0.02 r_a$ only differ for large R_Ω values, with the $s = 0.02 r_a$ case being closer to the DNS result. Similarly, the model prediction for the torque only slightly varies with the value of s, and the variation would not be recognisable for the central angular momentum $\mathcal{L}_a$ in Figure 5.5(c). In conclusion, the rotation-number dependence predicted by the model depends neither on the value of $\widetilde{a}$ nor on the two choices for the profile gradient in the central region.

5.3 BOUNDARY-LAYER TRANSITION

The observed discrepancy between model and DNS for small rotation numbers points to a deviation of the flow from the marginal stability behaviour. Since this discrepancy also occurs for the BL thicknesses in Figure 5.5(a,b), we expect that the change in stability takes place in the BLs. To further assess their stability, we assign a shear Reynolds number to the inner and outer BL defined as

BL Reynolds numbers

$$Re^i_{\mathrm{BL}} = \frac{\hat{r}_i \left(\omega_i - \omega|_{r_i+\delta_i} \right) \delta_i}{\nu}, \qquad Re^o_{\mathrm{BL}} = \frac{\hat{r}_o \left(\omega|_{r_o-\delta_o} - \omega_o \right) \delta_o}{\nu}, \tag{5.6}$$

with the typical radii $\hat{r}_i = r_i + \delta_i/2$ and $\hat{r}_o = r_o - \delta_o/2$. These Reynolds numbers are based on the angular velocity gradient across the BL and re-

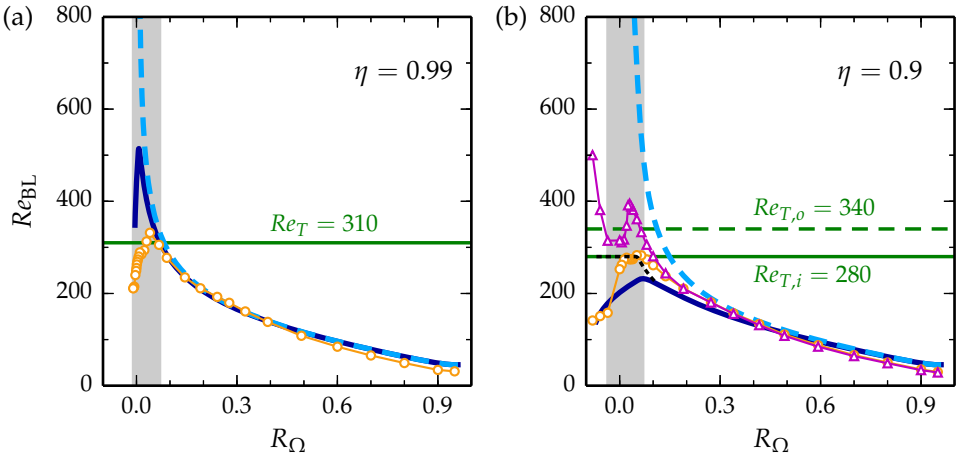

FIGURE 5.7: Inner and outer BL Reynolds number Re_{BL} predicted by the model (solid and dashed line) and calculated from the DNS (circles and triangles) for $Re_S = 2 \times 10^4$ and two radius ratios. In the DNS for $\eta = 0.99$, Re^o_{BL} coincides with Re^i_{BL} and therefore is left out in (a). While Re_{BL} predicted by marginal stability strongly increases for $R_\Omega \to 0$ (only for outer BL in (b)), it reaches a maximum and drops again in the DNS, indicating a transition to turbulent BLs, which occurs for $R_\Omega < 0.07$ in the grey-shaded area. This is implemented in an improved model by additionally requiring that the BL Reynolds number cannot exceed a transition Reynolds number Re_T marked by the green lines. Then, the model reproduces the beginning of the narrow torque maximum in Figure 5.6. In the improved model, Re^i_{BL} for $\eta = 0.9$ also increases to $Re_{T,i}$ as shown by the dotted line in (b).

semble the ones defined by van Gils *et al.* (2012). Figure 5.7 compares Re^i_{BL} and Re^o_{BL} predicted by the model (lines) to the corresponding DNS results (symbols). For the DNS with $\eta = 0.99$, we again only show results for Re^i_{BL} since they coincide with Re^o_{BL}. While for most rotation numbers, model and DNS are in good agreement, the pronounced discrepancy for small R_Ω values occurs again. In the DNS, the shear gradient across the BL increases with decreasing rotation number, reaches a maximum at a small positive R_Ω value and then drops again. In contrast, the model predicts a drastic increase of the BL Reynolds number (only Re^o_{BL} for $\eta = 0.9$) when R_Ω tends to 0. This increase is unrealistic since BLs are known to undergo a transition to turbulence if their Reynolds number exceeds a critical value Re_T (Schlichting & Gersten, 2006), as previously discussed for TCF by van Gils *et al.* (2012). For example, a Prandtl–Blasius BL becomes linearly unstable for $Re_{\mathrm{BL}} > 520$ (Schmid & Henningson, 2001). However, the presence of free-stream turbulence above the BL (as is the case here in TCF) lowers the transition Reynolds number Re_T (van Driest & Blumer, 1963; Andersson, Berggren & Henningson, 1999) since such strong disturbances can cause bypass transitions in the BL. Consequently, in reality the marginal stability of the BLs according to the TC stability criterion (Esser & Grossmann, 1996) is bypassed by a transition to turbulence following another route.

drastic increase of Re_{BL} in model

This BL transition can be incorporated into the model by means of the additional assumption that the BLs are also marginally stable with respect to the transition Reynolds number Re_T, which means that Re^i_{BL} and Re^o_{BL}

modelling the BL transition

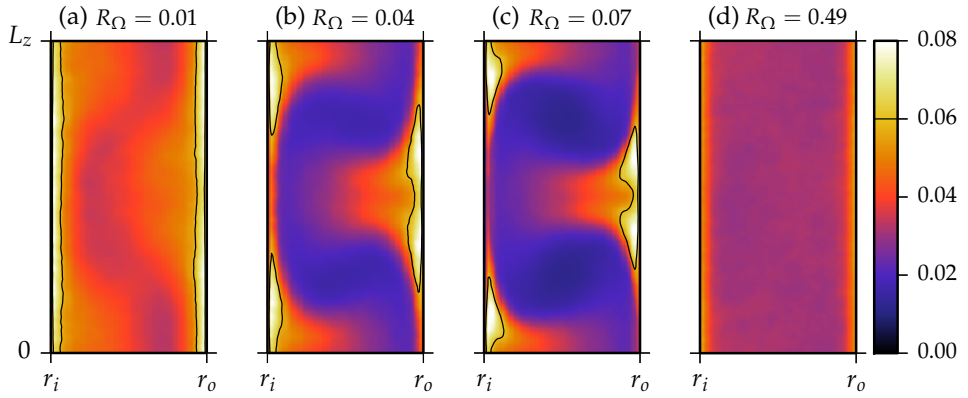

FIGURE 5.8: Azimuthal- and time-averaged RMS ($\mathcal{L}_{\mathrm{rms}}$) of the angular momentum fluctuations $\mathcal{L}'' = \mathcal{L} - \langle\mathcal{L}\rangle_{\varphi,t}$ calculated for various values of R_Ω in DNS with $\eta = 0.99$ and $Re_S = 2 \times 10^4$. $\mathcal{L}$ is measured in units of $\widetilde{r}dU_o$ with the geometric mean radius $\widetilde{r} = \sqrt{r_i r_o}/d$. All plots use the same colour scale, and the contour line marks strongly turbulent regions with $\mathcal{L}_{\mathrm{rms}} > 0.06$, which are absent in (d), cover a limited axial fraction of the BL in (b,c) and extent over the entire BL in (a). The axial fraction F_T of the strongly turbulent regions is further analysed in Figure 5.9(a).

must equal Re_T if they would exceed this value otherwise. The critical values $Re_T = 310$ for $\eta = 0.99$ as well as $Re_{T,i} = 280$ and $Re_{T,o} = 340$ for $\eta = 0.9$ approximate the maximal magnitude of the shear gradient occurring in the DNS, as indicated by the horizontal lines in Figure 5.7. These Re_T values suggest that, as a result of the increased cylinder curvature for $\eta = 0.9$, the outer BL becomes turbulent at a higher shear rate than the inner one. Furthermore, we note for the $\eta = 0.9$ case that in the improved model, Re^i_{BL} also reaches the transition at $Re_{T,i}$ as demonstrated by the dotted line in Figure 5.7(b).

formation of narrow torque maximum

With the additional assumption of marginal stability with respect to the BL transition, the model now also reproduces the onset of the narrow torque maximum, as shown by the green line for $R_\Omega < 0.07$ and for $R_\Omega < 0.1$ in Figure 5.6(a) and (b), respectively. The two bends in the torque curve for $\eta = 0.9$ result from two different R_Ω values for the inner and outer BL transition in this case. In contrast to the DNS results, the model still does not include the torque decrease for $R_\Omega < 0.02$, which, however, is plausible since in the limit $\eta \to 1$, the complete flow becomes linearly stable for $R_\Omega < 0$ (Dubrulle *et al.*, 2005). All in all, the model suggests that the narrow torque maximum originates from the transition to turbulent BLs for rotation numbers $R_\Omega < 0.07$ highlighted by shaded regions in Figure 5.7. This hypothesised transition needs to be double-checked, and we will look for evidence in our numerical simulations below.

evidence for BL transition in $\mathcal{L}_{\mathrm{rms}}$

Turbulent BLs consist of small vortices that generate high- and low-speed streaks close to the wall, which cause strong fluctuations of the downstream velocity u_φ and likewise of $\mathcal{L} = ru_\varphi$. Remarkably, the angular momentum fluctuations $\mathcal{L}'' = \mathcal{L} - \langle\mathcal{L}\rangle_{\varphi,t}$ are generally of comparable amplitude in both BL regions in contrast to the velocity fluctuations u''_φ.

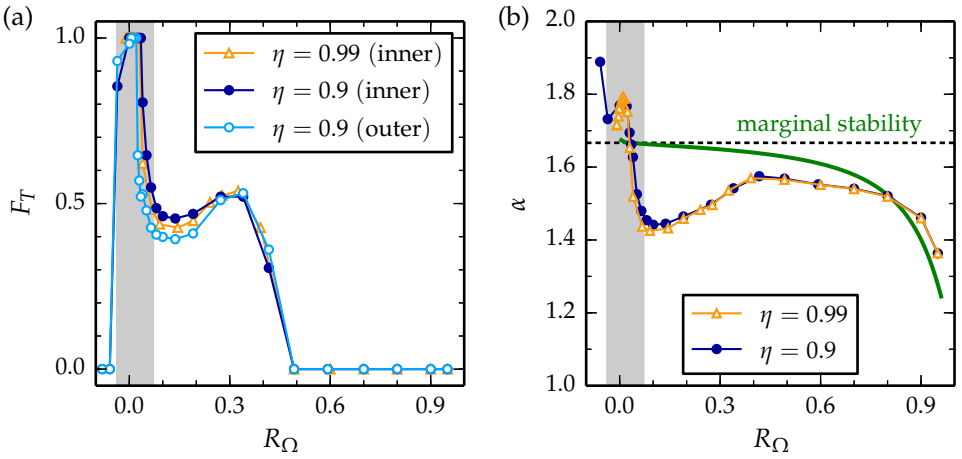

FIGURE 5.9: Indicators for the transition to turbulent BLs in the DNS as a function of the rotation number R_Ω: (a) Axial fraction F_T covered by strongly turbulent regions with $\mathcal{L}_{\text{rms}} > 0.06$ (cf. Figure 5.8) for $Re_S = 2 \times 10^4$. Since F_T of the inner and outer BL coincide for $\eta = 0.99$, only the inner value is shown. (b) The torque scaling exponent α, defined by $G \propto Re_S^\alpha$, was calculated for each R_Ω individually by a linear fit on a double-logarithmic scale using DNS results for $Re_S = 5 \times 10^3$, 10^4 and 2×10^4. The corresponding scaling exponent for $\eta = 0.99$ predicted by the marginal stability model (green line) is based on model torques in the range $5 \times 10^3 \leq Re_S \leq 2 \times 10^4$ and approaches the asymptotic limit $\alpha = 5/3$ (dotted line) for $R_\Omega \to 0$. This marginal stability limit is exceeded in the DNS for $R_\Omega < 0.03$. The BLs become turbulent for $R_\Omega < 0.07$ in the region shaded in grey.

Therefore, we analyse the azimuthal- and time-averaged RMS of the angular momentum fluctuations $\mathcal{L}_{\text{rms}} = (\langle \mathcal{L}''^2 \rangle_{\varphi,t})^{1/2}$ as a first indicator for the BL transition similar to that used by Ostilla-Mónico *et al.* (2014b). Figure 5.8 shows $\mathcal{L}_{\text{rms}}$ in the radial-axial plane for various values of R_Ω and the example case $\eta = 0.99$. Since all plots use the same colour scale, it becomes apparent that for $R_\Omega = 0.49$ (Figure 5.8(d)) the fluctuations are relatively small indicating quiet BLs. At the same time, no axial variation in $\mathcal{L}_{\text{rms}}$ that would indicate the presence of Taylor vortices is discernible. This changes with decreasing R_Ω as exemplified for $R_\Omega = 0.07$ in Figure 5.8(c): A limited axial fraction of each BL becomes turbulent, as evidenced by strong fluctuations in the regions marked by the contour line at $\mathcal{L}_{\text{rms}} = 0.06$. The axial position of these turbulent BL regions correlates with the radial flow produced by the existing Taylor vortex pair: Inner and outer BL are turbulent only adjacent to the outflow (top/bottom) and inflow region (middle), respectively. The coexistence of laminar and turbulent regions in the BLs corresponds to the *transitional regime* described by Ostilla-Mónico *et al.* (2014b) for $\eta = 0.714$ and a stationary outer cylinder. When R_Ω further decreases below 0.07, the turbulent part of each BL grows in height (Figure 5.8(b)) until the entire BL becomes turbulent (Figure 5.8(a)), as suggested by the marginal stability model. Simultaneously, the axial variation of $\mathcal{L}_{\text{rms}}$ in the centre, and hence the Taylor vortices, become weaker.

transitional regime

turbulent fraction of the BL

To analyse this transition process quantitatively, we calculate the axial fraction F_T of each BL that is covered by strong turbulence with $\mathcal{L}_{\text{rms}} > 0.06$.

Since the turbulent fractions of the outer and inner BL coincide for $\eta = 0.99$, Figure 5.9(a) only shows the latter for this radius ratio and both for $\eta = 0.9$. For $R_\Omega \geq 0.5$ no strongly turbulent BL region occurs in accordance with the small BL Reynolds number in this rotation-number range, cf. Figure 5.7. Then, in the range $0.07 < R_\Omega < 0.4$ the turbulent fraction increases, and approximately half of the BL becomes turbulent. This *transitional regime* is also characterised by strong Taylor vortices (see Section 4.4 and Section 4.5.3), which interact with the BL dynamics (Ostilla-Mónico *et al.*, 2014b). Finally, for $R_\Omega < 0.07$ the turbulent fraction sharply increases to one, indicating the transition to entirely turbulent BLs which was hypothesised by the model. For $\eta = 0.9$, the turbulent fraction drops again for negative rotation numbers, consistent with the fact that in these flow cases, the outer cylinder strongly counter-rotates and thereby re-stabilises the flow. Interestingly, the critical rotation number for the transition to turbulence depends on the wall curvature, whereas the general variation of F_T with R_Ω does not differ between both η values: For $\eta = 0.9$, the inner and outer BL become turbulent at a larger and smaller R_Ω value, respectively, than the BLs for $\eta = 0.99$. This difference represents another curvature effect and is consistent with the smaller inner (larger outer) transition Reynolds number $Re_{T,i}$ ($Re_{T,o}$), introduced to describe the DNS results for $\eta = 0.9$ in Figure 5.7(b).

transition to entirely turbulent BLs

As a second indicator for the BL transition, we analyse the local power-law scaling of the torque with Re_S, i.e. the exponent α from $G \propto Re_S^\alpha$, which was previously found to differ between flows with laminar and turbulent BLs (Lathrop, Fineberg & Swinney, 1992b,a; Lewis & Swinney, 1999; Ostilla-Mónico *et al.*, 2014b). Based on the key assumption of laminar BLs that are marginally stable to the formation of Taylor vortices, a previous marginal stability calculation predicts the scaling exponent $\alpha = 5/3$ in the limit of large Re_S (King *et al.*, 1984; Marcus, 1984b). The same exponent was calculated by Barcilon & Brindley (1984) by assuming BLs that are marginally stable to Görtler vortices. In this context, a torque scaling exponent $\alpha > 5/3$ has been linked to a flow with turbulent BLs (Ostilla-Mónico *et al.*, 2014b).

torque scaling exponent

In Figure 5.9(b), we analyse the variation of the torque scaling exponent with R_Ω and compare the exponent from the DNS to the one predicted by the marginal stability model without BL transition. We first note that there is hardly any difference between the cases of $\eta = 0.9$ and $\eta = 0.99$. The exponent predicted by the model lies below the asymptotic value $\alpha = 5/3$ because it is calculated for finite Re_S ranging between 5×10^3 and 2×10^4. For $R_\Omega \gtrsim 0.4$, the model qualitatively reproduces the variation of the exponent with R_Ω from the DNS, which also suggests that the BLs are laminar in this regime. In the range $0.07 < R_\Omega < 0.4$ corresponding to the regime where laminar and turbulent regions in the BL coexist (cf. Figure 5.9(a)), the exponent significantly falls below the marginal stability prediction, as observed by Ostilla-Mónico *et al.* (2014b) in their *transitional regime*. Finally, for $R_\Omega < 0.07$ the scaling exponent sharply rises demonstrating increas-

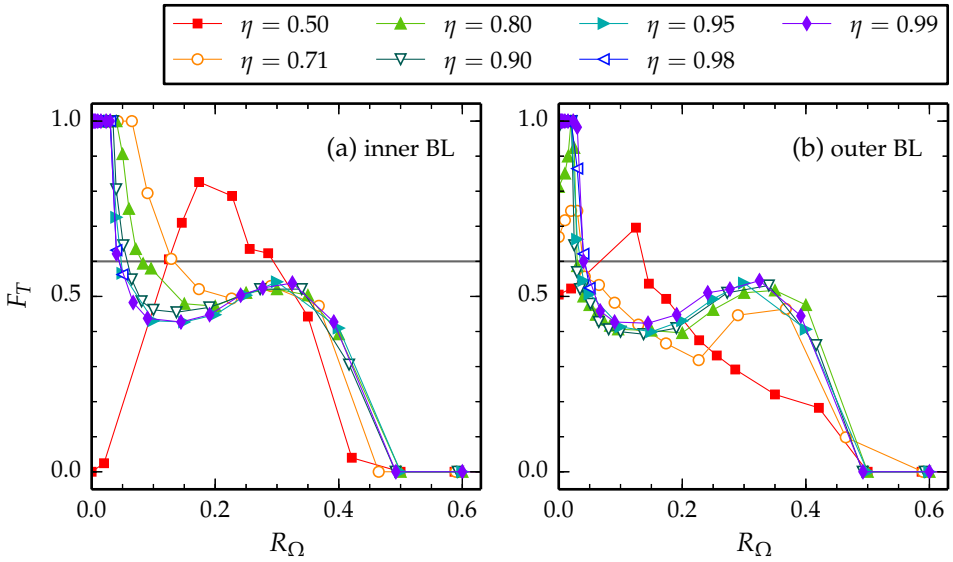

FIGURE 5.10: Axial fraction F_T of the BL that is covered by strongly turbulent regions with $\mathcal{L}_{\text{rms}} > 0.06$ (cf. Figure 5.8) for $Re_S = 2 \times 10^4$ and various radius ratios η. We estimate the onset of the transition to turbulent BLs by the rotation number $R_{\Omega,T}$ at which F_T exceeds the threshold 0.6 (horizontal line) for $R_\Omega < R_{\Omega,T}$.

ingly turbulent BLs. For $R_\Omega < 0.03$, the exponent exceeds the marginal stability prediction $\alpha = 5/3$ and accordingly indicates the torque scaling of a flow with completely turbulent BLs.

In summary, both the turbulent fraction F_T and the scaling exponent α prove the transition to turbulent BLs for $R_\Omega < 0.07$ that was hypothesised by the improved model. This transition takes place in a small rotation-number range ($0.03 < R_\Omega < 0.07$), and it rationalises the emergence of the narrow torque maximum at $R_\Omega = 0.02$ with increasing Re_S.

turbulent fraction for various η

Finally, we complement our transition analysis by evaluating the turbulent fraction of both BLs also for the other radius ratios considered in this thesis, see Figure 5.10. For $R_\Omega \lesssim 0.4$, we observe a *transitional regime* with $F_T \approx 0.5$ also for the other radius ratios, and with decreasing R_Ω the turbulent fraction increases further. Only the wide-gap case $\eta = 0.5$, where the stabilising counter-rotation occurs already for $R_\Omega < 0.5$, deviates from this behaviour. As intermittent bursts appear in the outer region for η considerably below 1 and small rotation numbers, the outer turbulent fraction decreases again for $\eta \leq 0.8$. We characterise the onset of the transition to turbulent BLs with decreasing R_Ω by the critical rotation number $R_{\Omega,T}$ at which the turbulent fraction F_T reaches the threshold 0.6 (horizontal line). Figure 5.10(a) reveals that for smaller radius ratios the transition in the inner BL occurs already at a larger rotation number. The variation of $R_{\Omega,T}$ with η is less for the outer BL, cf. Figure 5.10(b). As a result, the critical values $R_{\Omega,T}$ for the transition differ between both BLs for $\eta < 1$.

5.4 SUMMARY AND DISCUSSION

The modelling of mean profiles from a turbulent flow using marginal stability arguments was previously successfully applied to thermal convection (Malkus, 1954) and to TCF with stationary outer cylinder (King *et al.*, 1984; Marcus, 1984b; Barcilon & Brindley, 1984). While we here adopt the modelling arguments by King *et al.* (1984) and Marcus (1984b), some modifications were needed to generalise the marginal stability model to the case of independently rotating cylinders: As a first difference, instead of assuming a constant angular momentum in the central region, the present model incorporates the small positive angular momentum gradient that was observed in simulations and experiments. With this choice, the model predictions for large R_Ω differ less from the DNS results, but this slope value turned out to be non-essential for the correct rotation-number dependence. The second modification consists in the introduction of the increased effective gap widths $d_i = \widetilde{a}\delta_i$ and $d_o = \widetilde{a}\delta_o$, with $\widetilde{a} = 1.5$, for the TC Reynolds numbers of the BLs. The constant $\widetilde{a}$ accounts for the enlarged space due to a free-surface-like boundary condition at the BL edge. Its value was kept fixed for all η and R_Ω. The previous model without the factor $\widetilde{a}$ underestimated the measured torques, as the comparison by Lathrop, Fineberg & Swinney (1992a) showed. Finally, as the marginal stability condition for both BLs, we here utilise an analytic formula that determines the TC stability boundary in the whole parameter space (Esser & Grossmann, 1996). In particular, this stability formula also applies to the wide-gap case and to the situation of counter-rotating cylinders, in contrast to approximate stability conditions used by King *et al.* (1984) and Chandrasekhar (1961). However, for $\eta \to 1$ and co-rotating cylinders, these approximations coincide with the stability boundary by Esser & Grossmann (1996) and therefore produce the same marginal stability results in this parameter range.

The simplifications of the model helped us to interpret the rotation dependence of the torque at $Re_S = 2 \times 10^4$: While the broad maximum can be explained by marginal stability of both the central region and the BLs, the narrow torque maximum is related to turbulent BLs that enhance the angular momentum transport. Our simulations revealed that the marginal stability assumption of laminar BLs is most justified for $R_\Omega \geq 0.5$ and that a *transitional regime*, where laminar and turbulent regions in the BL coexist, occurs for $0.07 < R_\Omega < 0.4$. As the improved model that incorporates a shear transition suggests, the BLs become completely turbulent for R_Ω below 0.07. Remarkably, this demonstrates that the transition to turbulent BLs does not only depend on the shear strength (Re_S) as previously observed (Lathrop, Fineberg & Swinney, 1992a,b; Lewis & Swinney, 1999; Ostilla-Mónico *et al.*, 2014b), but also on the system rotation, as also evidenced by the R_Ω-dependence of the BL Reynolds numbers Re^i_{BL} and Re^o_{BL}. Moreover, the results for $\eta = 0.9$ reveal that the transition to turbulent BLs additionally depends on the wall curvature: At the convex inner cylinder,

the transition occurs earlier (i.e. at a smaller critical value Re_T and a larger R_Ω) than at the concave outer cylinder. We expect this curvature effect to become more pronounced for smaller radius ratios.

Previously, Lathrop, Fineberg & Swinney (1992a) observed that the torque scaling exponent $\alpha = 5/3$, predicted by marginal stability in the limit of large Re_S (King *et al.*, 1984; Marcus, 1984b), is incompatible with torque measurements showing a continuous variation of α with Re_S even in the regime of laminar BLs. Our calculations revealed that the exponent α predicted by marginal stability also varies with R_Ω and Re_S (not shown here) even at Re_S as high as 10^4. As a consequence of this transitional behaviour, the predicted α lies significantly below the asymptotic limit $\alpha = 5/3$, in agreement with the torque computations in the regime of laminar BLs for $R_\Omega > 0.5$. Surprisingly, the observed torque scaling exponent falls below the marginal stability prediction in the regime where laminar and turbulent regions in the BL coexist. It remains unclear how a mixture of laminar and turbulent BL regions creates a slower than laminar effective torque scaling. However, the observed α clearly exceeds the marginal stability limit $5/3$ in the regime where the BLs are completely covered with turbulence.

We here investigated the torque and BL behaviour in low-curvature TCF for $\eta \geq 0.9$. We expect that the application of the marginal stability model to TCF with $\eta < 0.9$ underlies some limitations. Already the larger discrepancies between model and DNS for $\eta = 0.9$ suggest that curvature effects become relevant for $\eta < 0.9$. Since then the inner BL becomes earlier turbulent (i.e. at a higher critical rotation number $R_{\Omega,T}$, cf. Figure 5.10(a)), the marginal stability assumptions can only apply for large rotation numbers $R_\Omega > R_{\Omega,T}$. More importantly, the marginal stability model does not account for the intermittent bursting behaviour observed in the outer flow region for strongly counter-rotating cylinders (cf. Section 3.1): Since the flow switches over time between quiescent and highly turbulent phases, the assumption of one marginally stable state is inadequate here. The intermittent behaviour gains in importance with decreasing η, because the bursting becomes stronger (cf. Section 4.2) and occurs in a wider rotation-number range since the regime of counter-rotating cylinders corresponds to $-(1-\eta)/\eta < R_\Omega < 1-\eta$.

6 SUMMARY AND CONCLUSIONS

System rotation and wall curvature influence wall-bounded shear flows. In this thesis, we studied the effects of rotation and curvature on the turbulence and angular momentum transport in the flow between two rotating cylinders. For this purpose, DNS of turbulent TCF were performed in a wide parameter range, which enable the investigation of a variety of general turbulent phenomena, such as intermittent bursts, large-scale structures, turbulent mixing and BL transitions. In addition, we introduced simplified models to explain the simulation results and to identify key physical mechanisms that govern the complicated turbulent flow.

validation of simulation approach

After describing the numerical scheme, we validated our simulation approach in Chapter 2. The analysis of convergence with increasing spatial resolution revealed that the numerical results become resolution-independent when the relative amplitudes of the highest modes decay to $\sim 10^{-4}$. Then, the deviation from the energy balance drops to 0.1%, and the agreement of torque values at the inner and outer cylinder is fulfilled within the statistical uncertainty, which serve as two additional convergence criteria. All presented simulations satisfy these criteria, which for the test case result in converged torque values, converged mean and RMS velocity profiles and the fulfilment of the radial independence of the current J^ω to within 0.1%. In addition, it was shown that our simulations in small domains of length $L_\varphi \approx 3$ and height $L_z = 2$ reproduce the rotation dependence of torques observed in much larger TC experiments. The computational domain can accommodate a single Taylor vortex pair. We tested that simulating more vortex pairs of the same size or longer domains does not significantly change the mean torque and the velocity profile and only slightly influences the fluctuations. Moreover, comparisons to torque measurements for Re_S between 10^5 and 10^6 show that our numerical results for $Re_S = 2 \times 10^4$ already capture the beginning of the general turbulent behaviour observed at much higher Reynolds numbers.

turbulent bursts

In Chapter 3, we investigated the phenomenon of turbulent bursts that occur in the outer flow region when the latter is stabilised by a sufficient counter-rotation of the outer cylinder. In contrast to the permanently turbulent inner region, the outer region changes between turbulent and quiescent phases, which reduce the angular momentum transport. For constant shear $Re_S = 2 \times 10^4$ and changing mean rotation (μ), the bursting onset μ_c was found to coincide with a torque maximum at counter-rotation for radius ratios $\eta \leq 0.8$. The simulation results show that this torque-maximisation can be explained by a strengthening of Taylor vortices with the onset of counter-rotation and a weakening of vortices when the bursts occur for stronger counter-rotation. This connection between Taylor vor-

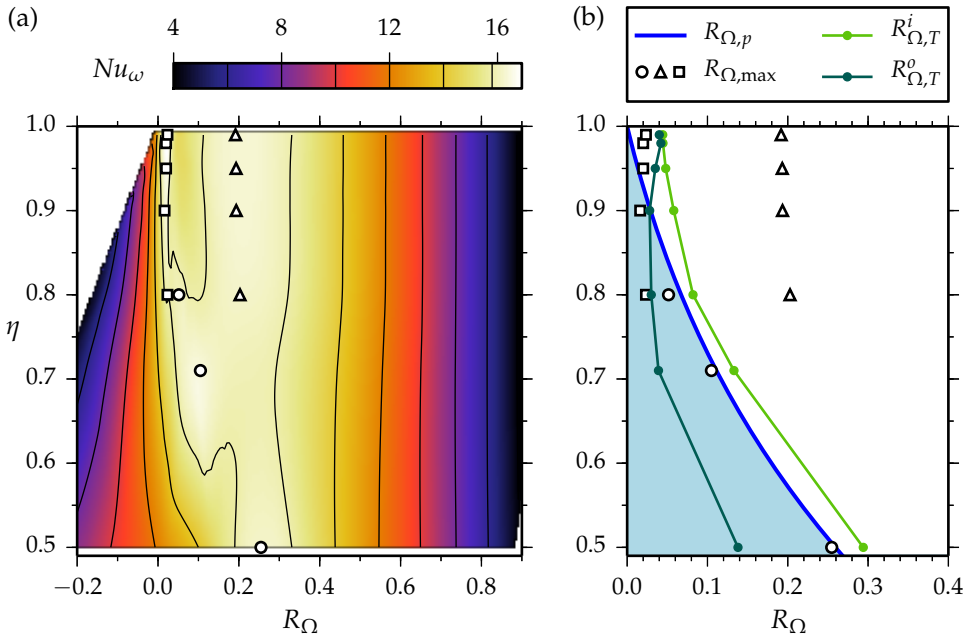

FIGURE 6.1: Overview of torque and BL results for $Re_S = 2 \times 10^4$. (a) Variation of the torque (Nu_ω) with rotation (R_Ω) and curvature (η). (b) Boundaries between flow regimes. Turbulent bursts occur in the parameter region marked in blue, where $R_{\Omega,p}$ corresponds to the prediction μ_p from (3.10). In the DNS, inner and outer BLs become turbulent for $R_\Omega < R^i_{\Omega,T}$ and $R_\Omega < R^o_{\Omega,T}$, respectively, as analysed in Figure 5.10. The circles, triangles and squares in (a,b) indicate the locations $R_{\Omega,\max}$ of the detachment, broad and narrow torque maxima.

tices, bursts and the angular momentum transport resulted in the prediction $\mu_p(\eta)$ for the bursting onset, which is in good agreement with the empirically identified onsets μ_c. In addition, $\mu_p(\eta)$ predicts the location of the corresponding detachment torque maximum, see circles in Figure 6.1. However, both the bursting and the prediction rely on the partitioning of the flow into an unstable inner and a stabilised outer region, which disappears for $\eta \to 1$. Our analysis in Section 4.2 revealed that the radial difference in stability and the strength of bursting continuously decrease with increasing η, and that both effects eventually vanish for $\eta = 1$. As a consequence, the prediction $\mu_p(\eta)$ does not apply for $\eta \gtrsim 0.9$. Moreover, the bursting regime recedes to $R_\Omega \to 0$, as shown in Figure 6.1(b).

limit of vanishing curvature

In Chapter 4, we explored the limit of vanishing curvature for $\eta \to 1$, where TCF approximates RPCF. To study the continuous transition between both systems, we described TCF in the rotating reference frame introduced by Dubrulle *et al.* (2005), so that shear and mean system rotation are measured by the same parameters Re_S and R_Ω in both systems. Furthermore, we analysed the angular momentum transport in TCF and linear momentum transport in RPCF in a common framework. Our study revealed that the simulation results for various radius ratios $\eta \geq 0.9$ and for RPCF collapse as a function of R_Ω, demonstrating that the turbulent behaviour of TCF with small but finite curvature already converges to the one of RPCF.

We observed this agreement in the Nusselt numbers, profile slopes, fluctuation amplitudes and angular momentum profiles of TCF. Effects of the curvature manifest themselves as a variation of the results with η, which only occurs in the bursting regime for $R_\Omega < R_{\Omega,p}$. The data collapse observed for $R_\Omega > R_{\Omega,p}$ additionally demonstrates that Re_S and R_Ω are the appropriate parameters to largely suppress the effect of geometry. Furthermore, we showed that for $R_\Omega > 0$ the turbulent mixing of momentum results in angular velocity (TCF) and velocity (RPCF) profiles with a residual gradient in the centre that can be explained by inviscid neutral stability. Remarkably, the limit of vanishing curvature entails more changes than anticipated, most notably the transition from a single torque maximum to two maxima for $\eta \gtrsim 0.9$, a broad and a narrow one, see Figure 6.1(a).

marginal stability and broad maximum

To explain the new rotation dependence of low-curvature TCF and the physical mechanisms behind the two torque maxima, we introduced a marginal stability model in Chapter 5, which extends a previous model for TCF with stationary outer cylinder (King *et al.*, 1984; Marcus, 1984b) to the case of independently rotating cylinders. Most importantly, both BLs are modelled as marginally stable TCFs with one free-surface-like boundary condition at the BL edge. A comparison between model prediction and simulation results for $\eta = 0.9, 0.99$ and $Re_S = 2 \times 10^4$ revealed that marginal stability explains the rotation dependence of the BL thickness, central profile and torque in a wide R_Ω range. In particular, the model reproduces the broad torque maximum at $R_\Omega = 0.2$, which is consistent with our observation that this maximum also occurs in streamwise-invariant simulations because the marginal stability assumptions apply there as well. The full simulations additionally show that the broad torque maximum is connected with a strong vortical flow. Furthermore, our model captures finite-Re_S effects. As a result, the torque scaling exponent α predicted for $Re_S \sim 10^4$ falls below the asymptotic marginal stability prediction $\alpha = 5/3$, in qualitative agreement with the DNS results for $R_\Omega \gtrsim 0.4$.

BL transition and narrow maximum

However, the model prediction strongly deviates from the simulation results for $R_\Omega \lesssim 0.07$ and does not reproduce the narrow torque maximum at $R_\Omega = 0.02$. This discrepancy was explained by a transition to turbulent BLs which bypasses their linear stability. An improved model suggests that the narrow torque maximum for $\eta \geq 0.9$ results from a transition to turbulent BLs for $R_\Omega < 0.07$, which increases the angular momentum transport. This explanation is consistent with our observation that the narrow maximum only emerges with increasing Re_S and that it does not occur in streamwise-invariant simulations where three-dimensional BL instabilities are absent. In addition, the narrow maximum coincides with an efficient angular momentum transport by the mean vortical flow. Our simulation results confirm that the BLs become turbulent for R_Ω below the critical values $R_{\Omega,T}$ shown in Figure 6.1(b). This reveals that the BL transition in TCF does not only depend on the shear strength but also on the system rotation (R_Ω). Moreover, it is influenced by the wall curvature since $R_{\Omega,T}$ varies with η and differs between the BLs of the convex inner and concave

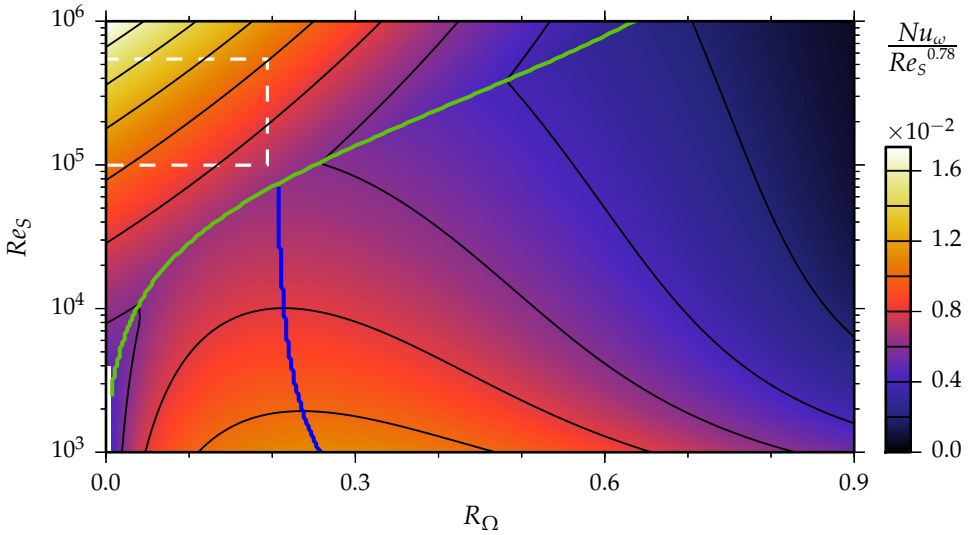

FIGURE 6.2: Extrapolation of the model prediction for $\eta = 0.99$ to higher Re_S. The torques are calculated with the improved marginal stability model from Section 5.3, which predicts turbulent BLs for Re_S above the transition boundary (green line). The blue line indicates the location of the broad torque maximum. The parameter region (dashed rectangle) explored in the Twente experiment with $\eta = 0.909$ is located entirely in the regime of turbulent BLs.

outer cylinder for $\eta < 1$. Interestingly, the transition to a turbulent inner BL also precedes the detachment torque maximum, but not the broad maximum for $\eta \geq 0.8$. Furthermore, a special constellation occurs for $\eta = 0.8$: With decreasing R_Ω, first the inner BL becomes turbulent giving rise to the detachment torque maximum. Then, the bursting decreases the torque, and the transition to a turbulent outer BL increases the torque again. Thus, a second maximum forms. For $\eta = 0.5$ and 0.71, the outer BL transition presumably lies too deep inside the bursting regime to cause a second maximum. Finally, for $R_{\Omega,T} < R_\Omega < 0.4$ we found a *transitional regime*, where the interaction with strong Taylor vortices results in a coexistence of laminar and turbulent regions in both BLs.

6.1 OUTLOOK

Overall, this study has explained various phenomena in turbulent TCF. On the other hand, the results raise interesting questions for future investigations. An intriguing observation is that the BL Reynolds number Re_{BL} depends on the system rotation, cf. Figure 5.7. As the BL Reynolds numbers increase with Re_S (i.e. the $Re_{\mathrm{BL}}(R_\Omega)$ curves in Figure 5.7 shift upwards), they exceed the transition threshold Re_T already at a larger critical value $R_{\Omega,T}$, and thus the BLs become turbulent in a wider rotation-number range. This is demonstrated for $\eta = 0.99$ in Figure 6.2, where the prediction of the improved model is calculated up to $Re_S = 10^6$ by assuming that the transition Reynolds number $Re_T = 310$ does not depend on R_Ω or Re_S. The model reveals that the critical value of Re_S for the BL transition in-

creases with R_Ω and that the broad torque maximum will disappear near $Re_S \approx 7 \times 10^4$ after the BL transition. Moreover, in the simulations, the narrow torque maximum grows faster with Re_S (cf. Figure 5.9(b)), which also suggests that it will eventually outperform the broad maximum. Torques from the Twente experiment with $\eta = 0.909$ and $Re_S \geq 10^5$ (Ostilla-Mónico *et al.*, 2014a) indeed show only a single maximum at $R_\Omega = 0.04$ close to the value $R_\Omega = 0.02$ found here (cf. Figure 4.6(a)). The experimentally explored parameter region is entirely in the regime where turbulent BLs are predicted, as shown in Figure 6.2. However, our model suggests that at these $Re_S \geq 10^5$ a regime of laminar BLs still exists for larger rotation numbers, e.g. $R_\Omega > 0.5$. Further simulations or experiments could test this prediction, the transformation of the broad maximum with increasing Re_S and the predicted boundary for the transition to turbulent BLs. Furthermore, the BL-transition boundaries for smaller radius ratios will additionally differ between the inner and outer cylinder, as they do for $Re_S = 2 \times 10^4$ in Figure 6.1(b). Thus, the influence of curvature on the turbulence transition in the BL can be further analysed.

Chapter 5 showed that marginal stability correctly reproduces the rotation dependence of torques in a wide range, but that the empirical factor $\widetilde{a} = 1.5$ (describing the increased effective BL width) is needed to match the overall magnitude of torques. Further studies will test whether this factor can be avoided in the marginal stability analysis by introducing improved models for the angular momentum profile and by considering the full linear stability equations derived from the Navier–Stokes equations (Lellep, 2015).

A

REANALYSIS OF WENDT'S TORQUE MEASUREMENTS*

Recent experimental studies analyse the dependence of torque on the shear rate and on the mean system rotation independently. This decomposition is advantageous since torques can be compensated either by dividing by the effective scaling with the shear (van Gils *et al.*, 2011) or by taking the ratio to $G(\mu = 0)$ (Dubrulle *et al.*, 2005; Paoletti & Lathrop, 2011) to study the rotation dependence. The resulting torque amplitudes are based on numerous measurements at different shear rates for each rotation ratio, which improves statistical significance. In contrast, Wendt presented the dependence of the torque on the rotation for some selected shear Reynolds numbers in figure 10 of Wendt (1933). Since this evaluation is based on single measurements, uncertainties may play a major role.

* This appendix has been published in H. J. Brauckmann & B. Eckhardt (2013b). Intermittent boundary layers and torque maxima in Taylor–Couette flow. *Phys. Rev. E* 87: 033004.

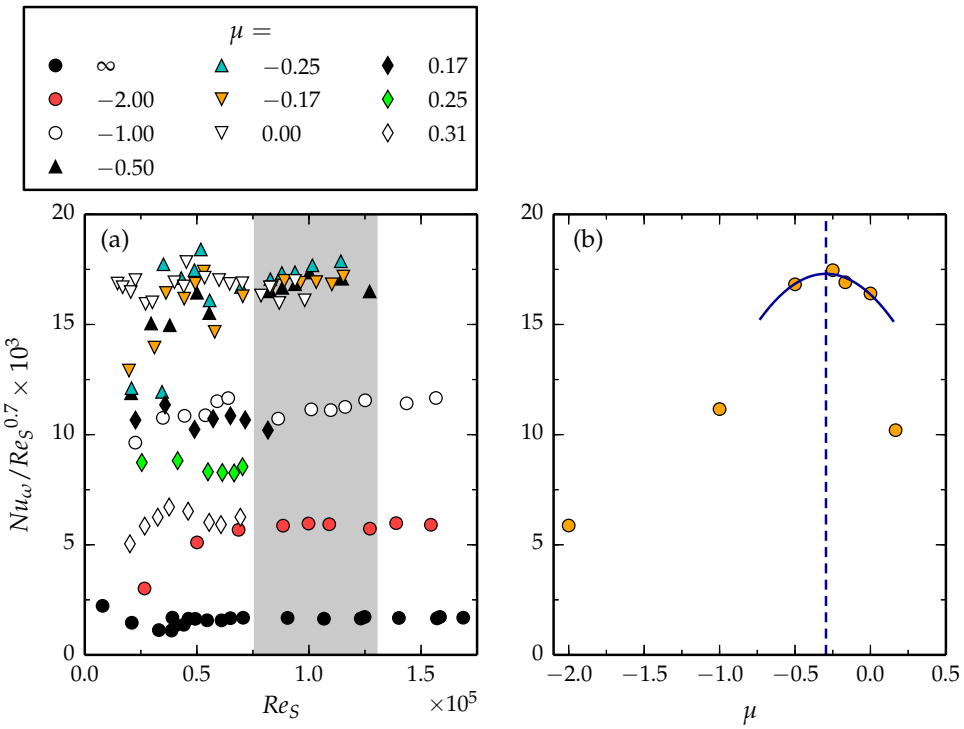

FIGURE A.1: Torques ($Nu_\omega = G/G_{\text{lam}}$) measured by Wendt (1933) for $\eta = 0.680$ compensated by the effective scaling $Nu_\omega \propto {Re_S}^{0.7}$ reported by Wendt. (a) Nu_ω versus Re_S for various rotation ratios μ. The compensated torques are independently averaged for each rotation ratio in the range $7.6 \times 10^4 < Re_S < 1.3 \times 10^5$ shaded in grey, resulting in the amplitudes shown in (b). The quadratic least-squares fit (solid line) to the four largest values in (b) has a maximum at $\mu_{\text{max}} = -0.295$ marked by the dashed line.

Therefore, we here apply the current analysis method to Wendt's torque measurements for $\eta = 0.680$ digitised from figure 9 in Wendt (1933). Figure A.1(a) shows the torques for various rotation ratios compensated by ${Re_S}^{0.7}$, which Wendt found as effective scaling for $10^4 \lesssim Re_S \lesssim 10^5$. One easily sees that the torque depends on the mean rotation with the largest values for high Re_S at $\mu = -0.25$. We closely follow the analysis in van Gils *et al.* (2011, 2012) and Paoletti & Lathrop (2011) and average the compensated torques in the range $7.6 \times 10^4 < Re_S < 1.3 \times 10^5$ to find amplitudes depending on the mean system rotation only, see Figure A.1(b). We chose this Reynolds-number range so that it starts after the shift of the torque maximum (Brauckmann & Eckhardt, 2013a) and just includes the highest data points for $-0.50 \leq \mu \leq 0.17$ (cf. Figure A.1(a)). One observes a maximum in the statistically more significant mean amplitudes for moderate counter-rotation, which was also found in recent studies (Paoletti & Lathrop, 2011; van Gils *et al.*, 2011, 2012) and in current simulations (Section 3.2). Based on a quadratic fit to the largest amplitudes, we find

$$\mu_{\max}(0.680) = -0.295 \pm 0.113, \tag{A.1}$$

with the uncertainty calculated in analogy to equation (3.4). Its relatively high level is due to the broad maximum in Figure A.1(b) and due to the few rotation ratios investigated by Wendt. In spite of the high uncertainty, the torque maximisation for counter-rotation, i.e. $\mu_{\max} < 0$, is clear without ambiguity. Moreover, the new maximum $\mu_{\max}(0.680) = -0.295$ lies consistently between the maxima for the neighbouring radius ratios $\mu_{\max}(0.5) = -0.195$ and $\mu_{\max}(0.71) = -0.361$ identified here, cf. equation (3.3).

BIBLIOGRAPHY

Ahlers, G., Bodenschatz, E., Funfschilling, D., Grossmann, S., He, X., Lohse, D., Stevens, R. J. A. M. & Verzicco, R. (2012). Logarithmic temperature profiles in turbulent Rayleigh–Bénard convection. *Phys. Rev. Lett.* 109: 114501 (cit. on p. 70).

Ahlers, G., Grossmann, S. & Lohse, D. (2009). Heat transfer and large scale dynamics in turbulent Rayleigh–Bénard convection. *Rev. Mod. Phys.* 81: 503–537 (cit. on pp. 45, 66).

Andereck, C. D., Liu, S. S. & Swinney, H. L. (1986). Flow regimes in a circular Couette system with independently rotating cylinders. *J. Fluid Mech.* 164: 155–183 (cit. on pp. 3, 4, 6, 35).

Andersson, P., Berggren, M. & Henningson, D. S. (1999). Optimal disturbances and bypass transition in boundary layers. *Phys. Fluids* 11: 134–150 (cit. on p. 90).

Avila, K. & Hof, B. (2013). High-precision Taylor–Couette experiment to study subcritical transitions and the role of boundary conditions and size effects. *Rev. Sci. Instrum.* 84: 065106 (cit. on p. 3).

Avila, M. (2008). *Nonlinear dynamics of mode competition in annular flows*. PhD thesis. Polytechnic University of Catalonia (cit. on pp. 15, 16).

Avila, M., Belisle, M. J., Lopez, J. M., Marques, F. & Saric, W. S. (2008). Mode competition in modulated Taylor–Couette flow. *J. Fluid Mech.* 601: 381–406 (cit. on p. 16).

Avila, M., Marques, F., Lopez, J. M. & Meseguer, A. (2007). Stability control and catastrophic transition in a forced Taylor–Couette system. *J. Fluid Mech.* 590: 471–496 (cit. on p. 16).

Avila, M., Meseguer, A. & Marques, F. (2006). Double Hopf bifurcation in corotating spiral Poiseuille flow. *Phys. Fluids* 18: 064101 (cit. on p. 16).

Avsarkisov, V., Hoyas, S., Oberlack, M. & García-Galache, J. P. (2014). Turbulent plane Couette flow at moderately high Reynolds number. *J. Fluid Mech.* 751: R1 (cit. on pp. 10, 11).

Barcilon, A. & Brindley, J. (1984). Organized structures in turbulent Taylor–Couette flow. *J. Fluid Mech.* 143: 429–449 (cit. on pp. 9, 10, 79, 93, 95).

Barcilon, A., Brindley, J., Lessen, M. & Mobbs, F. R. (1979). Marginal instability in Taylor–Couette flows at a very high Taylor number. *J. Fluid Mech.* 94: 453–463 (cit. on p. 35).

Barri, M. & Andersson, H. I. (2010). Computer experiments on rapidly rotating plane Couette flow. *Commun. Comput. Phys.* 7: 683–717 (cit. on p. 52).

Bech, K. H. & Andersson, H. I. (1997). Turbulent plane Couette flow subject to strong system rotation. *J. Fluid Mech.* 347: 289–314 (cit. on pp. 52, 73).

Bilson, M. & Bremhorst, K. (2007). Direct numerical simulation of turbulent Taylor–Couette flow. *J. Fluid Mech.* 579: 227–270 (cit. on pp. 29, 45, 75).

Blasius, H. (1908). Grenzschichten in Flüssigkeiten mit kleiner Reibung. *Z. Math. Phys.* 56: 1–37 (cit. on p. 10).

Boersma, B. J. (2015). Large scale motions in the direct numerical simulation of turbulent pipe flow. *Direct and Large-Eddy Simulation IX*. Springer, 243–249 (cit. on p. 11).

Borrero-Echeverry, D., Schatz, M. F. & Tagg, R. (2010). Transient turbulence in Taylor–Couette flow. *Phys. Rev. E* 81: 025301 (cit. on p. 3).

Bottin, S., Daviaud, F., Manneville, P. & Dauchot, O. (1998). Discontinuous transition to spatiotemporal intermittency in plane Couette flow. *Europhys. Lett.* 43: 171–176 (cit. on p. 3).

Boyd, J. P. (2000). *Chebyshev and Fourier spectral methods*. 2nd ed. Dover Publications (cit. on pp. 16, 18, 22).

Bradshaw, P. (1969). The analogy between streamline curvature and buoyancy in turbulent shear flow. *J. Fluid Mech.* 36: 177–191 (cit. on p. 71).

Brauckmann, H. J. (2011). *Torque calculations for Taylor–Couette flow*. Masters thesis. Philipps-Universität Marburg (cit. on pp. 18, 21, 24, 117).

Brauckmann, H. J. & Eckhardt, B. (2013a). Direct numerical simulations of local and global torque in Taylor–Couette flow up to $Re = 30\,000$. *J. Fluid Mech.* 718: 398–427 (cit. on pp. 3, 9, 11, 16, 20, 21, 24, 26, 28, 30, 31, 33, 35, 36, 40, 49, 52, 54, 65, 71, 104, 117).

Brauckmann, H. J. & Eckhardt, B. (2013b). Intermittent boundary layers and torque maxima in Taylor–Couette flow. *Phys. Rev. E* 87: 033004 (cit. on pp. 11, 27, 35, 38, 39, 51, 52, 60, 64–66, 68, 76, 79, 81, 103, 117).

Brauckmann, H. J. & Eckhardt, B. (2016). Marginally stable and turbulent boundary layers in low-curvature Taylor–Couette flow. *Manuscript in preparation* (cit. on p. 118).

Brauckmann, H. J., Salewski, M. & Eckhardt, B. (2016). Momentum transport in Taylor–Couette flow with vanishing curvature. *J. Fluid Mech.* 790: 419–452 (cit. on pp. 26, 51, 118).

Brethouwer, G., Duguet, Y. & Schlatter, P. (2012). Turbulent–laminar coexistence in wall flows with Coriolis, buoyancy or Lorentz forces. *J. Fluid Mech.* 704: 137–172 (cit. on pp. 10, 51).

Brethouwer, G., Schlatter, P., Duguet, Y., Henningson, D. S. & Johansson, A. V. (2014). Recurrent bursts via linear processes in turbulent environments. *Phys. Rev. Lett.* 112: 144502 (cit. on p. 11).

Brown, E. & Ahlers, G. (2007). Temperature gradients, and search for non-Boussinesq effects, in the interior of turbulent Rayleigh–Bénard convection. *Europhys. Lett.* 80: 14001 (cit. on p. 70).

Burin, M. J., Schartman, E. & Ji, H. (2010). Local measurements of turbulent angular momentum transport in circular Couette flow. *Exp. Fluids* 48: 763–769 (cit. on pp. 3, 75).

Busse, F. H. (1970). Bounds for turbulent shear flow. *J. Fluid Mech.* 41: 219–240 (cit. on p. 8).

Chandrasekhar, S. (1961). *Hydrodynamic and Hydromagnetic Stability*. 1st ed. Clarendon Press (cit. on pp. 11, 38, 42, 71, 79, 88, 95).

Coles, D. (1965). Transition in circular Couette flow. *J. Fluid Mech.* 21: 385–425 (cit. on pp. 3, 10, 24, 35).

Coles, D. (1967). A note on Taylor instability in circular Couette flow. *J. Appl. Mech.* 34: 529–534 (cit. on p. 5).

Colovas, P. W. & Andereck, C. D. (1997). Turbulent bursting and spatiotemporal intermittency in the counterrotating Taylor–Couette system. *Phys. Rev. E* 55: 2736–2741 (cit. on p. 35).

Couette, M. (1890). Études sur le frottement des liquides. *Ann. Chim. Phys., Ser. VI* 21: 433–510 (cit. on p. 2).

Coughlin, K. & Marcus, P. S. (1996). Turbulent bursts in Couette–Taylor flow. *Phys. Rev. Lett.* 77: 2214–2217 (cit. on pp. 11, 27, 35, 38, 42, 44).

Cox, S. M. & Matthews, P. C. (2002). Exponential time differencing for stiff systems. *J. Comput. Phys.* 176: 430–455 (cit. on p. 16).

Daly, C. A., Schneider, T. M., Schlatter, P. & Peake, N. (2014). Secondary instability and tertiary states in rotating plane Couette flow. *J. Fluid Mech.* 761: 27–61 (cit. on p. 6).

Daviaud, F., Hegseth, J. & Bergé, P. (1992). Subcritical transition to turbulence in plane Couette flow. *Phys. Rev. Lett.* 69: 2511–2514 (cit. on p. 3).

Demay, Y., Iooss, G. & Laure, P. (1992). Wave patterns in the small gap Couette–Taylor problem. *Eur. J. Mech. B/Fluids* 11: 621–634 (cit. on p. 6).

Doering, C. R. & Constantin, P. (1992). Energy dissipation in shear driven turbulence. *Phys. Rev. Lett.* 69: 1648–1651 (cit. on p. 8).

Doering, C. R. & Constantin, P. (1994). Variational bounds on energy dissipation in incompressible flows: Shear flow. *Phys. Rev. E* 49: 4087–4099 (cit. on p. 9).

Dong, S. (2007). Direct numerical simulation of turbulent Taylor–Couette flow. *J. Fluid Mech.* 587: 373–393 (cit. on pp. 17, 70, 83).

Dong, S. & Zheng, X. (2011). Direct numerical simulation of spiral turbulence. *J. Fluid Mech.* 668: 150–173 (cit. on p. 35).

Donnelly, R. J. (1991). Taylor–Couette flow: The early days. *Phys. Today* 44: 32–39 (cit. on p. 2).

Donnelly, R. J. & Fultz, D. (1960). Experiments on the stability of viscous flow between rotating cylinders. II. Visual observations. *Proc. R. Soc. London A* 258: 101–123 (cit. on pp. 43, 85).

Dubrulle, B. (1993). Differential rotation as a source of angular momentum transfer in the solar nebula. *Icarus* 106: 59–76 (cit. on p. 59).

Dubrulle, B., Dauchot, O., Daviaud, F., Longaretti, P.-Y., Richard, D. & Zahn, J.-P. (2005). Stability and turbulent transport in Taylor–Couette flow from analysis of experimental data. *Phys. Fluids* 17: 095103 (cit. on pp. 4–6, 9, 26, 33, 36, 54, 55, 62, 76, 79, 81, 82, 91, 98, 103).

Dubrulle, B. & Hersant, F. (2002). Momentum transport and torque scaling in Taylor–Couette flow from an analogy with turbulent convection. *Eur. Phys. J. B* 26: 379–386 (cit. on pp. 8, 9, 57).

Duguet, Y., Schlatter, P. & Henningson, D. S. (2010). Formation of turbulent patterns near the onset of transition in plane Couette flow. *J. Fluid Mech.* 650: 119–129 (cit. on p. 3).

Eckhardt, B., Grossmann, S. & Lohse, D. (2000). Scaling of global momentum transport in Taylor–Couette and pipe flow. *Eur. Phys. J. B* 18: 541–544 (cit. on p. 9).

Eckhardt, B., Grossmann, S. & Lohse, D. (2007a). Fluxes and energy dissipation in thermal convection and shear flows. *Europhys. Lett.* 78: 24001 (cit. on pp. 8, 57).

Eckhardt, B., Grossmann, S. & Lohse, D. (2007b). Torque scaling in turbulent Taylor–Couette flow between independently rotating cylinders. *J. Fluid Mech.* 581: 221–250 (cit. on pp. 7–9, 29, 42, 56).

Eckhardt, B. & Yao, D. (1995). Local stability analysis along Lagrangian paths. *Chaos, Solitons & Fractals* 5: 2073–2088 (cit. on pp. 59, 60).

Eckmann, J.-P. (1981). Roads to turbulence in disipative dynamical systems. *Rev. Mod. Phys.* 53: 643–654 (cit. on p. 3).

Esser, A. & Grossmann, S. (1996). Analytic expression for Taylor–Couette stability boundary. *Phys. Fluids* 8: 1814–1819 (cit. on pp. 6, 43, 79, 85, 86, 90, 95).

Faisst, H. & Eckhardt, B. (2000). Transition from the Couette–Taylor system to the plane Couette system. *Phys. Rev. E* 61: 7227–7230 (cit. on pp. 6, 48, 55).

Fardin, M. A., Perge, C. & Taberlet, N. (2014). "The hydrogen atom of fluid dynamics" – introduction to the Taylor–Couette flow for soft matter scientists. *Soft Matter* 10: 3523–3535 (cit. on p. 3).

Fenstermacher, P. R., Swinney, H. L. & Gollub, J. P. (1979). Dynamical instabilities and the transition to chaotic Taylor vortex flow. *J. Fluid Mech.* 94: 103–128 (cit. on p. 3).

Gibson, J. F. (2012). *Channelflow: A spectral Navier–Stokes simulator in C++*. Tech. rep. U. New Hampshire (cit. on p. 28).

Gibson, J. F., Halcrow, J. & Cvitanović, P. (2008). Visualizing the geometry of state space in plane Couette flow. *J. Fluid Mech.* 611: 107–130 (cit. on p. 28).

Goharzadeh, A. & Mutabazi, I. (2001). Experimental characterization of intermittency regimes in the Couette–Taylor system. *Eur. Phys. J. B* 19: 157–162 (cit. on p. 3).

Gol'dshtik, M. A., Sapozhnikov, V. A. & Shtern, V. N. (1970). Verification of the Malkus hypothesis regarding the stability of turbulent flows. *Fluid Dyn.* 5: 863–867 (cit. on p. 79).

Greidanus, A. J., Delfos, R., Tokgoz, S. & Westerweel, J. (2015). Turbulent Taylor–Couette flow over riblets: drag reduction and the effect of bulk fluid rotation. *Exp. Fluids* 56: 107 (cit. on p. 12).

Grossmann, S., Lohse, D. & Sun, C. (2014). Velocity profiles in strongly turbulent Taylor–Couette flow. *Phys. Fluids* 26: 025114 (cit. on p. 10).

Grossmann, S., Lohse, D. & Sun, C. (2016). High–Reynolds number Taylor–Couette turbulence. *Annu. Rev. Fluid Mech.* 48: 53–80 (cit. on p. 12).

Heinrichs, W. (1989). Improved condition number for spectral methods. *Math. Comput.* 53: 103–119 (cit. on p. 16).

Hersant, F., Dubrulle, B. & Huré, J.-M. (2005). Turbulence in circumstellar disks. *Astron. Astrophys.* 429: 531–542 (cit. on p. 6).

Hiwatashi, K., Alfredsson, P. H., Tillmark, N. & Nagata, M. (2007). Experimental observations of instabilities in rotating plane Couette flow. *Phys. Fluids* 19: 048103 (cit. on p. 6).

Hof, B., Westerweel, J., Schneider, T. M. & Eckhardt, B. (2006). Finite lifetime of turbulence in shear flows. *Nature* 443: 59–62 (cit. on p. 3).

Howard, L. N. (1966). Convection at high Rayleigh number. *Applied Mechanics*. Springer, 1109–1115 (cit. on pp. 10, 79, 83).

Huisman, S. G., Scharnowski, S., Cierpka, C., Kähler, C. J., Lohse, D. & Sun, C. (2013). Logarithmic boundary layers in strong Taylor–Couette turbulence. *Phys. Rev. Lett.* 110: 264501 (cit. on pp. 10, 23).

Huisman, S. G., van der Veen, R. C. A., Sun, C. & Lohse, D. (2014). Multiple states in highly turbulent Taylor–Couette flow. *Nat. Commun.* 5: 3820 (cit. on pp. 11, 24, 27, 35, 47, 66).

Hultmark, M., Vallikivi, M., Bailey, S. C. C. & Smits, A. J. (2012). Turbulent pipe flow at extreme Reynolds numbers. *Phys. Rev. Lett.* 108: 094501 (cit. on p. 10).

Jeong, J. & Hussain, F. (1995). On the identification of a vortex. *J. Fluid Mech.* 285: 69–94 (cit. on p. 37).

Jones, C. A. (1985). The transition to wavy Taylor vortices. *J. Fluid Mech.* 157: 135–162 (cit. on p. 15).

Kerr, R. M. (1996). Rayleigh number scaling in numerical convection. *J. Fluid Mech.* 310: 139–179 (cit. on p. 70).

King, G. P., Li, Y., Lee, W., Swinney, H. L. & Marcus, P. S. (1984). Wave speeds in wavy Taylor-vortex flow. *J. Fluid Mech.* 141: 365–390 (cit. on pp. 9, 10, 79, 83, 85, 89, 93, 95, 96, 99).

Kitoh, O. & Umeki, M. (2008). Experimental study on large-scale streak structure in the core region of turbulent plane Couette flow. *Phys. Fluids* 20: 025107 (cit. on p. 11).

Komminaho, J., Lundbladh, A. & Johansson, A. V. (1996). Very large structures in plane turbulent Couette flow. *J. Fluid Mech.* 320: 259–285 (cit. on p. 51).

Koschmieder, E. L. (1979). Turbulent Taylor vortex flow. *J. Fluid Mech.* 93: 515–527 (cit. on p. 35).

Koschmieder, E. L. (1993). *Bénard cells and Taylor vortices*. Cambridge University Press (cit. on pp. 3, 24, 35).

Landau, L. D. & Lifshitz, E. M. (1987). *Fluid Mechanics*. 2nd ed. Pergamon Press (cit. on pp. 4, 7, 17, 54).

Lathrop, D. P., Fineberg, J. & Swinney, H. L. (1992a). Transition to shear-driven turbulence in Couette–Taylor flow. *Phys. Rev. A* 46: 6390–6405 (cit. on pp. 3, 8, 9, 11, 26, 36, 65, 80, 93, 95, 96).

Lathrop, D. P., Fineberg, J. & Swinney, H. L. (1992b). Turbulent flow between concentric rotating cylinders at large Reynolds number. *Phys. Rev. Lett.* 68: 1515–1518 (cit. on pp. 3, 9, 36, 80, 93, 95).

Lellep, G. M. (2015). *Marginally stable velocity profiles in Taylor–Couette flow*. Bachelor thesis. Philipps-Universität Marburg (cit. on p. 101).

Lewis, G. S. & Swinney, H. L. (1999). Velocity structure functions, scaling, and transitions in high-Reynolds-number Couette–Taylor flow. *Phys. Rev. E* 59: 5457–5467 (cit. on pp. 3, 9, 11, 26, 30, 31, 65, 70, 73, 80, 82, 83, 93, 95).

Lezius, D. K. & Johnston, J. P. (1976). Roll-cell instabilities in rotating laminar and turbulent channel flows. *J. Fluid Mech.* 77: 153–175 (cit. on p. 6).

Malkus, W. V. R. (1954). The heat transport and spectrum of thermal turbulence. *Proc. R. Soc. London A* 225: 196–212 (cit. on pp. 10, 79, 83, 95).

Malkus, W. V. R. (1956). Outline of a theory of turbulent shear flow. *J. Fluid Mech.* 1: 521–539 (cit. on pp. 10, 79).

Malkus, W. V. R. (1983). The amplitude of turbulent shear flow. *Pure Appl. Geophys.* 121: 391–400 (cit. on p. 79).

Mallock, A. (1888). Determination of the viscosity of water. *Proc. R. Soc. London A* 45: 126–132 (cit. on p. 2).

Mallock, A. (1896). Experiments on fluid viscosity. *Philos. Trans. R. Soc. London A* 187: 41–56 (cit. on p. 2).

Marcus, P. S. (1984a). Simulation of Taylor–Couette flow. Part 1. Numerical methods and comparison with experiment. *J. Fluid Mech.* 146: 45–64 (cit. on pp. 7, 15, 17, 18, 56).

Marcus, P. S. (1984b). Simulation of Taylor–Couette flow. Part 2. Numerical results for wavy-vortex flow with one travelling wave. *J. Fluid Mech.* 146: 65–113 (cit. on pp. 9, 10, 79, 83, 89, 93, 95, 96, 99).

Martínez-Arias, B., Peixinho, J., Crumeyrolle, O. & Mutabazi, I. (2014). Effect of the number of vortices on the torque scaling in Taylor–Couette flow. *J. Fluid Mech.* 748: 756–767 (cit. on pp. 11, 65).

Merbold, S., Brauckmann, H. J. & Egbers, C. (2013). Torque measurements and numerical determination in differentially rotating wide gap Taylor–Couette flow. *Phys. Rev. E* 87: 023014 (cit. on pp. 3, 26, 30, 32, 33, 35, 41, 42, 48, 60, 65, 117).

Meseguer, A., Avila, M., Mellibovsky, F. & Marques, F. (2007). Solenoidal spectral formulations for the computation of secondary flows in cylindrical and annular geometries. *Eur. Phys. J. Spec. Top.* 146: 249–259 (cit. on p. 15).

Meseguer, A. & Mellibovsky, F. (2007). On a solenoidal Fourier–Chebyshev spectral method for stability analysis of the Hagen–Poiseuille flow. *Appl. Numer. Math.* 57: 920–938 (cit. on pp. 15, 16).

Meseguer, A., Mellibovsky, F., Avila, M. & Marques, F. (2009a). Families of subcritical spirals in highly counter-rotating Taylor–Couette flow. *Phys. Rev. E* 79: 036309 (cit. on p. 16).

MESEGUER, A., MELLIBOVSKY, F., AVILA, M. & MARQUES, F. (2009b). Instability mechanisms and transition scenarios of spiral turbulence in Taylor–Couette flow. *Phys. Rev. E* 80: 046315 (cit. on pp. 3, 16, 35).

MESEGUER, A. & TREFETHEN, L. N. (2003). Linearized pipe flow to Reynolds number 10^7. *J. Comput. Phys.* 186: 178–197 (cit. on p. 15).

MONTY, J. P., STEWART, J. A., WILLIAMS, R. C. & CHONG, M. S. (2007). Large-scale features in turbulent pipe and channel flows. *J. Fluid Mech.* 589: 147–156 (cit. on p. 11).

MOSER, R. D., MOIN, P. & LEONARD, A. (1983). A spectral numerical method for the Navier–Stokes equations with applications to Taylor–Couette flow. *J. Comput. Phys.* 52: 524–544 (cit. on p. 15).

NAGATA, M. (1986). Bifurcations in Couette flow between almost corotating cylinders. *J. Fluid Mech.* 169: 229–250 (cit. on pp. 5, 6).

NAGATA, M. (1990). Three-dimensional finite-amplitude solutions in plane Couette flow: bifurcation from infinity. *J. Fluid Mech.* 217: 519–527 (cit. on p. 6).

NICODEMUS, R., GROSSMANN, S. & HOLTHAUS, M. (1997a). Variational bound on energy dissipation in plane Couette flow. *Phys. Rev. E* 56: 6774–6786 (cit. on p. 9).

NICODEMUS, R., GROSSMANN, S. & HOLTHAUS, M. (1997b). Variational bound on energy dissipation in turbulent shear flow. *Phys. Rev. Lett.* 79: 4170–4173 (cit. on p. 9).

OERTEL, H., ed. (2010). *Prandtl-Essentials of Fluid Mechanics*. Vol. 158. Applied Mathematical Sciences. Springer New York (cit. on p. 79).

ORSZAG, S. A. & ISRAELI, M. (1974). Numerical simulation of viscous incompressible flows. *Annu. Rev. Fluid Mech.* 6: 281–318 (cit. on p. 22).

OSTILLA, R., STEVENS, R. J. A. M., GROSSMANN, S., VERZICCO, R. & LOHSE, D. (2013). Optimal Taylor–Couette flow: direct numerical simulations. *J. Fluid Mech.* 719: 14–46 (cit. on pp. 5, 9, 18, 26, 30–32, 40, 49, 52, 54, 71).

OSTILLA-MÓNICO, R., HUISMAN, S. G., JANNINK, T. J. G., VAN GILS, D. P. M., VERZICCO, R., GROSSMANN, S., SUN, C. & LOHSE, D. (2014a). Optimal Taylor–Couette flow: radius ratio dependence. *J. Fluid Mech.* 747: 1–29 (cit. on pp. 48, 51, 52, 63–65, 73, 77, 101).

OSTILLA-MÓNICO, R., VAN DER POEL, E. P., VERZICCO, R., GROSSMANN, S. & LOHSE, D. (2014b). Boundary layer dynamics at the transition between the classical and the ultimate regime of Taylor–Couette flow. *Phys. Fluids* 26: 015114 (cit. on pp. 80, 92, 93, 95).

OSTILLA-MÓNICO, R., VAN DER POEL, E. P., VERZICCO, R., GROSSMANN, S. & LOHSE, D. (2014c). Exploring the phase diagram of fully turbulent Taylor–Couette flow. *J. Fluid Mech.* 761: 1–26 (cit. on pp. 3, 27, 47, 66).

Ostilla-Mónico, R., Verzicco, R. & Lohse, D. (2015). Effects of the computational domain size on direct numerical simulations of Taylor–Couette turbulence with stationary outer cylinder. *Phys. Fluids* 27: 025110 (cit. on pp. 24, 25, 28).

Paoletti, M. S. & Lathrop, D. P. (2011). Angular momentum transport in turbulent flow between independently rotating cylinders. *Phys. Rev. Lett.* 106: 024501 (cit. on pp. 3, 9, 26, 33–36, 40, 41, 45, 48, 62, 103, 104).

Paoletti, M. S., van Gils, D. P. M., Dubrulle, B., Sun, C., Lohse, D. & Lathrop, D. P. (2012). Angular momentum transport and turbulence in laboratory models of Keplerian flows. *Astron. Astrophys.* 547: A64 (cit. on pp. 26, 33, 55, 62, 81).

Pirrò, D. & Quadrio, M. (2008). Direct numerical simulation of turbulent Taylor–Couette flow. *Eur. J. Mech. B/Fluids* 27: 552–566 (cit. on p. 29).

Pope, S. B. (2000). *Turbulent flows*. Cambridge University Press (cit. on pp. 10, 57).

Prandtl, L. (1905). Über Flüssigkeitsbewegung bei sehr kleiner Reibung. *Verhandlungen des III. Int. Math. Kongress, Heidelberg 1904*. B. G. Teubner, 484–491 (cit. on p. 10).

Prigent, A., Grégoire, G., Chaté, H. & Dauchot, O. (2003). Long-wavelength modulation of turbulent shear flows. *Physica D* 174: 100–113 (cit. on p. 3).

Prigent, A., Grégoire, G., Chaté, H., Dauchot, O. & van Saarloos, W. (2002). Large-scale finite-wavelength modulation within turbulent shear flows. *Phys. Rev. Lett.* 89: 014501 (cit. on p. 3).

Racina, A. & Kind, M. (2006). Specific power input and local micromixing times in turbulent Taylor–Couette flow. *Exp. Fluids* 41: 513–522 (cit. on pp. 30, 31).

Ravelet, F., Delfos, R. & Westerweel, J. (2010). Influence of global rotation and Reynolds number on the large-scale features of a turbulent Taylor–Couette flow. *Phys. Fluids* 22: 055103 (cit. on pp. 3, 11, 47, 51, 55, 62, 68).

Rayleigh, L. (1917). On the dynamics of revolving fluids. *Proc. R. Soc. London A* 93: 148–154 (cit. on pp. 42, 71, 82, 84).

Reynolds, W. C. & Hussain, A. K. M. F. (1972). The mechanics of an organized wave in turbulent shear flow. Part 3. Theoretical models and comparisons with experiments. *J. Fluid Mech.* 54: 263–288 (cit. on p. 66).

Reynolds, W. C. & Tiederman, W. G. (1967). Stability of turbulent channel flow, with application to Malkus's theory. *J. Fluid Mech.* 27: 253–272 (cit. on p. 79).

Riecke, H. & Paap, H.-G. (1986). Stability and wave-vector restriction of axisymmetric Taylor vortex flow. *Phys. Rev. A* 33: 547–553 (cit. on p. 24).

Rincon, F., Ogilvie, G. I. & Cossu, C. (2007). On self-sustaining processes in Rayleigh-stable rotating plane Couette flows and subcritical transition to turbulence in accretion disks. *Astron. Astrophys.* 463: 817–832 (cit. on p. 6).

Ruelle, D. & Takens, F. (1971). On the nature of turbulence. *Commun. Math. Phys.* 20: 167–192 (cit. on p. 3).

Salewski, M. & Eckhardt, B. (2015). Turbulent states in plane Couette flow with rotation. *Phys. Fluids* 27: 045109 (cit. on pp. 8, 28, 58, 62, 65).

Schlichting, H. & Gersten, K. (2006). *Grenzschicht-Theorie*. 10th ed. Springer (cit. on pp. 10, 80, 90).

Schmid, P. J. & Henningson, D. S. (2001). *Stability and Transition in Shear Flows*. Vol. 142. Applied Mathematical Sciences. Springer (cit. on p. 90).

Schultz, M. P. & Flack, K. A. (2013). Reynolds-number scaling of turbulent channel flow. *Phys. Fluids* 25: 025104 (cit. on pp. 9, 10).

Shi, L., Avila, M. & Hof, B. (2013). Scale invariance at the onset of turbulence in Couette flow. *Phys. Rev. Lett.* 110: 204502 (cit. on p. 3).

Smith, G. P. & Townsend, A. A. (1982). Turbulent Couette flow between concentric cylinders at large Taylor numbers. *J. Fluid Mech.* 123: 187–217 (cit. on pp. 10, 69, 73, 82, 83).

Smits, A. J., McKeon, B. J. & Marusic, I. (2011). High–Reynolds number wall turbulence. *Annu. Rev. Fluid Mech.* 43: 353–375 (cit. on p. 11).

Stevens, R. J. A. M., Verzicco, R. & Lohse, D. (2010). Radial boundary layer structure and Nusselt number in Rayleigh–Bénard convection. *J. Fluid Mech.* 643: 495–507 (cit. on p. 18).

Suryadi, A., Segalini, A. & Alfredsson, P. H. (2014). Zero absolute vorticity: Insight from experiments in rotating laminar plane Couette flow. *Phys. Rev. E* 89: 033003 (cit. on pp. 52, 72, 73).

Swinney, H. L. & Gollub, J. P. (1978). The transition to turbulence. *Phys. Today* 31: 41–49 (cit. on p. 3).

Taylor, G. I. (1923). Stability of a viscous liquid contained between two rotating cylinders. *Philos. Trans. R. Soc. London A* 223: 289–343 (cit. on pp. 2, 4, 24, 43, 79, 85).

Taylor, G. I. (1935). Distribution of velocity and temperature between concentric rotating cylinders. *Proc. R. Soc. London A* 151: 494–512 (cit. on pp. 69, 71, 82, 83).

Tilgner, A., Belmonte, A. & Libchaber, A. (1993). Temperature and velocity profiles of turbulent convection in water. *Phys. Rev. E* 47: R2253 (cit. on p. 70).

Tillmark, N. & Alfredsson, P. H. (1992). Experiments on transition in plane Couette flow. *J. Fluid Mech.* 235: 89–102 (cit. on p. 3).

Tokgöz, S. (2014). *Coherent structures in Taylor–Couette flow: Experimental investigation*. PhD thesis. Delft University of Technology (cit. on p. 11).

Tokgoz, S., Elsinga, G. E., Delfos, R. & Westerweel, J. (2012). Spatial resolution and dissipation rate estimation in Taylor–Couette flow for tomographic PIV. *Exp. Fluids* 53: 561–583 (cit. on p. 4).

Tong, P., Goldburg, W. I., Huang, J. S. & Witten, T. A. (1990). Anisotropy in turbulent drag reduction. *Phys. Rev. Lett.* 65: 2780–2783 (cit. on p. 12).

Tritton, D. J. (1992). Stabilization and destabilization of turbulent shear flow in a rotating fluid. *J. Fluid Mech.* 241: 503–523 (cit. on p. 71).

Tsukahara, T. (2011). Structures and turbulent statistics in a rotating plane Couette flow. *J. Phys. Conf. Ser.* 318: 022024 (cit. on pp. 51, 52).

Tsukahara, T., Tillmark, N. & Alfredsson, P. H. (2010). Flow regimes in a plane Couette flow with system rotation. *J. Fluid Mech.* 648: 5–33 (cit. on p. 6).

Tuckerman, L. S., Kreilos, T., Schrobsdorff, H., Schneider, T. M. & Gibson, J. F. (2014). Turbulent-laminar patterns in plane Poiseuille flow. *Phys. Fluids* 26: 114103 (cit. on p. 3).

Van Atta, C. (1966). Exploratory measurements in spiral turbulence. *J. Fluid Mech.* 25: 495–512 (cit. on pp. 3, 10, 35).

Van den Berg, T. H., Luther, S., Lathrop, D. P. & Lohse, D. (2005). Drag reduction in bubbly Taylor–Couette turbulence. *Phys. Rev. Lett.* 94: 044501 (cit. on p. 12).

Van den Berg, T. H., van Gils, D. P. M., Lathrop, D. P. & Lohse, D. (2007). Bubbly turbulent drag reduction is a boundary layer effect. *Phys. Rev. Lett.* 98: 084501 (cit. on p. 12).

Van Driest, E. R. & Blumer, C. B. (1963). Boundary layer transition: Freestream turbulence and pressure gradient effects. *AIAA J.* 1: 1303–1306 (cit. on p. 90).

Van Gils, D. P. M., Huisman, S. G., Bruggert, G.-W., Sun, C. & Lohse, D. (2011). Torque scaling in turbulent Taylor–Couette flow with co- and counterrotating cylinders. *Phys. Rev. Lett.* 106: 024502 (cit. on pp. 3, 9, 26, 33, 35, 36, 40, 54, 62, 103, 104).

Van Gils, D. P. M., Huisman, S. G., Grossmann, S., Sun, C. & Lohse, D. (2012). Optimal Taylor–Couette turbulence. *J. Fluid Mech.* 706: 118–149

(cit. on pp. 11, 27, 33–35, 38, 40–42, 44, 45, 48, 49, 51, 52, 60, 62–65, 76, 79, 81, 90, 104).

Van Gils, D. P. M., Narezo Guzman, D., Sun, C. & Lohse, D. (2013). The importance of bubble deformability for strong drag reduction in bubbly turbulent Taylor–Couette flow. *J. Fluid Mech.* 722: 317–347 (cit. on p. 12).

Van Hout, R. & Katz, J. (2011). Measurements of mean flow and turbulence characteristics in high-Reynolds number counter-rotating Taylor–Couette flow. *Phys. Fluids* 23: 105102 (cit. on p. 3).

Wattendorf, F. L. (1935). A study of the effect of curvature on fully developed turbulent flow. *Proc. R. Soc. London A* 148: 565–598 (cit. on pp. 69, 71, 82, 83).

Wendt, F. (1933). Turbulente Strömungen zwischen zwei rotierenden konaxialen Zylindern. *Ing.-Arch.* 4: 577–595 (cit. on pp. 3, 9, 10, 12, 30, 31, 41, 45, 48, 52, 69, 103, 104).

PUBLICATIONS

The following publications are included in parts or in an extended version in this thesis:

1. H. J. Brauckmann & B. Eckhardt (2013a). Direct numerical simulations of local and global torque in Taylor–Couette flow up to $Re = 30\,000$. *J. Fluid Mech.* 718: 398–427.

   This paper was written during the doctoral period and is based mainly on results from my master's thesis (Brauckmann, 2011) and on new analyses shown in figures 6, 11 and 13 therein. The latter two figures are included as Figure 2.8 and Figure 2.10 in Section 2.6 of this thesis, where the discussion of the figures is partly adopted from the paper.

   contributions The study was proposed by BE and jointly designed with HB. The simulations and data analysis were performed by HB under the supervision of BE. HB wrote the first draft of the paper with input and feedback by BE.

2. H. J. Brauckmann & B. Eckhardt (2013b). Intermittent boundary layers and torque maxima in Taylor–Couette flow. *Phys. Rev. E* 87: 033004.

   The results of this paper are discussed in an extended version in Chapter 3 of this thesis. The paper's appendix is reproduced here in Appendix A.

   contributions HB and BE jointly developed the study design. The simulations and data analysis were performed by HB under the supervision of BE. HB derived the prediction $\mu_p(\eta)$ after a suggestion for the physical mechanism by BE. HB re-evaluated the torque measurements by Wendt. The first draft of the paper was written by HB with input and feedback by BE.

3. S. Merbold, H. J. Brauckmann & C. Egbers (2013). Torque measurements and numerical determination in differentially rotating wide gap Taylor–Couette flow. *Phys. Rev. E* 87: 023014.

   The paper presents a direct comparison of torques from the experiment and the simulation, which is included as Figure 2.9 in Section 2.6 of this thesis.

   contributions The idea was developed in discussions between SM, HB, CE and Bruno Eckhardt. SM performed the experiments under the supervision of CE. HB performed the simulations and computed the bisector line. The first draft of the paper was written by SM with input and feedback by HB and CE.

4. H. J. Brauckmann, M. Salewski & B. Eckhardt (2016). Momentum transport in Taylor–Couette flow with vanishing curvature. *J. Fluid Mech.* 790: 419–452.

   The main part of this paper is reproduced in Chapter 4, and the analysis of enhanced torque fluctuations is included in Chapter 3. Further parts of the text are reproduced in Section 1.2.2, Section 2.4, Section 2.5 and in the abstract of this thesis.

   CONTRIBUTIONS The idea for the study was developed in joint discussions between HB, MS and BE. HB performed the TCF simulations and analysed the results with feedback by MS and BE. The simulations of RPCF were performed by MS, and the analyses were done by HB and MS with feedback from BE. The first draft of the paper was written by HB with input and feedback by MS and BE.

5. H. J. Brauckmann & B. Eckhardt (2016). Marginally stable and turbulent boundary layers in low-curvature Taylor–Couette flow. *Manuscript in preparation*.

   This paper is written based on Chapter 5 of this thesis.

   CONTRIBUTIONS The idea for the study was developed by HB with feedback by BE. HB derived the model, numerically solved the model equations, performed the simulations and analysed the results, with the input by BE. HB wrote a first draft of the paper with feedback by BE.

EFMC9 young scientist prize paper:

6. H. J. Brauckmann & B. Eckhardt (2015). Intermittent boundary layers in Taylor–Couette flow. *EUROMECH Newsletter* 46: 8–14.

   The results of this paper are discussed in an extended version in Chapter 3 of this thesis. For CONTRIBUTIONS see item 2 above.

ACKNOWLEDGEMENTS

I would like to express my deep thankfulness to many people who made this study possible.

First of all, I want to thank my supervisor, Prof. Bruno Eckhardt, for his continuous support and numerous valuable ideas for this work. He often elucidated the broader picture of fluid dynamics, and his enthusiasm for new findings has always been very motivating for me.

Furthermore, I like to thank Prof. Jörg Schumacher for his willingness to become the second referee of this thesis. I also appreciate the fruitful scientific discussions and his hospitality during my visits to his group in Ilmenau. I would like to express my gratitude to Prof. Siegfried Großmann for the joyful and valuable discussions. His positive nature is very encouraging. Special thanks go to Prof. Marc Avila for developing, providing and explaining the code used for the Taylor–Couette simulations. Discussions with him about scientific and numerical aspects were always helpful.

For the friendly and cooperative atmosphere at work, I have to thank all members of our research group "Komplexe Systeme". In particular, I was happy to share an amicable office atmosphere with Tobias Kreilos and Felix Schmidt, and enjoyed the chats about computers, programming, fluid dynamics and life. Special thanks also go to Jens Pfeifer and Stefan Zammert for proofreading this dissertation. For the good cooperation on topics related to rotating flows, I particularly thank Matthew Salewski, Georg Ehlers, Annika Franeck and Martin Lellep.

Moreover, I am grateful for the cooperation with Sebastian Merbold and Prof. Christoph Egbers, who explained many experimental aspects of Taylor–Couette flow to me. For various stimulating discussions, I thank many colleagues that I met at conferences or workshops, especially Prof. Daniel Lathrop, Prof. Detlef Lohse, Rodolfo Ostilla-Mónico, Matthew Paoletti, Liang Shi and Sedat Tokgoz.

Prof. Andreas Schrimpf and Andreas Oppermann deserve many thanks for their great help with the IT infrastructure at the physics department. Furthermore, I thank Thomas Gebhardt and the HRZ team for their support with the use of the MaRC and MaRC2 clusters. I am also grateful for the computing time at the LOEWE-CSC in Frankfurt. This work was financially supported by the German Research Foundation (DFG) within the research unit FOR 1182.

Special thanks go to my parents Annegret and Michael, who supported me all the years and made many things possible for me. I am grateful to my grandparents Ellen and Ferdinand, who arouse my curiosity for physics. Finally, I am happy to thank Annika, who gave me encouragement and supported my work all the time.